High Speed Autonomous Off-Road Vehicle Steering

by

Theunis Richard Botha

Submitted in partial fulfilment of the requirements for the degree

Master of Engineering
(Mechanical Engineering)

in the Faculty of

Engineering, Built Environment and Information Technology (EBIT)

at the

University of Pretoria,
Pretoria

February 2011

Summary

Title:	High Speed Autonomous Off-Road Vehicle Steering
Author:	Theunis Richard Botha
Study Leader:	Prof. P.S. Els
Department:	Mechanical and Aeronautical Engineering, University of Pretoria
Degree:	Masters in Engineering (Mechanical Engineering)

High speed cornering of an off-road vehicle poses considerable challenges to the development of an autonomous vehicle due to the non-linear dynamics of the tyre road interface as well as those of the vehicle as a whole during high lateral accelerations. Most driver models are developed for low speed applications using linear control methods under the assumption of linear vehicle dynamics. The dynamics of a vehicle however become highly non-linear as the lateral acceleration increases, thus rendering these linear models unusable during high speed manoeuvres.

In this study, two robust driver models for use in an autonomous vehicle capable of path following at both low and high speeds are presented. Both models make use of the relationship between the yaw acceleration and steering rate to control the yaw angle of the vehicle. The first driver model is derived from the simulation of a full non-linear vehicle model in ADAMS. The Magic Tyre Formula is used to model the relationship between the vehicle's yaw acceleration and steer rate as a function of vehicle speed. The second driver model is a mathematical model which incorporates a form of sliding control. The model includes the lateral tyre dynamics as modelled by the Pacejka '89 tyre model.

Both driver models are coupled with a gain scheduling proportional derivative controller to reduce the cross-track error.

The two driver models were implemented on a Land Rover Defender and experimentally validated by performing a double lane change manoeuvre at speeds up to 80km/h. The vehicle remained stable even though the lateral accelerations experienced were 80% of the vehicle limits.

The result is a robust controller capable of path following at various speeds and at high lateral accelerations.

Acknowledgements

I would like to show my gratitude to:

- Prof. Els, for his mentorship through my postgraduate studies.

- My parents Susan and Johann Botha, for their support and aid in my masters.

- My brother Philip and Johann Botha, for their advise and support.

- My fellow postgraduate student Cor-Jacques Kat, Braham Breytenbach, Rudi Kroch, Lionel Prinsloo, Francois van der Westhuizen, for their advise, criticism and support during testing, as well as the conversations we shared during our coffee drinking sessions.

- Carl Becker for his help and for our swim sessions, which allowed me time to relax and refresh my mind.

Contents

List of Figures

List of Tables

List of Symbols
and Abbreviations

Abbreviations

Abbreviation	Description	Definition
ACC	Adaptive Cruise Control	page 1
A/D	Analog to Digital	page 16
ADAMS	Automatic Dynamic Analysis of Mechanical Systems	page 15
CA	Collision Avoidance	page 1
C/A	Clearance/Acquisition	page 88
CG	Centre of Gravity	page 11
CPGPS	Carrier-Phase Enhancement Global Positioning System	page 88
DARPA	Defense Advanced Research Projects Agency	page 2
DGPS	Differential Global Positioning System	page 16
DLC	Double Lane Change	page 10
DOD	Department of Defence	page 84
DOP	Dilution Of Precision	page 86
FARS	Fatal Analysis Reporting System	page 1
FFNN	Feed Forward Neural Network	page 33
FLC	Fuzzy Logic Controller	page 11
GES	General Estimates System	page 1
GLONASS	GLObal NAvigation Satellite System	page 84
GNSS	Global Navigation Satellite Systems	page 13
GPS	Global Positioning System	page 84
INS	Inertial Navigation Systems	page 89
LAAS	Local Area Augmentation System	page 88
LDT	Linear Displacement Transducer	page 16
LF	Left Front	page 16
LIDAR	Light Detection and Ranging	page 83
LQR	Linear Quadratic Regulator	page 11

Abbreviation	Description	Definition
LR	Left Rear	page 16
MATLAB	MAtrix LABoratory	page 32
MM	Mathematical Model	page 67
MTF	Magic Tyre Formula	page 67
NHTSA	National Highway Traffic Safety Administration	page 1
NN	Neural Network	page 12
NS	Neutral Steer	page 57
OS	Over Steer	page 57
PD	Proportional Derivative	page 35
RF	Right Front	page 16
RR	Right Rear	page 16
RTK	Real Time Kinematic	page 88
SA	Selective Availability	page 85
SM	Static Margin	page 55
US	Under Steer	page 57
USB	Universal Serial Bus	page 17
VBOX3	Velocity BOX 3	page 16
V/F	Voltage to Frequency	page 78
WAAS	Wide Area Augmentation System	page 88
$4S_4$	Four-State Semi-active Suspension System	page 15

Roman symbols

Symbol	Description	Definition
A	Area	page 16
a	Pseudo arctangent coefficient	page 32
a	Semi-major axis or equatorial radius	page 91
B	Magic Formula stiffness factor	page 5
BW	Bandwidth	page 95
b	Pseudo arctangent coefficient	page 32
b	Semi-minor axis or polar radius	page 91
$d_{preview}$	Preview distance	page 33
E	Eastern distance	page 90
C	Cornering Stiffness	page 2
C	Magic Formula shape factor	page 5
D	Magic Formula peak factor	page 5
D	First order term constant	page 54
dE	Change in Eastern distance	page 90
dN	Change in Northern distance	page 90
d_f	Track width front	page 65
d_r	Track width rear	page 65

Symbol	Description	Definition
E	Magic Formula curvature factor	page 5
e_{lat}	Cross-track error	page 35
e	Flattening coefficient of earth	page 91
F_1	Lateral tyre force at vertical load $W + \Delta W$	page 5
F_2	Lateral tyre force at vertical load $W - \Delta W$	page 5
F'	Lateral tyre force due to load transfer	page 5
F_y	Lateral force	page 31
F_z	Vertical force	page 31
f_{K_d}	Derivative term gain scheduling function	page 35
f_{K_p}	Proportional term gain scheduling function	page 35
f_s	Sampling frequency page 95	
G	Steady state yaw acceleration gain	page 55
g_x	Goal x coordinate	page 8
g_y	Goal y coordinate	page 8
h_{cg}	Height of centre of gravity	page 64
h_f	Front roll centre height	page 64
h_r	Roll centre height or rear roll centre height	page 64
h_s	Distance between roll centre and CG	page 65
K_d	Derivative term gain	page 35
K_p	Proportional term gain	page 35
K_ϕ	Roll stiffness	page 64
$K_{\phi f}$	Front roll stiffness	page 65
$K_{\phi r}$	Rear roll stiffness	page 65
I	Mass moment of inertia	page 51
$\mathbf{i}$	Unit vector in longitudinal x direction	page 49
$\dot{\mathbf{i}}$	Rate of change in unit vector in longitudinal x direction	page 50
$\mathbf{j}$	Unit vector in lateral y direction	page 49
$\dot{\mathbf{j}}$	Rate of change in unit vector in lateral y direction	page 50
l	Vehicle wheel base	page 55
l_f	Distance from front axle to centre of gravity	page 51
l_r	Distance from rear axle to centre of gravity	page 51
M_ϕ	Moment about roll axis	page 65
m	Mass of vehicle	page 51
N	Northern distance	page 90
$n_{steerboxratio}$	Steer box gear ratio	page 79
P	Zero order term constant	page 54
p	Pressure	page 16
R	Radius of curvature	page 39
R_m	Meridian radius of curvature	page 91
R_n	Prime vertical radius of curvature	page 91
r	Yaw rate	page 50
r_{arc}	Arc radius	page 90
$\dot{r}$	Yaw acceleration	page 53
$\dot{\mathbf{R}}$	Velocity vector	page 49

Symbol	Description	Definition
$\ddot{\mathbf{R}}$	Acceleration vector	page 50
SF	Stability Factor	page 55
SM	Static Margin	page 55
S_h	Horizontal shift	page 5
S_v	Vertical shift	page 5
s	Laplace operator	page 53
s	Arc length	page 90
T_r	Responsiveness	page 55
t_r	Response time	page 95
t	Time	page 35
t	Track width	page 64
u	Velocity in the longitudinal x direction	page 49
$\dot{u}$	Acceleration in the longitudinal x direction	page 50
V	Vehicle Velocity	page 39
v	Velocity in the lateral y direction	page 49
$\dot{v}$	Acceleration in the lateral y direction	page 50
W	Weight	page 65
X	Magic Formula, unsifted side-slip angle	page 5
X	Longitudinal position	page 38
x	Magic Tyre, shifted lateral tyre force	page 5
$\dot{x}$	Longitudinal vehicle speed	page 31
y'	Derivative of lateral position (Y) with longitudinal position (X)	page 39
y''	Second derivative of lateral position (Y) with longitudinal position (X)	page 39
Y	Magic Tyre, shifted lateral tyre force	page 5
Y	Lateral position	page 38
y	Magic Tyre, unshifted lateral tyre force	page 5
$\ddot{y}$	Lateral acceleration	page 39

Greek symbols

Symbol	Description	Definition
β	Side-slip angle	page 2
$\dot{\beta}$	Rate of change of side-slip angle	page 53
ΔF_z	Axle load transfer	page 65
ΔW	Change in vertical load	page 5
δ	Front wheel steer angle	page 51
$\dot{\delta}$	Front wheel steer rate	page 31
$\dot{\delta}_{e_{lat}}$	Steer rate from lateral position controller	page 35

Symbol	Description	Definition
$\dot{\delta}_{\psi,FFNN}$	Feed Forward Neural Network controller steer rate output	page 35
$\dot{\delta}_{\psi,MM}$	Mathematical Model controller steer rate output	page 56
λ	Longitude	page 90
$\lambda_{1,2}$	Roots of characteristics equation	page 54
$\dot{\omega}_a$	Rotational speed of actuator	page 78
$\dot{\omega}_{tyre}$	Rotational speed of tyre	page 79
ω_n	Undamped natural frequency	page 55
ϕ	Roll angle	page 64
ϕ	Latitude	page 90
ψ_p	Predicted yaw angle at preview point	page 33
ψ_d	desired yaw angle at preview point	page 33
ψ_a	Vehicles current yaw angle	page 33
$\dot{\psi}$	Vehicle current yaw rate	page 33
$\ddot{\psi}$	Vehicle yaw acceleration	page 31
τ	Time step	page 31
θ	Angle	page 90
ζ	Damping ratio	page 55

Subscripts

Symbol	Description	Definition
f	Front	page 53
$f1$	Front left tyre	page 53
$f2$	Front right tyre	page 53
i	Inner tyre	page 64
o	Outer tyre	page 64
$static$	Static i.e. vehicle stationary	page 65
r	Rear	page 53
$r1$	Rear left tyre	page 53
$r2$	Rear right tyre	page 53

Chapter 1

Introduction and Literature Survey

1.1 Introduction

In recent years the integration of autonomous systems with passenger vehicles has become an important focus in research. Research into autonomous system has significantly contributed towards vehicle safety and useability. This is a field with great potential for innovation and ground breaking research. One such area for research is lateral vehicle control which is important for vehicle safety and fully autonomous vehicles.

Current research in autonomous systems has already been implemented in an effort to reduce accidents, improve safety and enhance driver comfort. A focus area has been the development of Adaptive Cruise Control (ACC) with Collision Avoidance (CA)) (Moon et al, 2009), whereby the vehicle can be set at a constant speed, detect a preceding vehicle and automatically control braking and acceleration to maintain a specified distance between the vehicles. However, active CA is currently limited to longitudinal control and used to improve reaction time during braking. In the event that an oncoming collision is detected, braking is used to slow or completely stop the vehicle to prevent the collision. On the other hand, lateral CA is limited to notifying the driver that a lateral movement will result in a collision by either making use of warning lights, audible warning sounds or in more advanced systems, by providing steering feedback. Thus, there is a need for active lateral CA.

According to the United States National Highway Traffic Safety Administration's (NHTSA) two major crash databases, namely Fatal Analysis Reporting System (FARS) and the General Estimates System (GES), run-off-road collisions account for approximately 15% of all collisions reported in FARS, but are responsible for approximately a third of all fatal collisions. Collisions where the vehicle failed to negotiate a curve were 4.7% of total collisions and 14% of all fatal collisions (O'Connor, 2004). By contrast head-on collisions accounted for about 2% of all police reported collisions and about 10% of all fatal collisions (O'Connor, 2004).

Lateral collisions, thus, typically result in more severe injuries and higher fatalities. Unlike longitudinal collision prevention, no active control exists which completely takes lateral

control of the vehicle to prevent collisions.

Two key aspects of lateral obstacle avoidance as well as autonomous control are:

1. the identification of an obstacle, as well as a path around the obstacle (often referred to as path planning)

2. the following of the identified path which will prevent the collision (commonly referred to as path following).

Path following, in turn, requires the determination of the precise steering input required to control the lateral motion of a vehicle, termed a driver model. Collisions typically occur at highway speeds and therefore requires a driver model which provides stable and accurate control at highway speeds. Currently, few existing driver models allow for stable control at these speeds.

Autonomous vehicle research is not only important for vehicle safety, but is also at the forefront of many robotic institutes, mining facilities and military organisations due to the numerous benefits they pose for their respective industries.

Although rigorous mathematical models have been developed with non-linearities and multiple degrees of freedom, many steering controllers still make use of basic linear methods. In the Defense Advanced Research Projects Agency (DARPA) challenge, most vehicles make use of kinematic based controllers that only take the steering geometry into account (Snider, 2009). During low lateral acceleration manoeuvres, these controllers provide satisfactory performance where the assumption that tyre characteristics are linear i.e $F_y = C\beta$. At higher lateral accelerations, however, the non-linear dynamics of the tyre road interface becomes a dominating factor and should be taken into consideration. Dynamic models have been developed to take this into account with the majority making use of a linearisation of the non-linear model (Plochl and Edelman, 2007), which provides satisfactory results at low to moderate lateral accelerations. Great difficulty is often experienced with these models in determining the gain parameters for a stable controller at various speeds. At higher lateral accelerations these linearised models also provide unsatisfactory performance due to the complex vehicle dynamics and non-linear tyre characteristics which are mostly neglected. More complex controllers are generally considered to be too computationally expensive to be implemented in real time control of an autonomous vehicle. Many also require parameters that are not easily available on a real vehicle.

A simple and robust driver model is thus required which can incorporate the non-linear dynamics of the tyre road interface.

1.2 Lateral Tyre Force

The tyres are the only contact a vehicle has with the road. It is this interaction with the road that allows a vehicle to move longitudinally as well as perform lateral motions. It is thus vital to understand the tyre-road interface when conducting any form of vehicle dynamic analysis.

This study involves the lateral motions of a vehicle i.e cornering, therefore a short study of the literature on lateral force generation of a tyre is presented.

1.2.1 Basics of Lateral Force Generation

The lateral forces generated by a vehicle when cornering, act through the contact area of the tyre and road - neglecting any aerodynamic effects. The tyre-road interface thus becomes the most important factor in the handling of a vehicle. During cornering a deformation in the tyre is introduced by steering the tyre. The deformation is such that an angle is formed between the tyre's travelling direction and the tyre's longitudinal centre line. This is called the tyre side-slip angle β as shown in Figure 1.1 (Abe, 2009). At small side-slip angles a majority of the tyre deformation is parallel with the tyre's direction of travel with the largest deformation taking place near the rear of the contact surface. As the side-slip angle increases, the portion of the contact surface parallel to the travelling direction decreases, with the largest lateral deformation moving more to the front of the contact surface. As the side-slip angle increases further around 10-12° the contact surface parallel to the travel direction disappears and the deformation becomes more symmetric around the wheel centre.
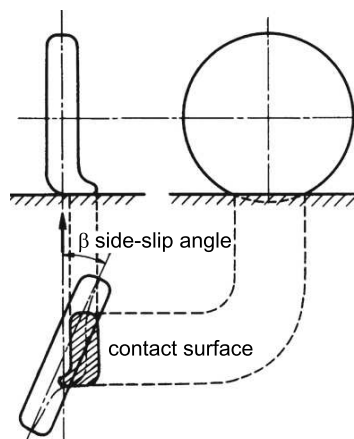
Figure 1.1: Tyre deformation during cornering (Abe, 2009 as modified).

1.3 Typical Tyre Data

Fiala's (1954 in Abe, 2009) model can be used to understand the tyre-road interaction. The factors involved in determining this interaction are numerous and are not constant and therefore make it difficult to apply the model to simulations. As a result, most simulation tyre models rather fit experimentally obtained tyre data rather than mathematically modeling a tyre.

1.3.1 Non-linear lateral force and side-slip angle relationship

Figure 1.2 displays the experimentally obtained lateral force as a function of side-slip and vertical force for two different tyres (Avon motorsport tyres, 2010). It is clear from this figure that a linear region exists where the lateral force is directly proportional to the side-slip angle. The saturation of the tyre force can also be observed being more evident in Figure 1.2b. This relationship mirrors that of Fiala's model. The implication of the non-linearity is that as the tyre produces a force, the side-slip angle and thus steering action required to increase the force, increases exponentially up to saturation.

Other factors such as the camber angle also influence the lateral tyre force. However, the vehicle used for this study is equipped with solid axles. The tyres on solid axle vehicles will generally remain vertical with a camber of zero. While the tyres' camber angle can change as a result of tyre deflection this is considered to be very small. As a result the effect of camber will be assumed negligible for the rest of this study.

The experimental tyre lateral force vs. side-slip angle as a function of vertical force is typically curve fitted using a Pacejka tyre model. While other models also exist the Magic Formula tyre model, as developed by Pacejka, is well known and the '89 model is implemented in the vehicle simulation model presented in chapter 2. This model allows for simple yet accurate lateral force tyre modeling.

(a) Avon Formula student tyre (b) Avon Prototype Lites tyre
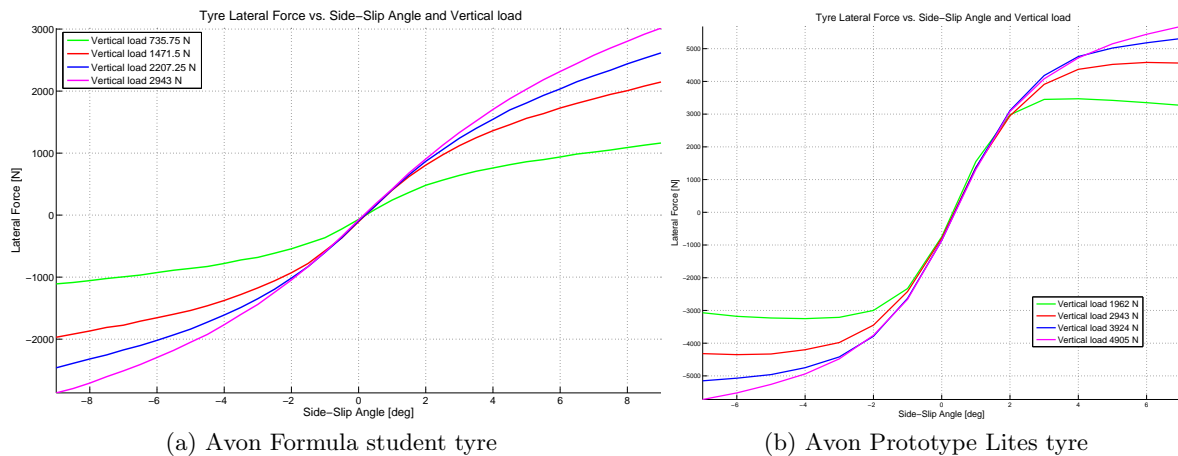
Figure 1.2: Tyre lateral force vs. side-slip angle as a function of vertical load.

1.3.2 Load Transfer Effect

If the tyre data were to be plotted as lateral force vs. vertical force as a function of side-slip angle (as depicted in Figure 1.3) it becomes evident that for a given side-slip angle the relationship between lateral force and vertical load is also non-linear. The relationship also seems to reach a saturation level, this has a profound effect during cornering. For an axle with two wheels the static load on each wheel is W, when cornering a load transfer occurs

between the inside and outside wheels. The outside wheels become more loaded $(W + \Delta W)$ and the inside wheel load reduces $(W - \Delta W)$. This yields lateral forces F_1 and F_2 respectively at each wheel and a combined average force of F' for the axle as opposed to F for the no load transfer case. Thus, it is clear that during cornering the load transfer reduces the lateral force capable of being generated by a vehicle for a given side-slip angle. The larger the load transfer, the greater the reduction in total lateral force. It should also be noted that in most cars the load transfer is different for the front and rear wheels.
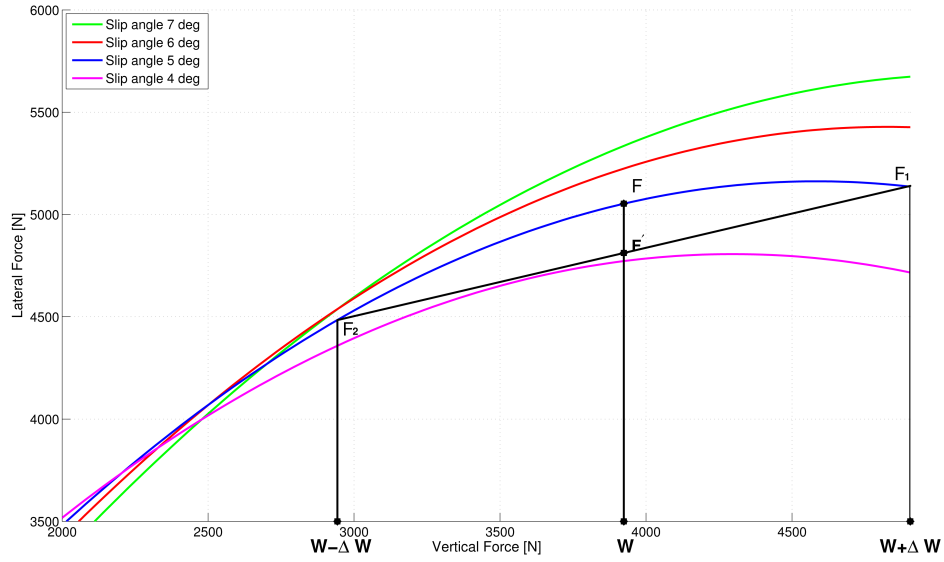
Figure 1.3: Tyre lateral force vs. vertical load as a function of side-slip angle.

This indicates that during cornering the tyre road interface is highly non-linear and cannot be generalised by a single model which does not include the tyre specific model. This implies that experimentally obtained tyre data, for the specific tyre, should be used as opposed to a generalised tyre model.

1.3.3 Magic Tyre Formula

The Magic Tyre Formula describes the tyre's handling characteristics by means of one formula. This study will consider the Magic Formula as used to describe the tyre's lateral force vs. side-slip angle relationship as presented in Figure 1.2. The formula is defined as:

$$y(x) = D\sin(C\arctan\{Bx - E(Bx - \arctan(Bx))\}) \qquad (1.1)$$
$$Y(X) = y(x) + S_v \qquad (1.2)$$
$$x = X + S_h \qquad (1.3)$$

The terms are defined as:

- $Y(X)$ tyre lateral force F_y

- X tyre side-slip angle

- B stiffness factor

- C shape factor

- D peak factor

- E curvature factor

- S_h horizontal shift

- S_v vertical shift

These terms depend on the vertical tyre load and camber angle. The use of this formula allows the fitting of the tyre's lateral force vs. side-slip angle relationship with a smooth function. This allows the full representation of the relationship at various vertical loads and side-slip angles by a small set of discrete experimental data points.

1.4 Driver Models

The types of driver models identified in the literature can be classified into two broad categories. The first is a controller which simply mimics a human driver taking very little vehicle elements into consideration. The second type of controller is based on the vehicle characteristics either derived from simple kinematics relationships, or more complex controllers based on a dynamic vehicle model. A summary of these driver models are provided to illustrate typical driver models employed in simulations and in experimental autonomous vehicles, as well as, their shortcomings when considering non-linear tyre dynamics.

1.4.1 Human Based Driver Models

A human based driver model places more emphasis on the modelling of a human's response than on the vehicle itself. While in some cases vehicle models are still used, the emphasis is placed on modeling the response of a typical driver. The modeling could include physical attributes, such as a neuron muscular dynamics with thresholds or information reception such as visual, vestibular, tactile and auditory. The modeling could include a human's greatest abilities such as prediction, anticipation, adaptation and learning. MacAdam (2003) lists key properties which a controller must satisfy to be deemed a minimum representation of a human driver. These include:

- provision for a transport time delay

- use of preview by the driver for sensing upcoming lateral and longitudinal control requirements

- driver adaptation provision so that alterations to the controlled vehicle dynamics and operating conditions can be approximated or accounted for within the driver model

- the exhibition of the aforementioned linear regime "crossover model" behaviour in the immediate vicinity of the crossover frequency

- the presence of an internal vehicle model or equivalent capability within the structure of the driver model in order to help estimate future controlled vehicle responses.

MacAdam also provides a secondary set of desirable attributes, these attributes are not necessarily essential depending on the application, but include:

- provisions for processing incoming sensory signals to account for neural delays, thresh holding, rate limiting, and dynamical properties of individual sensory channels

- neuromuscular filtering elements for output channels such as steering, braking, and throttle control responses

- previewed path adjustment capabilities/strategies by the driver model to account for driver skill-related abilities or preferences in selecting alternate or modified paths

- driver abilities to adjust speed based on upcoming lateral path requirements in order to facilitate path tracking along curves and around obstacles, thereby enhancing directional stability during such conditions

- provisions for surprise or situational awareness features within the model that allow discrimination between control responses provided by well rehearsed or highly practised driving scenarios versus unrehearsed or less familiar driving scenarios

- the inclusion of some forms of driver skill factors, or corresponding parameter adjustments, that are known or estimated to correlate with different categories of driver experience or skill.

Accurate modeling of these aspects would produce a driver model which would be representative of a human driver. However, the development of such a model requires a large database containing the responses of various drivers with varying abilities, performing a multitude of manoeuvres. The question also arises whether the modelling of a human would be best for vehicle control since in many vehicle dynamics simulation cases, better control can be obtained by simple mathematical models instead of modelling a human response. The greatest advantage in modeling a human is in the adaptation/learning attribute, however these attributes are still missing in most human based driver models and can also be implemented in mathematical models. The vehicle-driver forms a closed-loop control system, human attributes are therefore implemented to ensure that the system will be safe and stable. For autonomous control, which is the current focus, the driver model need not include any human driver aspects as the vehicle will be driven by a control system.

1.4.2 Vehicle Based Driver Models

Three types of vehicle derived controllers are mainly used, namely geometric, kinematic and dynamic controllers. The most simple are the geometric and kinematic based controllers. The fundamental assumption made in these two controllers is that the dynamic effects of the tyre-road interface is negligible, and thus a no slip assumption is made. The DARPA urban challenge saw various autonomous vehicles competing in an urban challenge. While this challenge mostly tested the vehicles' decision making abilities, such as path planning, steering models were implemented to track the planned path. The majority of competitors including some of the well known and successful autonomous vehicles - Boss (Urmson et al, 2008) and Stanley (Thrun et al, 2006) - made use of relatively simple control strategies.

Geometric Driver Models

The most simple models use geometric relationships between the wheel base, steering angle and radius of curvature of the road. These models take no preview into consideration as it takes the radius of curvature at the front wheel. The pure pursuit model used by various mobile robots, uses a simple proportional controller on the cross-track error at a certain preview distance ahead. The preview distance and cross-track error are obtained by making use of the geometric relationship involving the turning radius and steer angle (Amidi, 1990). Figure 1.4 shows a basic illustrations of two geometric based driver models.

(a) Simplified Ackerman geometric model   (b) Pure pursuit geometric model
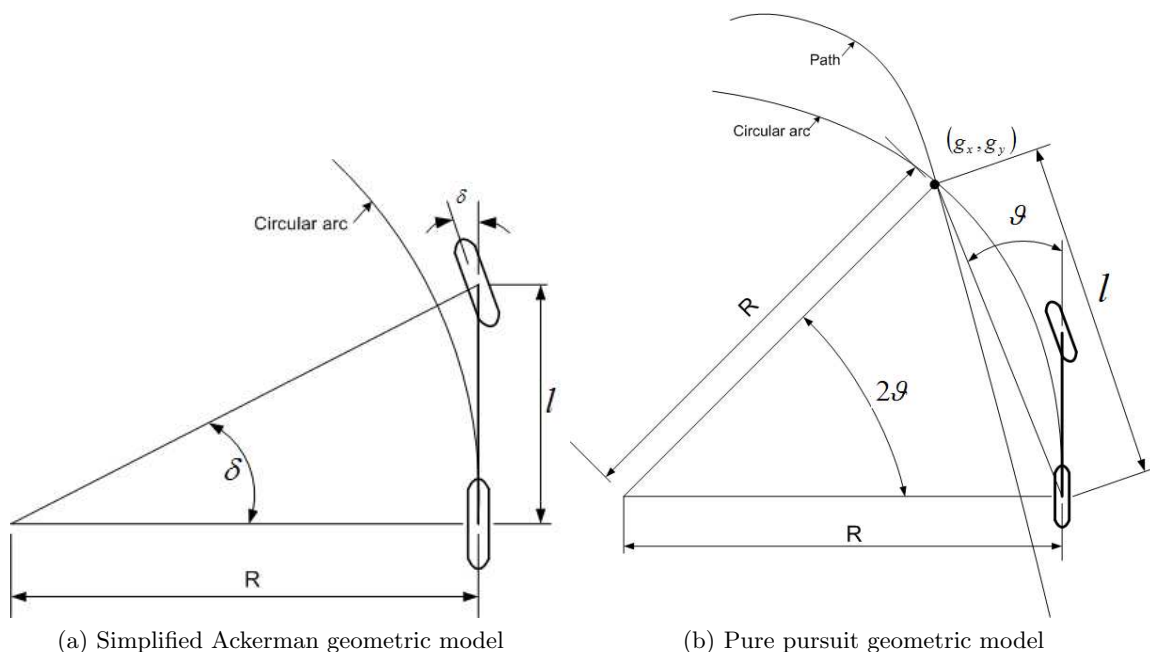
Figure 1.4: Geometric models based on geometric relationships.

The Stanley method (Thrun et al, 2006) used on the successful Stanley vehicle, which won

the DARPA Grand Challenge in 2005, uses a simple cross-track error at the front wheels. This, coupled with a term to reduce the difference between the vehicle heading and the path heading with no preview, provides a simple control strategy.

The geometric controllers use no inherent vehicle model to develop the control strategy except for making use of the wheelbase in certain cases. The controllers also make use of simple proportional controllers. Snider (2009) gives an overview of these controllers as applied to a CarSim simulation, with various gain settings. It was found that good control for these controllers can be obtained at very low speeds for various gain values, however the gain values which gave the best control at lower speeds cause the vehicle to become unstable as the speed increases. While the gains which gave the worst performance at low speeds are the only gains which provided stable control at higher speeds. Thus, a compromise between low speed performance and high speed stability has to be made. The performance at higher lateral accelerations has also been lacking, with the controller either becoming unstable or resulting in large tracking errors.

Kinematic Driver Models

A kinematic controller is the most basic controller in which a vehicle model is developed. The model, as the name implies, is derived from the kinematic equations of motion governing the vehicle planer motion, making the assumption of no slip. The most basic model makes use of a simple yaw planar model (bicycle model) deriving the equation for both the longitudinal and lateral velocities and displacements, as well as the vehicle heading in terms of the steering angle, wheel base and vehicle speed. Figure 1.5 shows a basic illustration of a kinematic driver model. De Luca et al (1998) derive a control action which minimises the cross-tracking and heading errors by a suitable steer input. The controller contains three gains, however stability is obtained by selecting the gains based on a relationship of one single gain value.

This controller provides better control than the geometric based controllers at low speeds. However, the same trade-off between low speed performance and high speed stability exist as in the geometric controllers. The stability at higher lateral acceleration is also very dependant on the gain value, with the vehicle becoming too unstable with either too high or too low gain values.

Dynamic Driver Models

The dynamic model is the first model which introduces the mechanism of slip. The model derives the dynamic equations of motion for a vehicle from the forces generated by the tyres due to the side-slip angles at the respective tyres. These models range from simple bicycle models to more complex four wheel models which could include the roll and pitch motions as well.

Ackerman and Sienel (circa 1989) used a linearised tyre model and yaw rate feedback to design a robust controller for a bus. The yaw rate feedback was used to reduce the influence of mass and velocity on the dynamics of the controller, since it can capture the dynamic
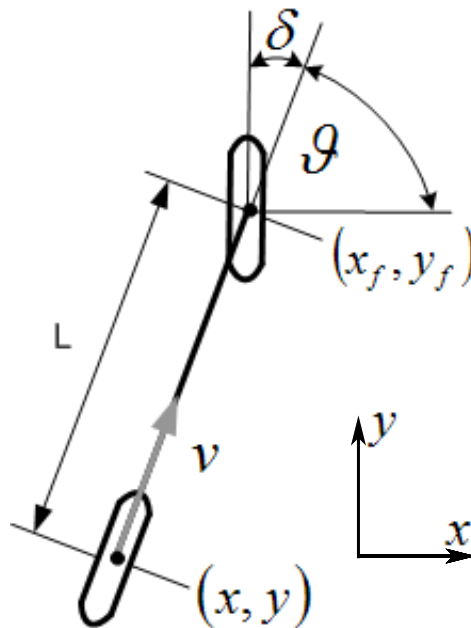
Figure 1.5: Kinematic model.

effects of the uncertain parameters velocity, mass and road surface. However, the model does not include any suspension effects and is still limited to moderate speeds <80km/h.

To compensate for larger velocity changes, Chatzikomis and Spentzas (2009) made use of a simple proportional derivative controller with gain scheduling on the heading angle error to provide a steering action. The gain scheduling is introduced to compensate for the effect the longitudinal velocity has on the vehicle dynamics based on a linear tyre model. The controller, tested on a passenger vehicle, successfully performs the Double Lane Change (DLC) manoeuvre at 67km/h. It was found that, at this speed the vehicle utilised almost all the lateral tyre force capability of the tyres. However, pilot testing, for this study, demonstrated that significantly higher speeds (80-100km/h) are easily attainable through a DLC with a normal driver in any modern passenger vehicle. Thus, 67km/h is taken as the stability limit for the controller propose by Chatzikomis and Spentzas (2009) and not the vehicle, through a DLC.

Fenton et al (1976) made use of experimental tests to determine the transfer functions between the steer angle and yaw rate. The model also incorporates transfer functions between a super elevation force and a disturbance force (eg. side wind). While the experimental yaw rate transfer function is compared to a mathematically obtained function, the experimental yaw rate transfer function is used in the controller. A multiple termed compensator is used to obtain the desired performance. The model assumes that the yaw rate transfer function remains fixed at a certain speed. While this function is dependant on vehicle speed the controller shows satisfactory results at a range of speeds. The model is however only tested at low lateral accelerations $< 2m/s^2$.

Rajamani (2006) used state space modeling to obtain a model of the problem in terms of both the cross-tracking error and heading error from the vehicle Centre of Gravity (CG) as well as their derivatives. The model also incorporated a desired yaw rate determined from both the path curvature and vehicle speed. A Linear Quadratic Regulator (LQR), from optimal control theory, is used to determine the gains of the feedback controller. Snider (2009) incorporated the control law in CarSim. It was found that the controller provided excellent control at low to medium speeds. However, as a result of the zero preview, the controller failed to control the vehicle at high speeds, as well as at high levels of lateral accelerations.

To alleviate the problem of zero preview, Sharp (2005) proposed an optimal preview controller whereby the path profile is sampled at discrete intervals based on the vehicle speed and a sample time. The cross-track error is a combination of all the path errors for a certain amount of preview points ahead obtained by using a low frequency filter. Use of a linear bicycle model and the LQR method is made to produce the desired controller. Snider (2009) also investigated this controller in the CarSim environment for various tuning parameters. The controller was found to be more robust than the zero preview LQR controller of Rajamani (2006). The controller was however also found to become more unstable at higher speeds with a similar compromise between low speed accuracy and high speed stability needed as other controllers.

While the above controllers typically make use of classic control theories, various other control strategies have also been proposed. El Hajjaji and Bentalba (2003) proposed a Fuzzy Logic Controller (FLC) for path tracking. A nonlinear vehicle model is used in terms of the equations of motion, however, the vehicle still makes use of a linear tyre model. The model is then linearised at various operational points and a local controller gain calculated for each local linearised model. The global controller is inferred by calculating the weighted average of all local controllers. While the controller provided good control, the controller was not tested at length at various speeds and lateral accelerations. Hessburg and Tomizuka (1994) developed a FLC that uses multiple rules. The rules are manually obtained either from experimental analysis, other controllers or heuristics. The controller output is then given as a combination of these rules, determined by triangular membership functions. The rules are divided into steering angle rules for feedback, which contain error terms on the path, rules on preview which contain the current turn's curvature and the following turn's curvature as well as the curve transition time. A rule set on gain scheduling, which takes the effect of an increase in vehicle speed into account, is also implemented. The final steer output is then a combination of the preview rules and feedback rules steering angles, of which the gain scheduling determines the combination scheme. The controller, while not tested at higher speeds and lateral accelerations, provides reasonable control. The construction of the rule sets can be seen as a very tedious process, but does allow the designer to completely tailor the vehicle response to various situations using any input imaginable.

Peng and Tomizuka (1990), as well as Sienel and Ackermann (circa 1995), proposed a feedforward controller. They made use of the curvature of the road - since on normal roads these curvatures are constant in a turn - to estimate the yaw rate and thus a desired steering

angle by making use of linear vehicle models. Peng and Tomizuka (1990) further improved the linear model by estimating the cornering stiffness based on the measured lateral acceleration and yaw rate. An additional feedback controller is used to provide closed loop control. The use of the feedforward controller provided improved robustness of the overall control strategy. Peng and Tomizuka (1991) also made use of a feedforward/feedback controller utilising the optimal preview control similar to Sharp (2005) in both the feedforward and feedback controllers. The controller enables the vehicle to perform path following with small cross-tracking errors, however while tested at higher speeds the controller was not tested at higher lateral accelerations.

Neural Networks (NN) have been used for decades to emulate the response of humans to various stimuli (Lo et al (2008), Gingrich et al (1992) and Moon et al (2002)). It thus follows that NN could also be used to emulate a human driver. Since the 1990's various researchers have played with this possibility. The most common architecture being a non-linear two layered NN trained using data obtained either from simulations or experimental tests. Inputs to the NN can include yaw rate, roll angle and roll rate, lateral displacement, velocity and acceleration and cross-track error with outputs including steer angle and steer rate. The largest problem with NN is the method for generating training data as this process is in general expensive and time consuming. Generalisation of NN are also a problem, with various techniques used to improve NN generalisation. The effect of a change in vehicle properties such as mass, moment of inertia as well as tyre properties which, unless specifically added during training - and thus greatly increasing the amount of training data - could not be taken into consideration by such a controller.

A non-linear controller which accounts for tyre saturation is implemented by Sharp et al (2000). The controller uses multiple previewed cross-track errors as well as yaw angle error. A steer angle is determined by multiplying each error with an associated gain and computing the sum. Non-linear control is obtained by means of a saturation function on each error term. In the case of an understeer vehicle, where the cross-track error would have a larger contribution than the yaw angle error, an additional saturation function is placed on the sum of the cross-track error terms. This effectively reduces the steering effect and prevents the front tyres from working too far into the saturation limit. In the case of an oversteer vehicle, the yaw angle error would have a larger contribution and as such a saturation function is placed on the overall output of the driver model. This saturation function as well as the gains are mainly manually tuned with the use of some intuition. The model was tested on a Formula 1 simulation model. The controller provided excellent control at various lateral acceleration levels. The model however does not include suspension deflection and thus the robustness towards suspension effects are unknown.

1.5 Focus of the Research

In light of the need for an autonomous steering system, the question is how to develop such a driver model for path following, capable of being used for CA. In order to investigate an appropriate driver model for this purpose, this study will focus on autonomous steering control of an off-road vehicle. The two main aspects required for autonomous steering control are, firstly the identification of a path, and secondly the following of the identified path. This study concentrates on the path following aspect of autonomous control, hence no emphasis will be placed on the determination of a path. It will thus be assumed that a path will be known or prerecorded. Emphasis will then be on a driver model which can control the lateral position of the vehicle under conditions of high lateral acceleration where non-linearities are significant. The driver model will include the dynamics of the lateral tyre road interface which allows for more accurate control at higher lateral accelerations. However, the driver model must be capable of providing accurate and stable path following at low speeds defined as speeds below the urban speed limit i.e. <60km/h as well as high speeds (>80km/h). The model must also be capable of working at high lateral accelerations (i.e. >4m/s^2) in the non-linear tyre regime. The driver model is to be implemented and validated experimentally. The experimental test will culminate in a ISO3888-1 (ISO3888-1, 1999) double lane change performed autonomously at approximately the speed achievable in the test vehicle by an experienced human driver, to test at both high speed and lateral acceleration.

Such a driver model, which is the focus of this research, builds on how tyres generate lateral forces, as well as the aspects of driver models that are neglected, or can be improved, as discussed in the literature study. A summary on the available vehicle platform and the simulation model thereof follows in Chapter 2. Furthermore in Chapter 2, the discussed simulation model will allow for quicker development of a system since it allows for the evaluation of a change in parameters faster and safer than experimental validation. The simulation model is only an effective tool if it is representative of the actual vehicle, and for this reason an experimental validation of the simulation model is also performed.

Chapter 3 presents a modified version of the novel driver model developed by Thoresson (2007), which uses the Magic Formula (Bakker et al, 1989) to model the relationship between vehicle yaw acceleration, speed and steer rate input. This relationship was obtained from simulations conducted with the simulation model presented in chapter 2. Chapter 4 presents a controller whereby the yaw acceleration, speed and steer rate relationship is mathematically modelled instead of using the Magic Tyre Formula. The mathematical model also includes a tyre model. A Global Navigation Satellite Systems (GNSS) system is used to provide the controller with position coordinates used to experimentally evaluate the driver models presented in chapters 3 and 4. Chapter 5 gives an overview of GNSS systems as well as experimental tests conducted on the GNSS system available. The experimental validation is performed in chapter 6.

1.6 Conclusion from Literature Survey

The tyre road interface is highly non-linear at high lateral accelerations. Not only do the tyres move away from the linear lateral force, side-slip angle relationship, but load transfer also affects the tyre lateral force generation. The tyre construction and material also play a large role in the lateral force capable of being generated by a vehicle and thus the handling of the vehicle. This makes it nearly impossible to create a general control strategy for steering at high lateral accelerations which can be applied to all vehicle types without considering the tyre and vehicle dynamics.

There are multiple control strategies available for vehicle path following. It has however been found that a compromise between low speed tracking and high speed stability has to be made with most of these strategies. Use of linear vehicle models, especially linear tyre models, cause controllers to display poor performance at higher lateral acceleration due to the tyres operating in the non-linear regime. Many controllers require vast amounts of training data to implement or require the manual tuning of various parameters. This makes them time consuming to implement and difficult to obtain a robust controller. The driver models are typically simulated on passenger vehicles with low CG heights and relatively stiff suspension systems. Many controllers are also very sensitive to large changes in vehicle parameters, making them difficult to use in vehicle development where parameters change constantly.

A driver model which can include the non-linear tyre dynamics, as well as the effect of vehicle speed is thus desired. It is expected that such a driver model would perform well at all speeds therefore eliminating the need of a compromise between low speed accuracy and high speed stability. The driver model should also perform well at higher lateral acceleration due to the inclusion of the non-linear tyre dynamics.

Chapter 2

Development and Validation of Vehicle Simulation Model

The vehicle used for this study is a Land Rover Defender 110. This particular vehicle has been extensively used for various research projects of the Dynamics Systems Group at the University of Pretoria. Various sensors have been permanently installed on the vehicle. Most of the mass properties needed for mathematical modelling have been experimentally determined (Uys et al, 2006). This section describes the instrumentation installed on the vehicle as well as the full vehicle model developed in Automatic Dynamic Analysis of Mechanical Systems (ADAMS) (MSC.Software, 2010) software and the experimental validation thereof.

2.1 Instrumentation of Vehicle

The research vehicle is equipped with an in-house developed suspension system termed the $4S_4$ suspension and control system, as well as various transducers and a data acquisition and control system. The vehicle has also been equipped with the necessary actuators for full autonomous control. A more in depth discussion of these systems follows.

2.1.1 $4S_4$ Suspension System

The vehicle is equipped with a Four-state Semi-active Suspension System, or $4S_4$, developed by the University of Pretoria (Els, 2006). The $4S_4$ system is a hydro-pneumatic suspension system designed to switch between two discrete spring and damper characteristics. The system allows the suspension to switch between a handling mode with high suspension stiffness and damping and a ride comfort mode with low suspension stiffness and damping. Each suspension strut also contains a pressure transducer which allows for the calculation of the suspension force and thus the normal force on each wheel.

2.1.2 Measurement Instrumentation

Experimental vehicle validation forms an important part in the development of mathematical models. Kat (2009) presents a thorough discussion on the importance of experimental vehicle validation especially for the specific parameters that these models are intended to predict. Kat also warns that correlation for acceleration alone may not imply good correlation on other parameters such as suspension forces. The measurements used for vehicle validation should thus include a variety of body and suspension motions. Table 2.1 summarises vehicle parameters which are measured relating to vehicle lateral dynamics.

Table 2.1: Vehicle parameters measured for validation lateral dynamics.

Parameters	Transducer
Vehicle Speed	Racelogic Velocity BOX 3 (VBOX3) Differential Global Positioning System (DGPS)
Vehicle position	VBOX3 DGPS
Vehicle heading	VBOX3 DGPS
Body CG lateral acceleration	Accelerometer (Crossbow 4g)
Body roll velocity	Solid state gyroscope (CRS03)
Body yaw velocity	Solid state gyroscope (CRS03)
LF suspension displacement	Linear Displacement Transducer (LDT) (Celesco)
RF suspension displacement	LDT (Celesco)
LR suspension displacement	LDT (Celesco)
RR suspension displacement	LDT (Celesco)
LF suspension force	Pressure Transducer in Suspension strut (Wika)
RF suspension force	Pressure Transducer in Suspension strut (Wika)
LR suspension force	Pressure Transducer in Suspension strut (Wika)
RR suspension force	Pressure Transducer in Suspension strut (Wika)
FR wheel angle	Potentiometer (Celesco)

The suspension forces can be measured by converting the suspension pressure into a force using the suspension strut area ($F = pA$), this excludes the friction forces present in the suspension strut joints and bushes and only represent the spring and damper forces of the suspension strut. The location of the measurement transducers are depicted in Figure 2.1.

2.1.3 Data Acquisition and Control System

The vehicle is equipped with a PC104 form factor data acquisitioning system. The system contains 16, 12bit Analog to Digital (A/D) converters; 16 digital inputs; 4 analog outputs and 16 digital outputs. The system is used to perform the data aquisitioning and signal calibrations, after which the data is sent via Ethernet to a laptop. The laptop receives both the GNSS information (via serial port), and sensor data and performs all of the complex computations. The desired actuator outputs are then sent back to the PC104 via Ethernet
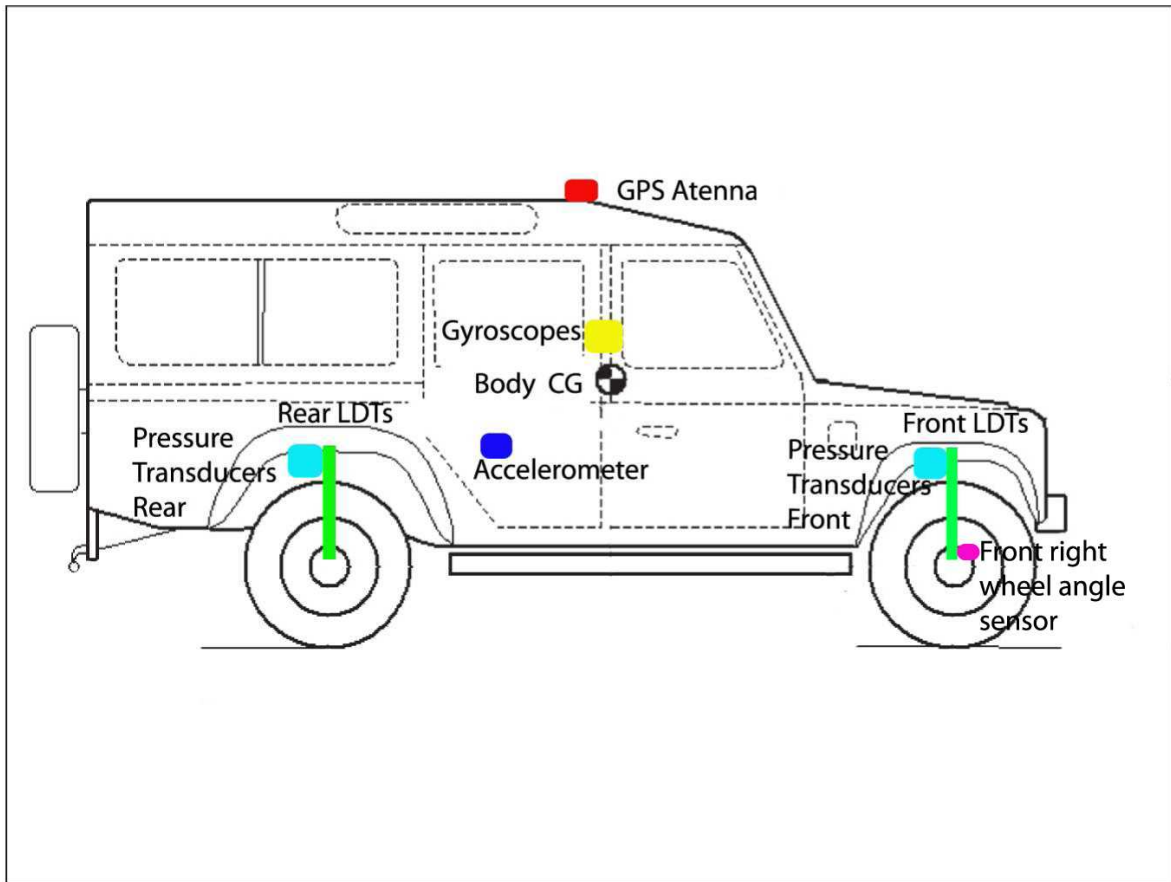
Figure 2.1: Location of measurement transducers.

which generates the analog outputs required by the actuator controllers. This process is shown graphically in the block diagram of Figure 2.2.
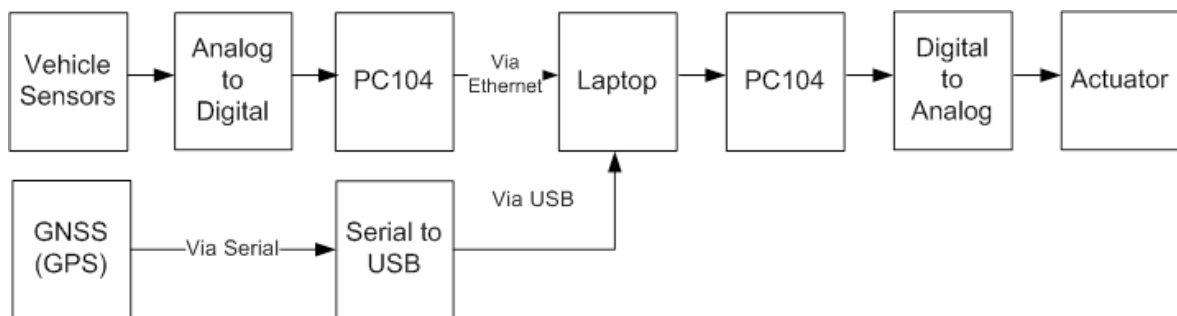
Figure 2.2: Block diagram of data acquisition and control.

2.1.4 Actuators for Autonomous Systems

All vehicle subsystems have been equipped with the necessary actuators for autonomous control. The brake pedal, clutch pedal, gear lever and accelerator pedal have been equipped with pneumatic actuators. The steering is controlled by means of a stepper motor connected between the steering wheel and steering box which provides fine and accurate control. All systems are implemented in such a manner that they are not intrusive to a driver, thus allowing the vehicle to be controlled both manually and autonomously. The driver can also immediately override all the actuators if needed. The steering subsystem is one of the main components of this study, as such the steering system will be discussed in more detail.

Steering System

The vehicle is equipped with a Festo EMMS-ST-87L stepper motor which is connected via two universal joints to the steering box of the vehicle. Nominal torque of the motor is a constant 8.6Nm up to a certain rotational speed after which a drop off in torque occurs as depicted in Figure 2.3. The stepper motor was chosen based on torque measurements made when the wheels are loaded (on the ground) and the vehicle is stationary, as well as the maximum steer rate required to perform NHTSA's fishhook test (NHTSA, 2003). The stepper motor output torque as a function of motor speed is displayed in Figure 2.3. The complete stepper motor assembly is shown in Figure 2.4 and shown installed in the test vehicle in Figure 2.5.
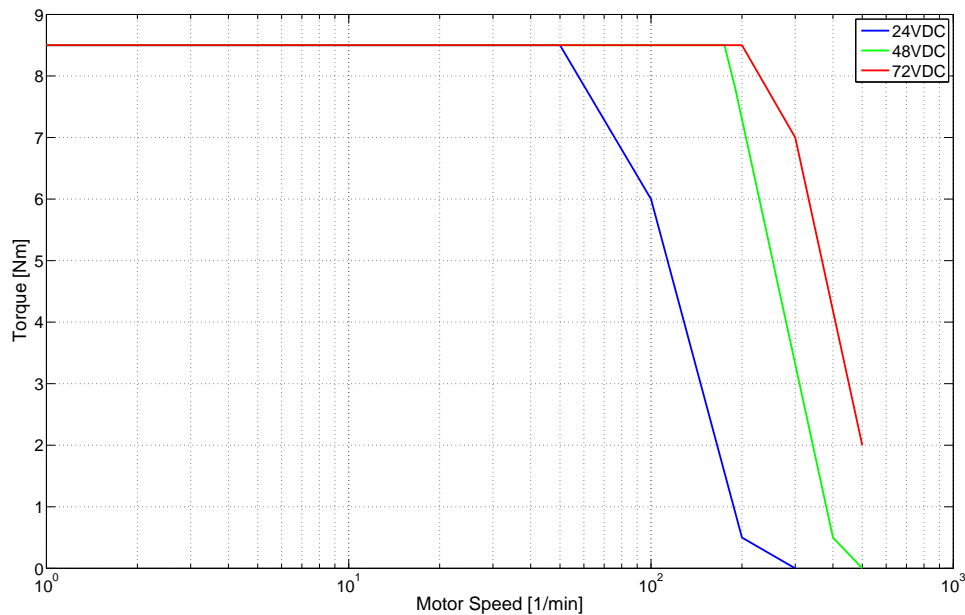
Figure 2.3: Stepper motor torque as a function of rotational speed and supply voltage (Festo, 2010).
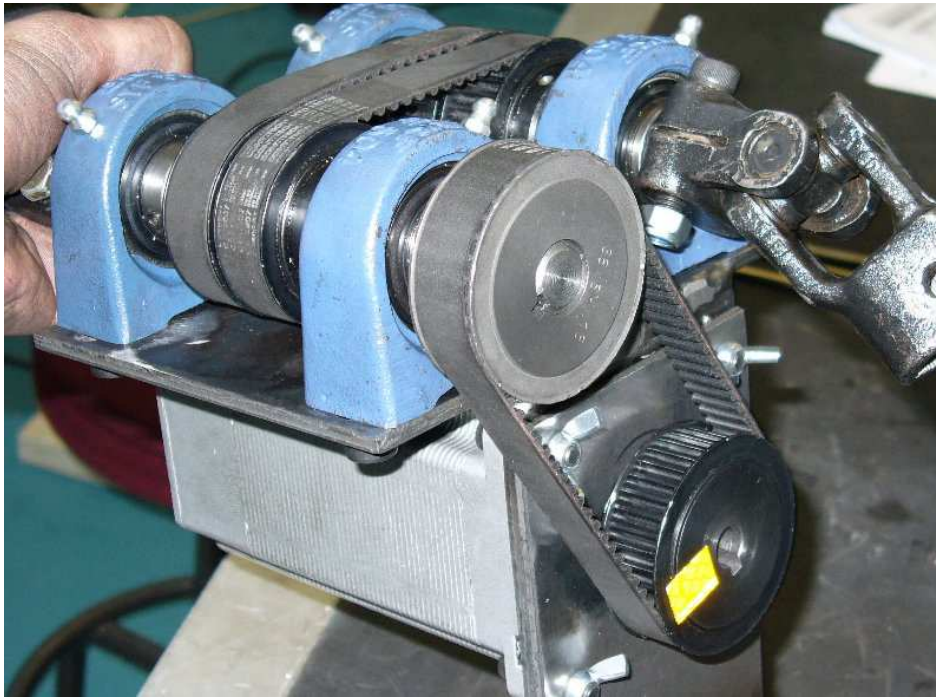
Figure 2.4: Stepper motor assembly.

Figure 2.5: Stepper motor assembly installed in engine bay.

2.2   Full Vehicle Simulation Model

A 16 degrees of freedom fully non-linear vehicle dynamics model has been developed for the
Land Rover Defender in ADAMS by Thoresson (2007) and modified by Uys et al (2007) and
Cronje (2008). The model includes the non-linear $4S_4$ spring and damper characteristics,
non-linear bump stops and bushes as well as body torsion about the longitudinal axis, all
of which have been experimentally determined. The hydro-pneumatic $4S_4$ suspension unit
is modelled as a adiabatic process, thus it includes thermal effects inside the system, with
the assumption of no heat transfer to and from the surrounding environment. A graphical
representation of the full model is shown in Figure 2.6.
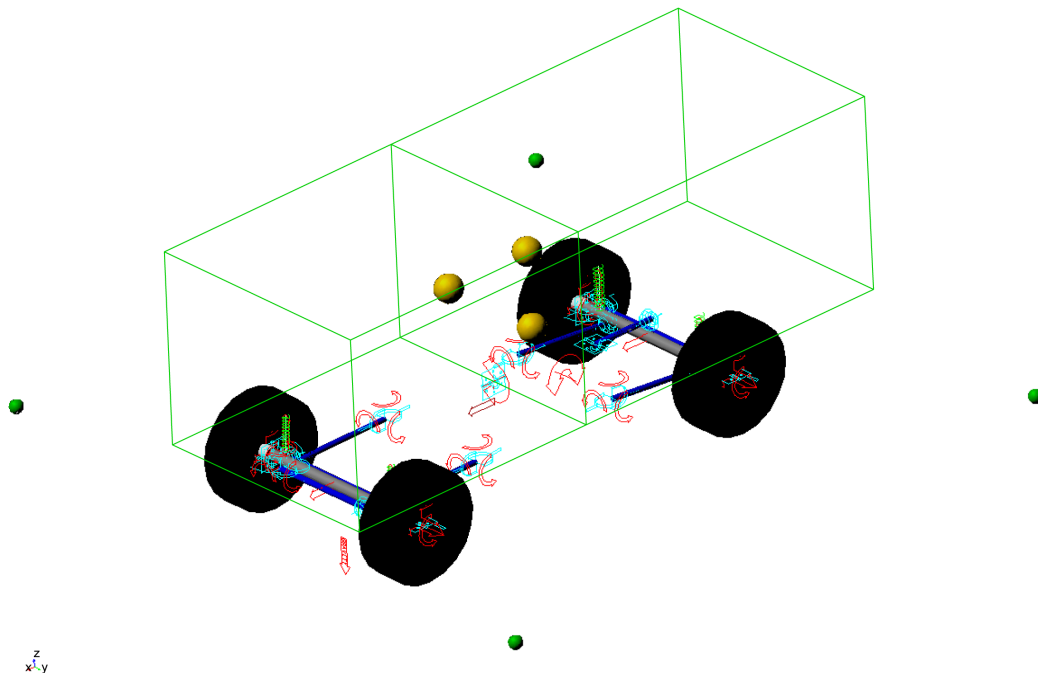
Figure 2.6: Graphical view of vehicle Modelled in ADAMS.

The front suspension consists of a rigid axle fixed longitudinally to the chassis via two leading
arms with rubber bushes. The rigid axle is located laterally with a Panhard rod. Figure 2.7
depicts the front suspension modelled in ADAMS, showing all connections and reaction forces.

The rear suspension incorporates a rigid axle fixed longitudinally by two trailing arms.
An A-arm constrains the rigid axle laterally via a spherical joint on the axle and bushes on
the chassis. The anti-roll bar is modelled as a torsional spring. Figure 2.8 shows the layout
of the suspension as modelled in ADAMS.

The ADAMS model is linked to Simulink (MathWorks, 2010) allowing for easier modeling
of the non-linear $4S_4$ suspension system with included non-linear friction. The Simulink
environment also provides an excellent platform for the development of a steering controller.
As mentioned in section 1.3.1 the tyre road interface is modelled using the Pacejka 89 tyre
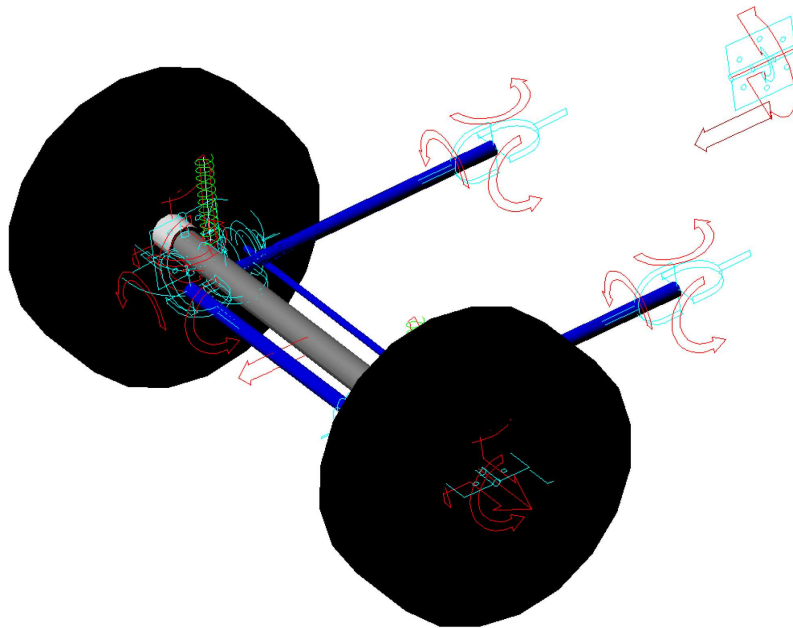
Figure 2.7: Front suspension of vehicle modelled in ADAMS.
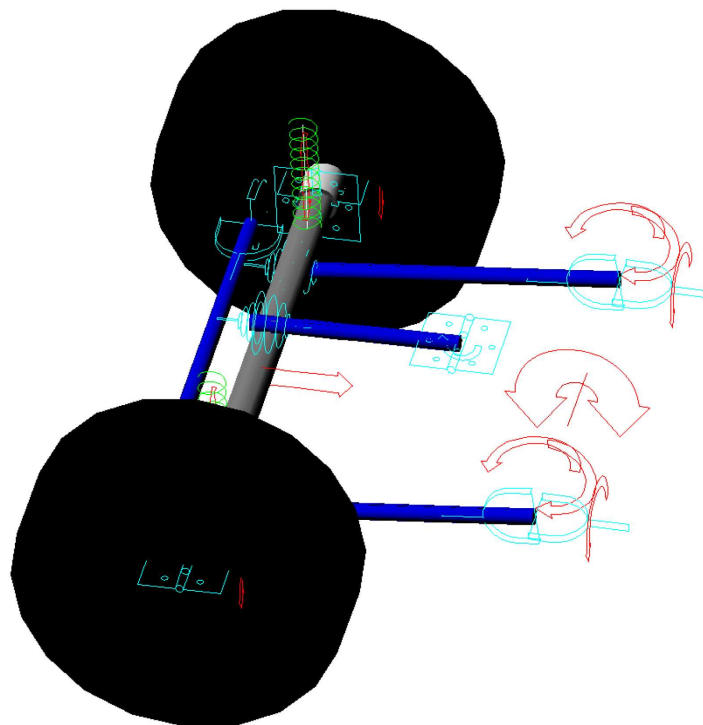
Figure 2.8: Rear suspension of vehicle modelled in ADAMS.

model (Pacejka, 1989) as implemented in ADAMS using parameters which were previously fine tuned (Thoresson, 2007). The longitudinal force and self-aligning moment characteristics of the tyres are excluded (in order to keep the model as simple as possible, yet as complex as necessary and due to lack of data). Some modifications to the full vehicle model included relocation of the driving force to reduce the yaw moment caused by the driving force. For the simulations to evaluate the driver model, the sampling frequency of vehicle parameters such as yaw rate, lateral acceleration was changed to coincide with the sampling frequency of the data acquisitioning device (100Hz). The sampling frequency of vehicle position was changed to coincide with the sampling frequency of the global navigation satellite systems used to provide position feedback (50Hz). This was done to incorporate the sampling frequency of the various data in the simulations.

2.3 Full Vehicle Model Validation

This study is only concerned with the lateral vehicle dynamics and, as such, the model will only be validated for lateral motions including body roll. Validation is achieved by comparing simulation results with experimental results while performing a Double Lane Change (DLC) manoeuvre according to ISO 3888 (1999).

2.3.1 Procedure

Validation is carried out by experimentally performing a severe DLC at various entry speeds (such as 40, 60 and 80km/h). All the parameters in Table 2.1 are measured. The measured vehicle speed and front steering angle are then low-pass filtered to remove high frequency noise and used as inputs to the simulation model as they represent inputs given to an actual vehicle by a human driver. Simulation results are compared to the measured parameters provided in Section 2.1.2 to determine the correlation.

2.3.2 Validation Through DLC at 55km/h

Figure 2.9 displays the steering and vehicle speed inputs, obtained from measurements, to the simulation model. The entry speed to the DLC is observed to be 55km/h. Figure 2.10 shows the correlation of simulation results used when evaluating lateral vehicle dynamics. The correlation shows a mixture of accelerations, velocities as well as displacements. It can be observed that good correlation is obtained from all vehicle parameters. If one also considers that good correlation is obtained from both the yaw angle (top right graph where both VBox GPS and integration of the yaw rate is used) and the absolute position (bottom right graph) it can be concluded that the simulation model gives good correlation to the physical vehicle at 55km/h.

Figure 2.9: Steering and speed inputs to simulation model through DLC at 55km/h.
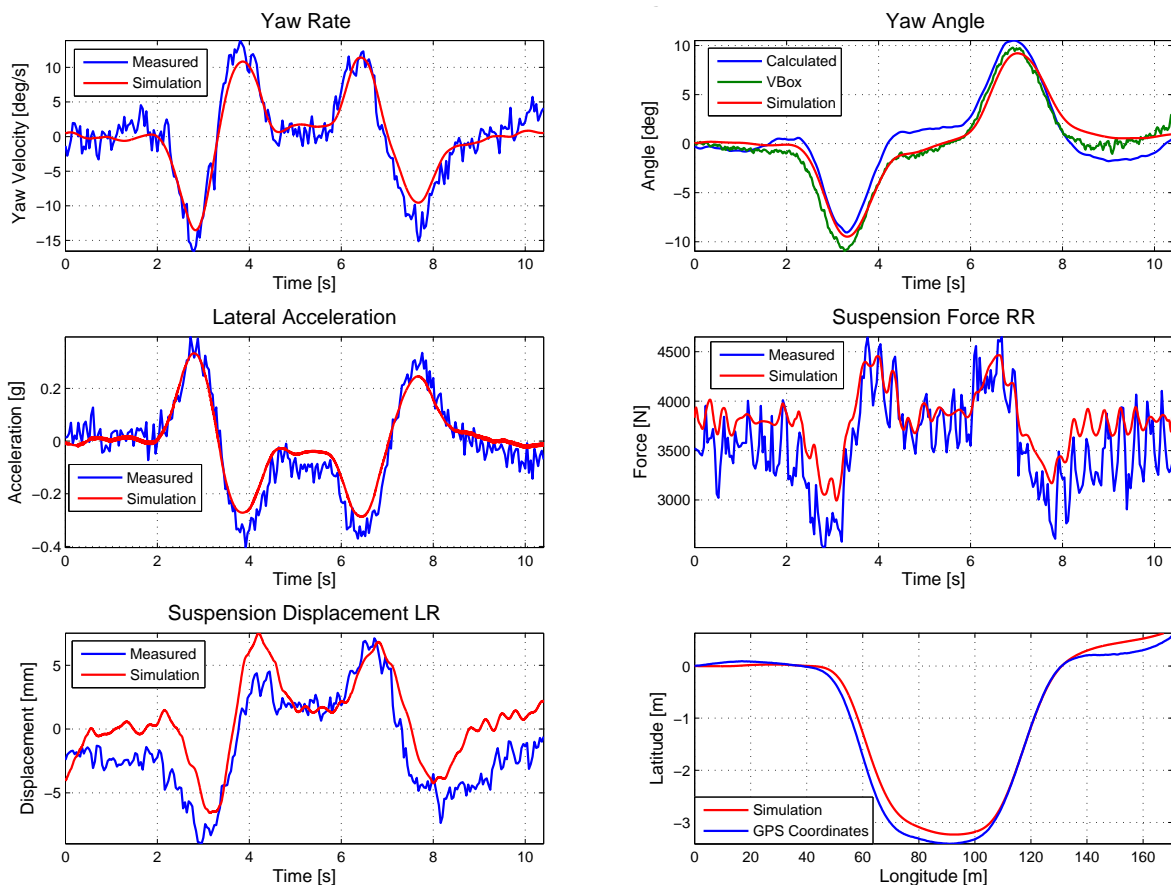
Figure 2.10: Correlation of measured parameters through DLC at 55km/h.

2.3.3 Validation Through DLC at 73.5km/h

Figure 2.11 displays the steering and vehicle speed inputs, obtained from measurements, to the simulation model. Figure 2.12 shows the correlation of most vehicle parameters used when evaluating lateral vehicle dynamics. The correlation shows a mixture of accelerations, velocities as well as displacements.
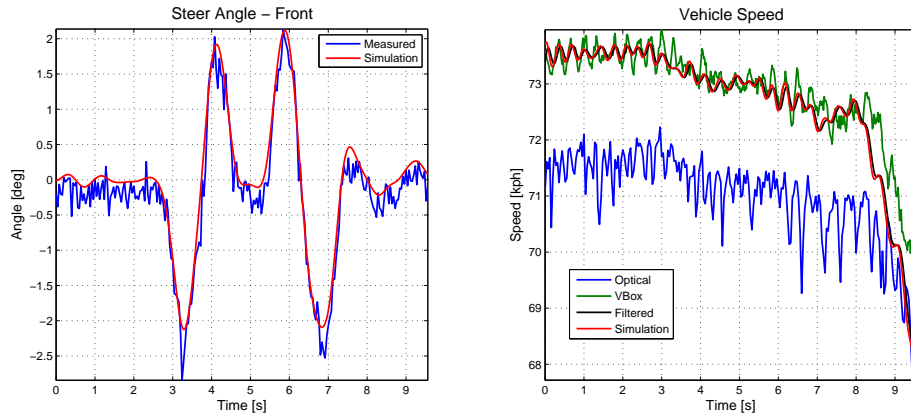
Figure 2.11: Steering and speed inputs to simulation model at 73.5km/h.
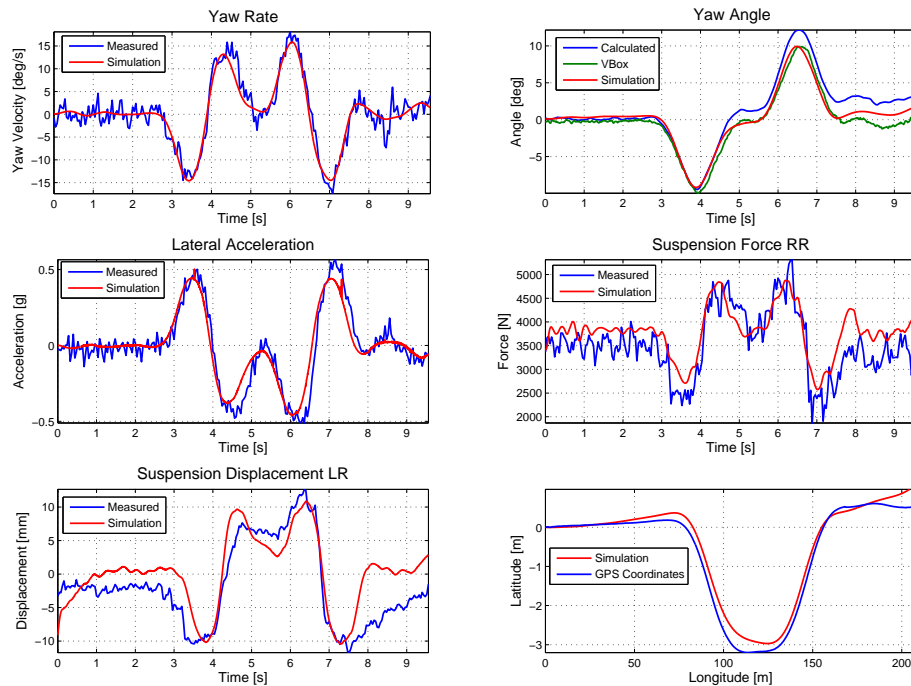
Figure 2.12: Correlation of measured parameters at 73.5 km/h.

To determine the degree of validation the relative error between the peaks on the measured and simulated data were determined. To remove the noise present (as can be seen by the regions prior to any steer input) the data was first filtered through a 2.5Hz low-pass filter. The calculated maximum relative error is tabulated in Table 2.2.

Table 2.2: Maximum relative error on peaks of correlation data.

Speed	Maximum Relative Error [%]					
	Yaw Rate	Yaw Angle	Lateral Acceleration	Suspension Force RR	Suspension Displacement LR	Path
55km/h	16.07	15.06	17.00	10.67	60	5.16
73.5km/h	5.05	0.27	15.38	7.67	26.20	7.20

The greater deviation in displacement correlation can be attributed to an error in the static equilibrium values, as well as, the error in the modelling of the friction in the suspension system. The trend is however the same and a vertical shift of one of the plots would most likely yield better correlation.

At 55km/h the maximum relative error of all plots is around 15% on the peaks, while the maximum peak error on other plots are closer to 10%. There is also no visible phase shift between the two data sets. The error can thus be said to be between 10-15%. almost all maximum errors at 73.5km/h is smaller compared to 55km/h errors. Considering also that both yaw angle and vehicle position have small relative errors, it can be concluded that good correlation is obtained with an acceptable error between 10-15%. Especially the correlation with the yaw angle and the vehicle position which is very difficult to achieve, is excellent.

2.4 Conclusion

The vehicle used for this study is equipped with all the necessary instrumentation that allows for the assessment of vehicle handling, as well as performing autonomous steering. The simulation model has been validated for handling and therefore provides an excellent platform to design a driver model which is to be experimentally validated. Correlation between vehicle tests and simulation results are excellent.

Chapter 3

Inverse Magic Formula Steering Controller

The use of driver models in simulations are essential when performing closed loop vehicle handling manoeuvres. Thoresson (2007) required a robust driver model to optimise the suspension parameters (spring and damping characteristics) of the 4S$_4$ system for various conditions in ADAMS. However, as discussed in Chapter 1, the determination of gains for most driver models to yield stable control at high speeds and accurate control at low speeds becomes a difficult task. This problem is compounded by the fact that suspension parameters are changed over a wide range. Taking all these effects into account is important for autonomous control as many modern vehicles are also fitted with controllable suspension systems, such as semi-active dampers or active anti-roll bars. The fact that an off-road vehicle, with high CG, is considered further complicates the problem. Thoresson (2007) investigated the relationship between the vehicle yaw response and the non-linear tyre characteristics. He proposed the fitting of the Magic Formula, normally used for tyre modeling, to the non-linear response of the vehicle's yaw acceleration vs. steering rate and vehicle speed. In traditional driver models the relationship between the steer angle and yaw rate is used for vehicle control. In these controllers the vehicle yaw angle and yaw rate is used to approximate the yaw angle a distance ahead. By making use of the yaw acceleration the accuracy of the approximated preview yaw angle is improved. The study will show that a relationship between the steer rate and yaw acceleration exists which can be used for control purposes. Thoresson (2007) also concluded that the feasibility of single point preview was ensured by the fact that the non-linear tyre characteristics is replicated for the steering gain parameter. The implementation and modifications made to this driver model for the purpose of autonomous path following, as required for this study, are discussed in this chapter.

3.1 Yaw Acceleration vs. Steer Rate

To investigate the relationship between the vehicle's yaw acceleration response and steering inputs, simulations were performed for various steering rate inputs at various vehicle speeds. The result of some of these simulations are displayed in Figure 3.1.
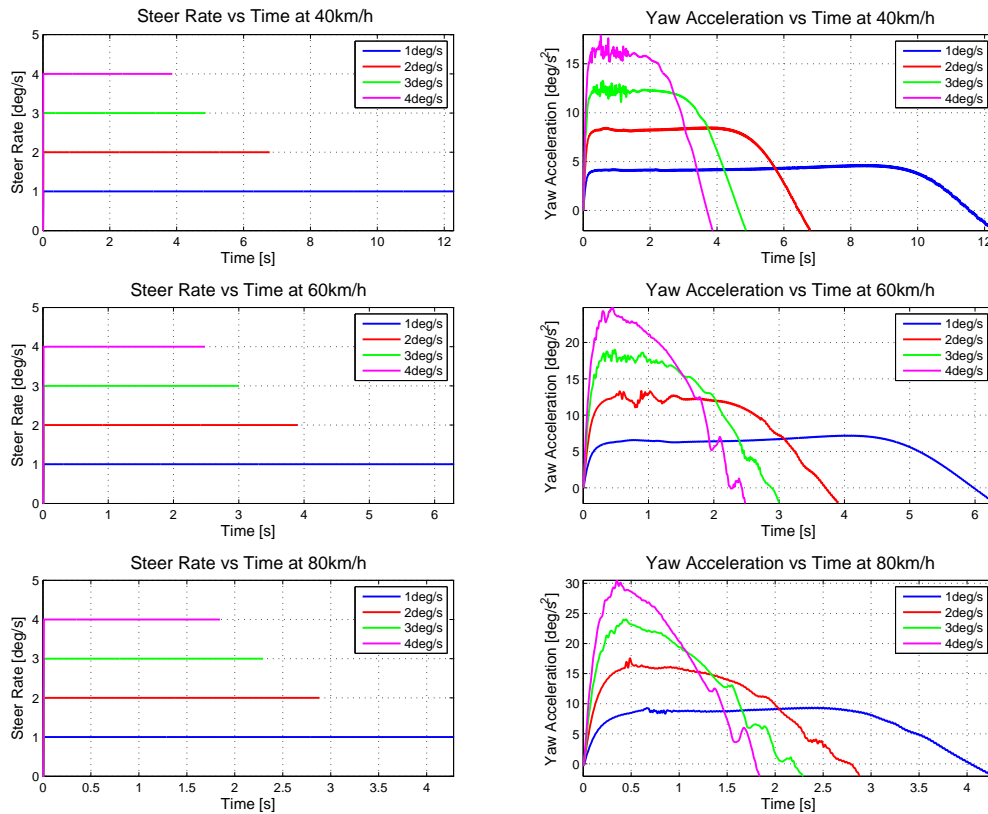
Figure 3.1: Yaw Acceleration response for various vehicle speeds and steering rates

The plots indicate that the yaw acceleration attains a constant value for a significant part of the duration of the simulation, for a specific steer rate and vehicle speed, for almost all steer rates at low speeds and low steer rates at high speeds. It can also be noted that the response becomes larger as vehicle speed increases for the same steer rate. This increase in sensitivity is well known with modern vehicles equipped with speed dependent power steering reducing the power assist as vehicle speed increases. As a result of the increase in sensitivity, lower steer rates at higher speeds are put into the vehicle. Thus, the use of lower steer rates at higher speeds ensures that the yaw acceleration response still obtains a constant value for a significant part of the input duration. These constant values of the responses suddenly reduces towards the end of the test. This sudden reduction is most likely due to the tyre reaching its saturation level. Since both the steer rate and vehicle speed would influence the time to reach tyre saturation, the yaw acceleration was subsequently plotted against lateral

acceleration rather than time. The lateral acceleration also gives a measure of the level of tyre saturation.

Figure 3.2 shows the yaw acceleration vs. lateral acceleration as a function of steer rate for different vehicle speeds. The figure better illustrates the near constant response obtained by the yaw acceleration. The response stays constant up to very high lateral accelerations after which a sudden drop occurs indicating that the tyre force is saturating.
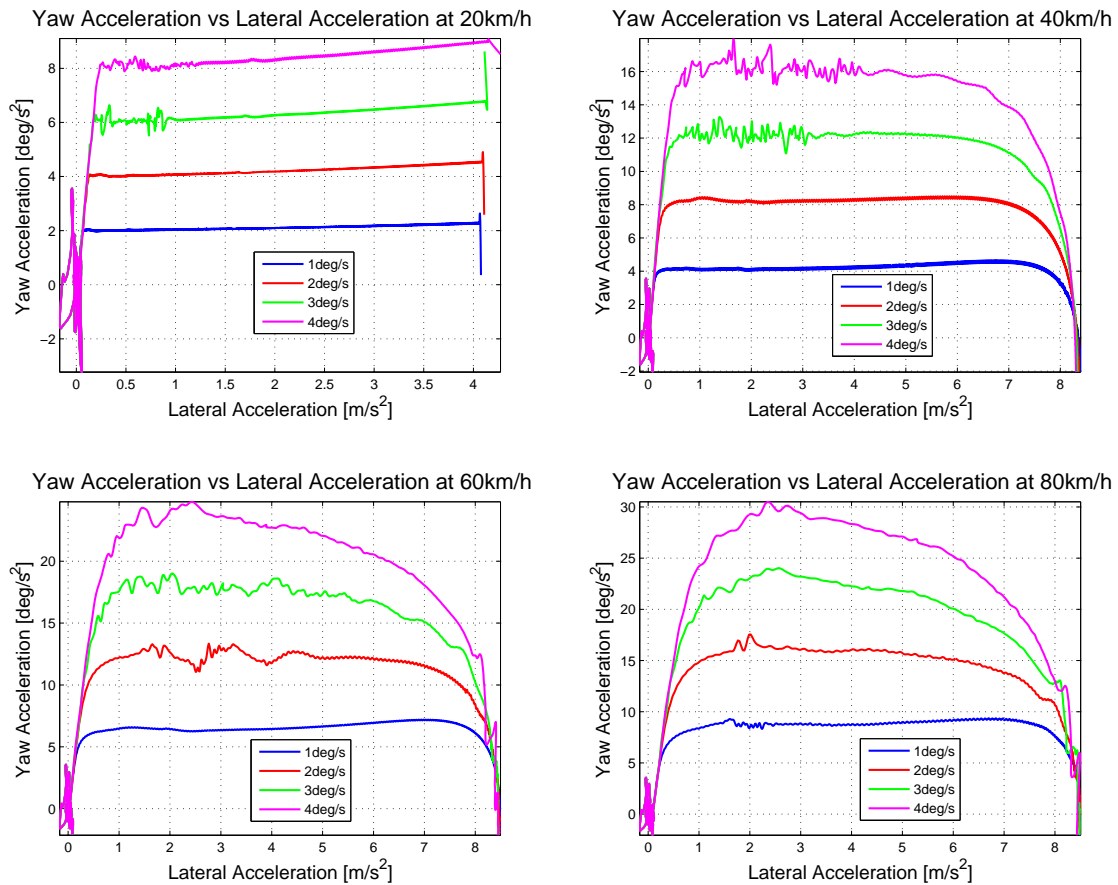
Figure 3.2: Yaw Acceleration vs lateral acceleration for various vehicle speeds and steering rates

Reymond et al (2001), as well as Hugemann and Nickel (circa 2002) showed that normal drivers typically reached larger lateral acceleration as vehicle speeds increased. This increase was however only up to a certain speed. After this speed drivers tended to reach lower lateral accelerations with increasing speed to increase the safety margin available to them. In their tests conducted during normal driving the lateral acceleration seldom exceeded 6m/s^2. Thus, the normal operating lateral accelerations of a vehicle can be considered to be below 6m/s^2. If it is considered that the yaw acceleration response remains fairly constant below lateral acceleration of 6m/s^2, it can be said that the yaw acceleration obtains a steady state response during normal operating conditions for a specific vehicle speed and steer rate.

It is thus possible to obtain the steady state yaw acceleration response as a function of steer rate and vehicle speed (depicted in Figure 3.3 (Thoresson, 2007)). The relationship can be noted to be fairly linear at low speeds - confirming that linear vehicle models are sufficient in the region of low speeds. However, the relationship becomes non-linear with increasing vehicle speed as well as steer rate at higher vehicle speeds. The relationship is thus non-linear with respect to both vehicle speed and steer rate. It was however evident to Thoresson (2007)
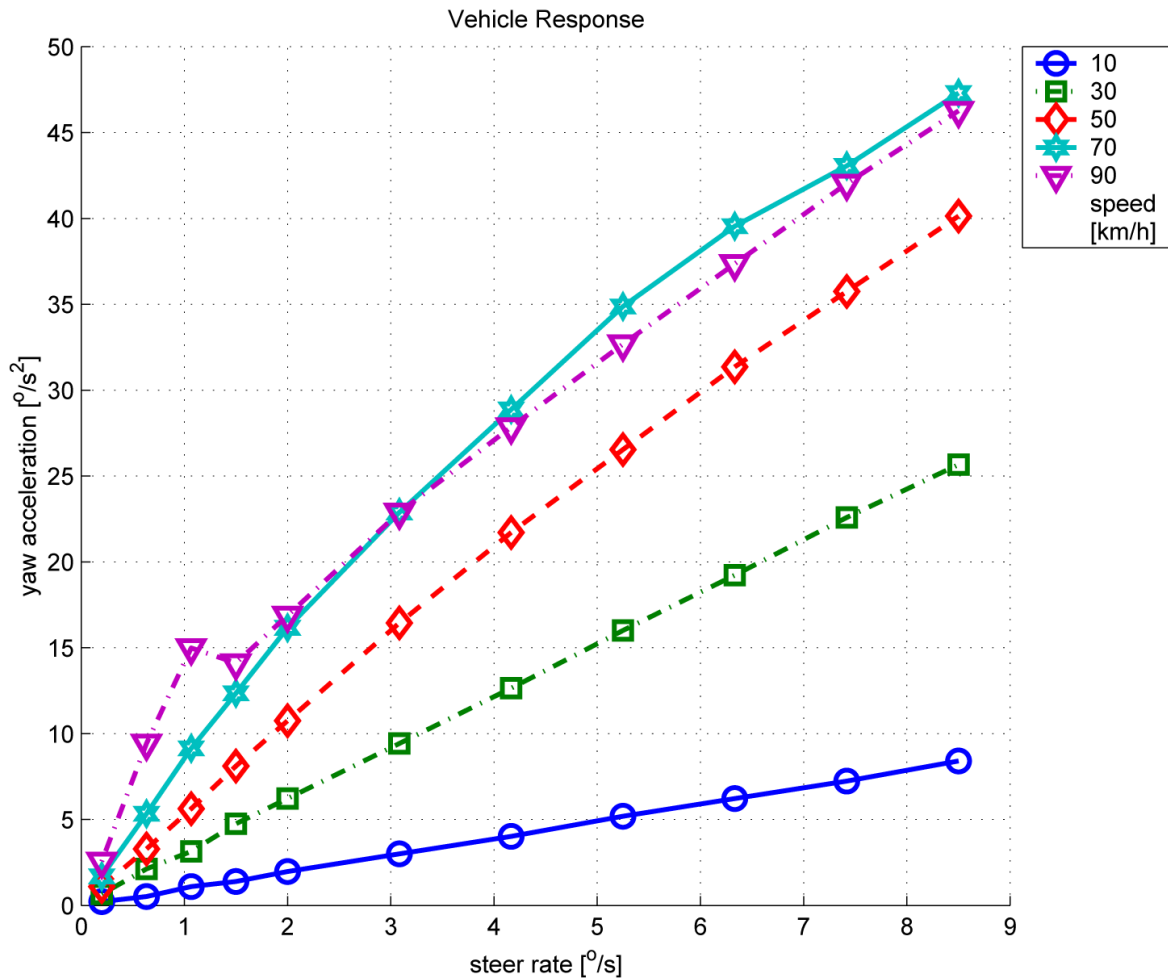
Figure 3.3: Yaw Acceleration vs lateral acceleration for various vehicle speeds and steering rates (Thoresson, 2007).

that the relationship was similar to the relationship of tyre lateral force vs. side-slip angle as a function of vertical load as depicted in Figure 3.4. This relationship is widely modelled by means of the non-linear Magic Formula (Bakker et al, 1989). With this discovery, Thoresson (2007) decided to implement the proposed novel driver model, with the non-linear gain factor modelled with the Magic Formula.
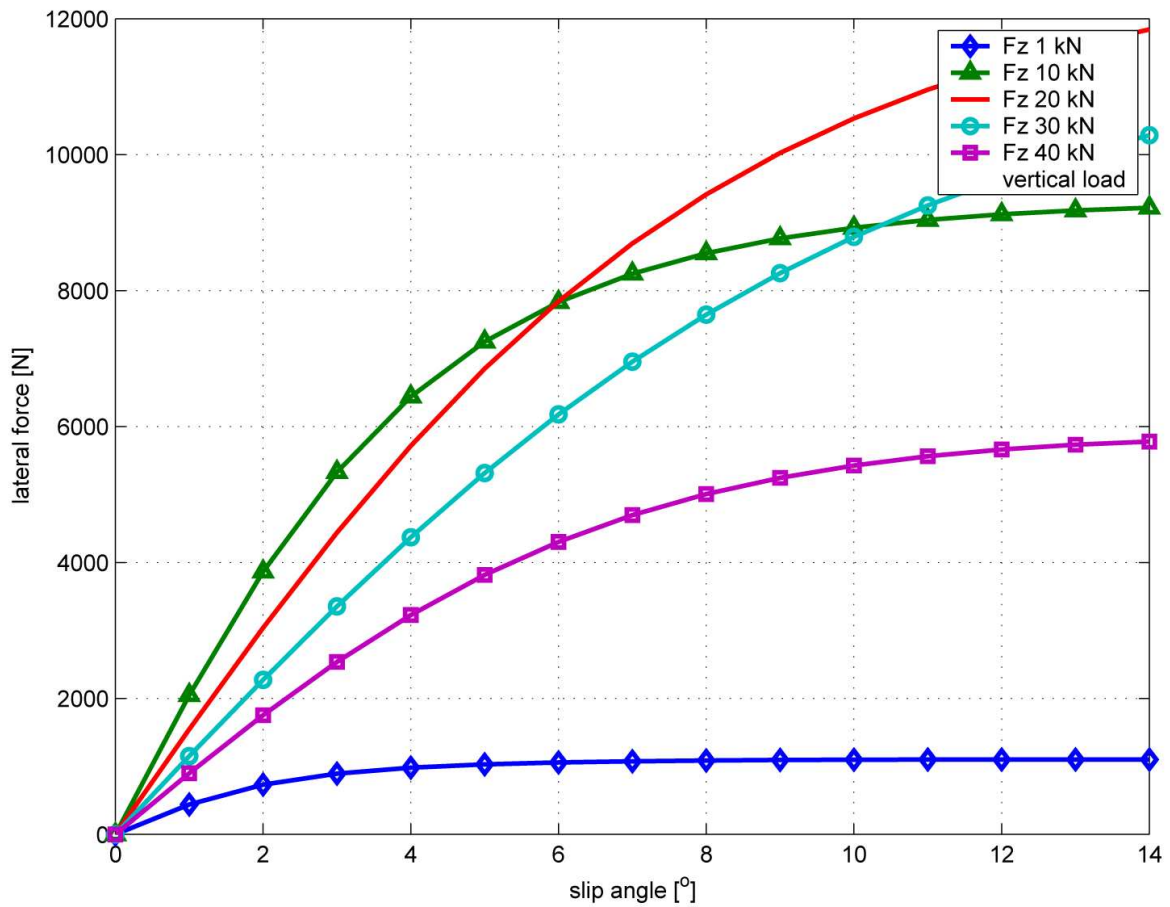
Figure 3.4: Tyre lateral force vs. side-slip angle as a function of vertical load (Thoresson, 2007).

3.2 Magic Formula Fits

According to Thoresson (2007), the Magic Formula (1.1), can be successfully fitted to the yaw acceleration vs. steer rate and vehicle speed relationship by redefining the parameters as:

- vertical tyre load F_z is equivalent to vehicle speed $\dot{x}$

- tyre side-slip angle β is equivalent to steering rate $\dot{\delta}$

- tyre lateral force F_y is equivalent to vehicle yaw acceleration $\ddot{\psi}$.

The Magic Formula presented in Equation 1.2 can now be used to fit the model with parameters Y and X defined as:

- $Y(X)$ = yaw acceleration $\ddot{\psi}$

- X = steering rate $\dot{\delta}$

The parameters of the fit can either be obtained by a simple optimisation process or by following the process outlined by Bakker et al (1989). The fit of the Magic Formula to the yaw acceleration vs. steer rate and vehicle speed relationship is shown in Figure 3.5. From this figure it can be concluded that the Magic Formula can successfully be used to represent this relationship.
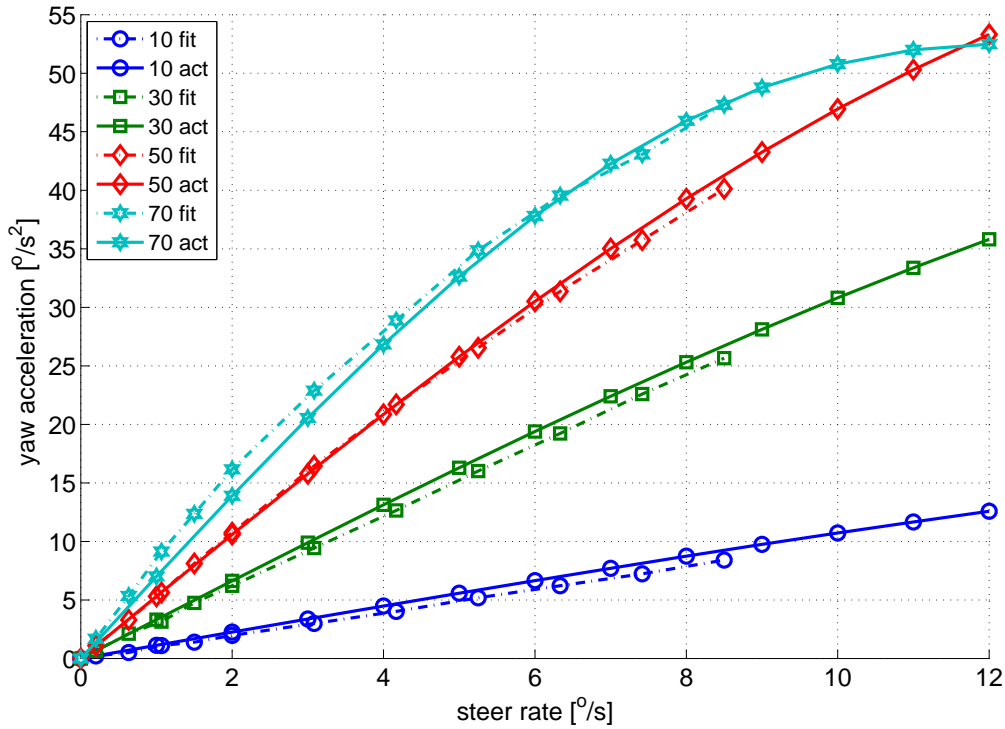
Figure 3.5: Magic Formula fit to the yaw acceleration response as a function of both speed and steer rate (Thoresson, 2007).

The vehicle's steady state yaw acceleration response as a function of both speed and steer rate as obtained (Figure 3.5) was fitted with the Magic Formula with yaw acceleration as the output. For steering control it is however required to have the steer rate as the subject of the equation. However, due to the nature of the magic formula this is not possible. To circumvent this problem the arctan function in (1.1) was replaced with the pseudo arctan function as suggested by Pacejka (2002) as:

$$\text{psarctan(x)} = \frac{2(1 + a|x|)}{1 + 2(b|x| + ax^2)/\pi} \tag{3.1}$$

Initially Thoresson (2007) solved the equation symbolically using MATLAB's (MAtrix LABoratory (MathWorks, 2011)) symbolic toolbox for the steer rate. The resulting equation has three solutions each representing different parts of the graph and containing multiple terms. The solution is taken as the first part of the graph up to a peak value. The peak value is kept

for any steer rate beyond the peak value. Due to the size and the complexity of the resulting equation it is not represented here. The inverse model of the Magic Formula equation used to obtain a steer rate from a desired yaw acceleration and vehicle speed, is termed the Inverse Magic Formula Model in this study.

Implementation of such a long complex equation in a real-time control loop that needs to be executed at a predetermined frequency presents a problem. The solution to this was to curve fit the relationship by using a Feed Forward Neural Network (FFNN). It was found that a simple 3 layered (Input, Hidden and Output layers) network with 20 hidden nodes was sufficient enough to represent the much more complex solution (see Figure 3.6). This modification to Thoresson's (2007) original controller, presented in this study, not only makes the implementation much simpler but was also found to improve computational efficiency.
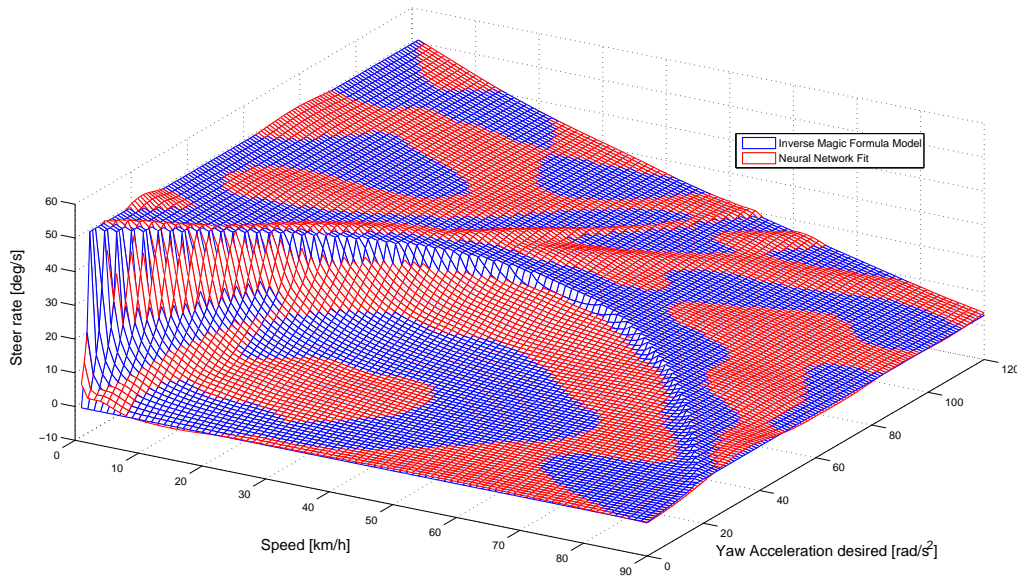
Figure 3.6: Neural network fit of the Inverse Magic Formula.

3.3 Yaw Angle Controller

Using the relationship obtained in section 3.2 it was postulated that the vehicle's yaw angle can be controlled by comparing the actual yaw acceleration with the desired yaw acceleration. From dynamic principles the rotation angle ψ of a rigid body is dependant on the current rotation angle ψ_0, the yaw rate $\dot{\psi}$, the yaw acceleration $\ddot{\psi}$, as well as the time step τ. If the acceleration is not constant, but a sufficiently small time step is used, then the rotation angle can be sufficiently predicted as follows:

$$\psi_p = \psi_a + \dot{\psi}\tau + \frac{1}{2}\ddot{\psi}\tau^2 \tag{3.2}$$

Considering Figure 3.7 the parameters can be defined as:

- ψ_p, predicted yaw angle after time step ,

- ψ_d, desired yaw angle at $d_{preview}$,

- ψ_a, actual vehicle yaw angle,

- $\dot{\psi}$, actual vehicle yaw rate,

- $\ddot{\psi}$, actual vehicle yaw acceleration.
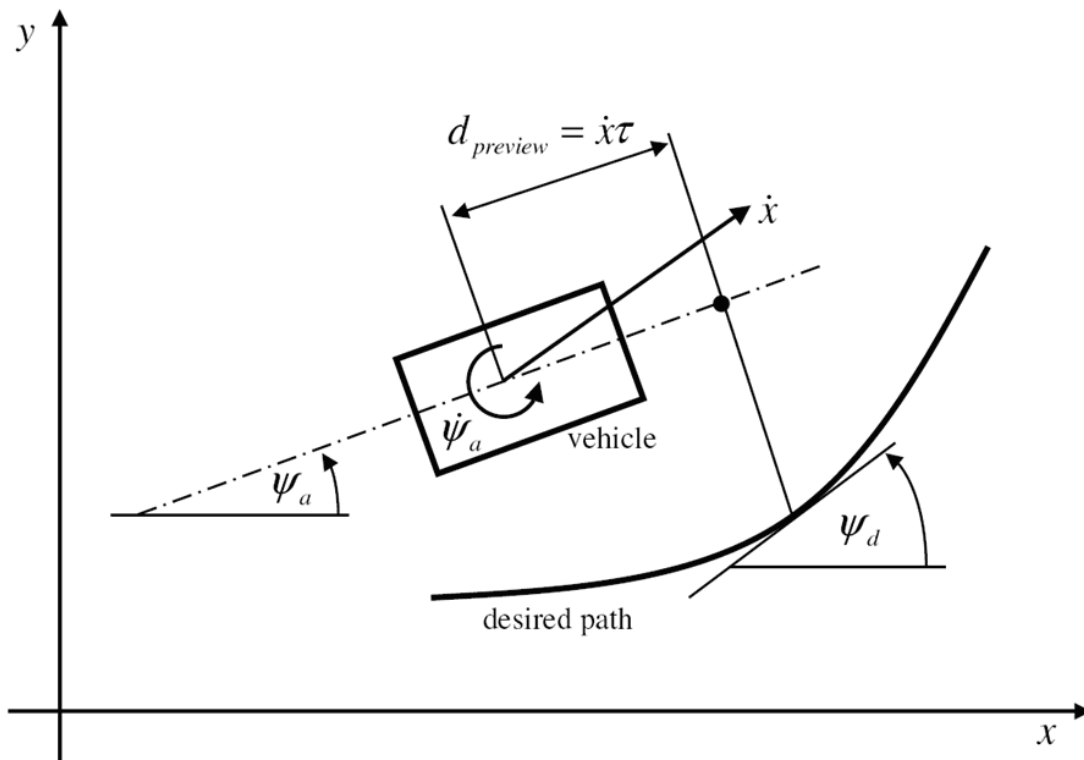
Figure 3.7: Definition of driver model parameters (Thoresson, 2007).

Thus, the desired yaw acceleration needed to obtain a desired angle of rotation ψ_d at the next time step, is as follows:

$$\ddot{\psi} = 2\frac{\psi_d - \psi_0 - \dot{\psi}\tau}{\tau^2} \tag{3.3}$$

The yaw angle of the vehicle can thus be controlled by determining a required yaw angle change ($(\psi_d - \psi_0)$ or yaw angle error) and by measuring the current yaw rate. Form this

a required yaw acceleration can be determined to provide the necessary yaw angle change. The yaw acceleration can then be translated into a required steering rate input at a specific vehicle speed by using the relationship developed in Section 3.2 as:

$$\dot{\delta}_{\psi,FFNN} = FFNN(\ddot{\psi}, \dot{x}) \tag{3.4}$$

This driver model attempts to hold the vehicle yaw angle equal to the path angle i.e. keep the vehicle parallel to the prescribed path.

3.4 Lateral Position Control

Another modification, made to Thoresson's (2007) driver model in this study was the inclusion of a controller which minimises the cross-track (or lateral position) error. It is evident that the yaw angle controller described in section 3.3 attempts to make the vehicle path parallel to that of the desired path. If the vehicle starts on the desired path then both paths should be the same. However, due to the accumulation of errors the vehicle path could be parallel but have some lateral offset to that of the desired path. As a result of this, the controller is complimented with a controller that minimises the cross-track error at a preview distance ahead of the vehicle (see Figure 3.8).

A Proportional Derivative (PD) controller on the cross-track error (e_{lat}) is implemented as:

$$\dot{\delta}_{e_{lat}} = K_p e_{lat} + K_d \frac{de_{lat}}{dt}, \tag{3.5}$$

where $\dot{\delta}$ is the steer rate, and K_p and K_d are the proportional and derivative gains respectively.

As mentioned, the steering becomes more sensitive as the vehicle speed increases, this is also evident from Figure 3.3 as the yaw acceleration response for a certain steer rate increases with vehicle speed. It is thus necessary to introduce a form of gain scheduling to compensate for the vehicle's longitudinal speed and thus improve stability. Equation 3.5 can therefore be rewritten as:

$$\dot{\delta}_{e_{lat}} = f_{K_p}(\dot{x})e_{lat} + f_{K_d}(\dot{x})\frac{de_{lat}}{dt}, \tag{3.6}$$

where $f_{K_p}(\dot{x})$ and $f_{K_d}(\dot{x})$ are the proportional and derivative gains which are now a function of vehicle speed ($\dot{x}$) respectively. The gain scheduling function will be defined later in section 4.3.

The final output of the controller is the sum of the two controller outputs given by:

$$\dot{\delta} = \dot{\delta}_{e_{lat}} + \dot{\delta}_{\psi,FFNN} \tag{3.7}$$

A block diagram is provided in Figure 3.9 to graphically illustrate the controller operation.
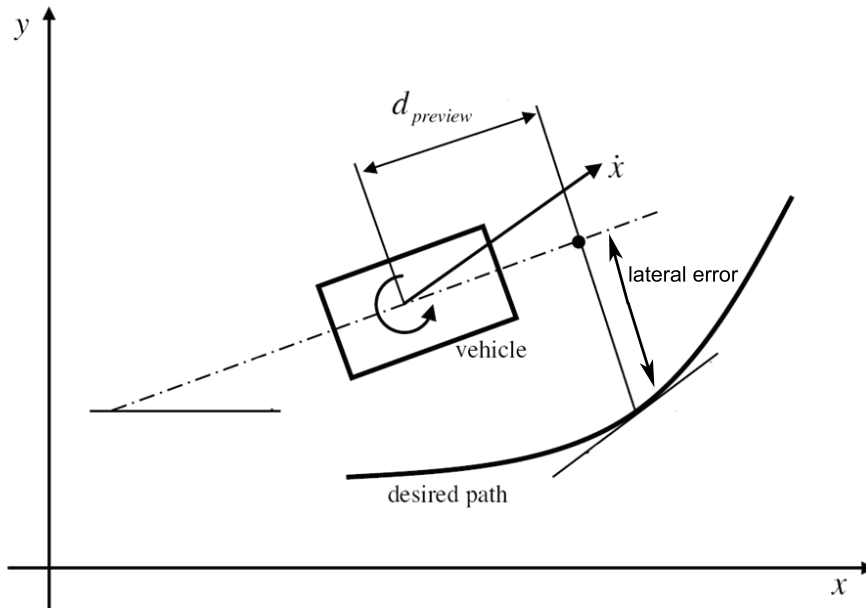
Figure 3.8: Definition of lateral driver model parameters.
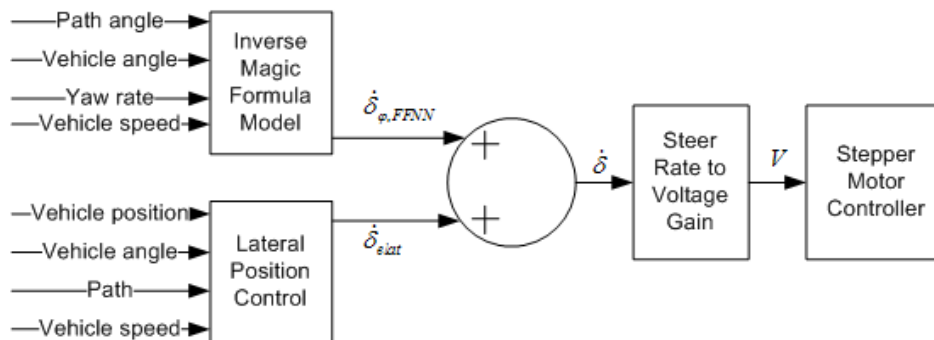
Figure 3.9: Block diagram of controller.

3.5   Driver Model Test Roads

To evaluate the proposed driver model, the full vehicle model with newly developed steering control is tasked with following three different paths. Each of the three paths are used to evaluate certain performance criteria of the driver model. These three paths include:

- Severe Double Lane Change defined by ISO3888-1 (1999)

- Sinusoidal path with constant amplitude but increasing frequency

- Constant radii S-curve

3.5.1 Double Lane Change

The double lane change manoeuvre is a manoeuvre which simulates real life obstacle avoidance or severe overtaking manoeuvres. The manoeuvre is often used as a measure of both handling and rollover sensitivity as it excites almost all dynamics while providing very little time for the vehicle to reach a steady state. This makes it ideal to test a steering controller which is based on a steady state response. Figure 3.10 depicts DLC course layout as defined by ISO38888-1 (1999). This test is defined for left hand drive vehicles, thus, during the experiments this layout will be flipped laterally for the right hand drive experimental vehicle. The dimensions of the sections are tabulated in Table 3.1
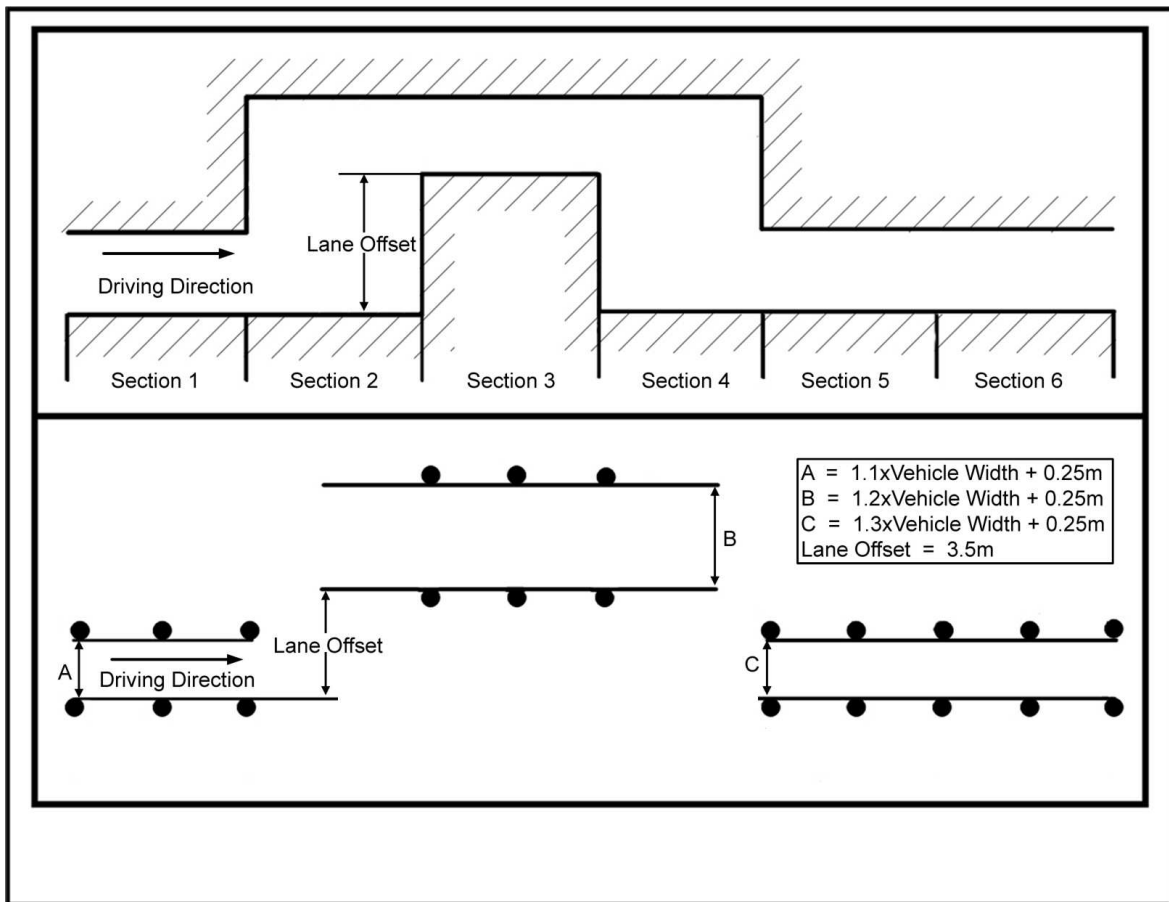
Figure 3.10: Double lane change course layout.

Table 3.1: Dimension of double lane change.

Section	Length	Width	Actual Values Used in Tests
1	15m	1.1×vehicle width + 0.25m	2.23m
2	30m	Not Applicable	Not Applicable
3	25m	1.2×vehicle width + 0.25m	2.41m
4	25m	Not Applicable	Not Applicable
5	15m	1.3×vehicle width + 0.25m	2.59m
6	15m	1.3×vehicle width + 0.25m	2.59m
Lane offset	3.5m	Not Applicable	Not Applicable

Genta (1997) presents an analytical equation for the path and heading through a DLC, given as:

$$\begin{cases} Y = 0 & \text{for } X < 15 \\ Y = \frac{3.5}{2}\left\{1 - \cos\left[\frac{\pi}{30}(X - 15)\right]\right\} & \text{for } 15 \leq X \leq 45 \\ Y = 3.5 & \text{for } 45 \leq X \leq 70 \\ Y = \frac{3.5}{2}\left\{1 + \cos\left[\frac{\pi}{30}(X - 70)\right]\right\} & \text{for } 70 \leq X \leq 95 \\ Y = 0 & \text{for } 95 \leq X \leq 125 \end{cases} \tag{3.8}$$

$$\begin{cases} \psi = 0 & \text{for } X < 15 \\ \psi = \arctan\left\{\frac{3.5\pi}{60}\sin\left[\frac{\pi}{30}(X - 15)\right]\right\} & \text{for } 15 \leq X \leq 45 \\ \psi = 0 & \text{for } 45 \leq X \leq 70 \\ \psi = -\arctan\left\{\frac{3.5\pi}{50}\sin\left[\frac{\pi}{30}(X - 70)\right]\right\} & \text{for } 70 \leq X \leq 95 \\ \psi = 0 & \text{for } 95 \leq X \leq 125 \end{cases} \tag{3.9}$$

The result of these equations are presented in Figure 3.11.
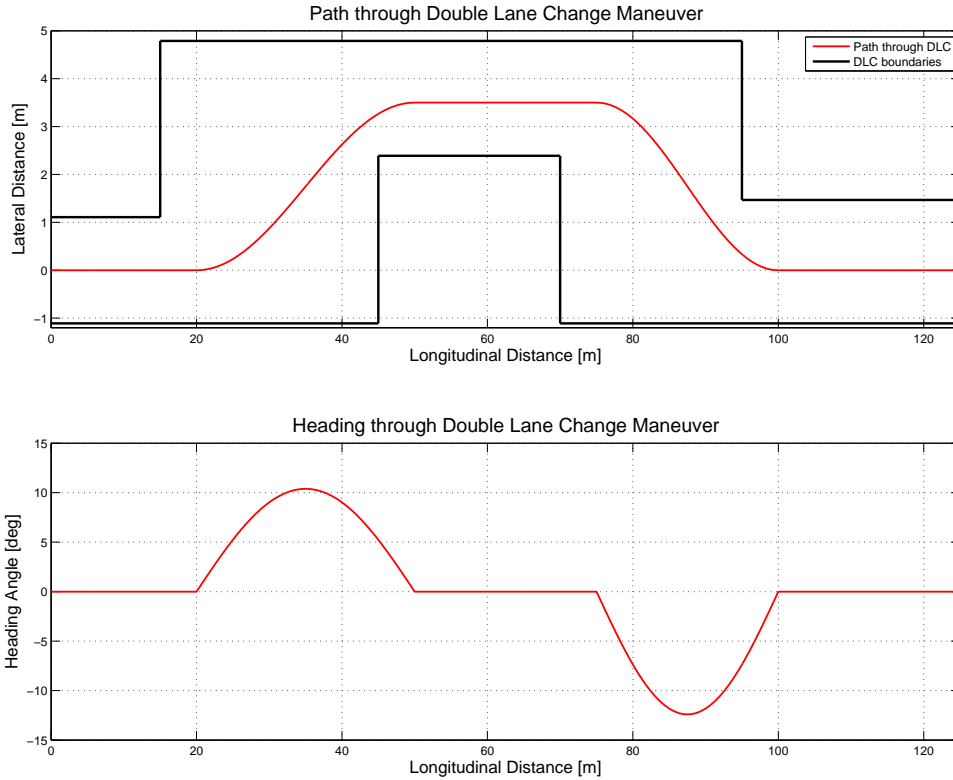
Figure 3.11: Path and heading through double lane change (Genta, 1997).

The lateral acceleration experienced through the DLC can be determined as:

$$\ddot{y} = \frac{V^2}{R},\tag{3.10}$$

where V is the vehicle speed and R is the radius of curvature. The radius of curvature can be determined from the x and y coordinates from:

$$R = \frac{\left(1 + y'^2\right)^{\frac{3}{2}}}{|y''|}\tag{3.11}$$

$$y' = \frac{dY}{dX}, y'' = \frac{d^2Y}{dX^2}\tag{3.12}$$

The theoretical lateral acceleration through the DLC with various vehicle speeds can be seen in Figure 3.12.

If it is taken that the maximum lateral acceleration the vehicle can experience is 8.2m/s^2, then it is evident that perfect path following can only be obtained at a vehicle speed of just over 60km/h. At speeds higher than this the vehicle will be unable to follow the path perfectly

and will deviate from the desired path. The areas with the smallest radii of curvature will be the areas where the vehicle will firstly fail to follow perfectly thus namely the start and end of each lane change.
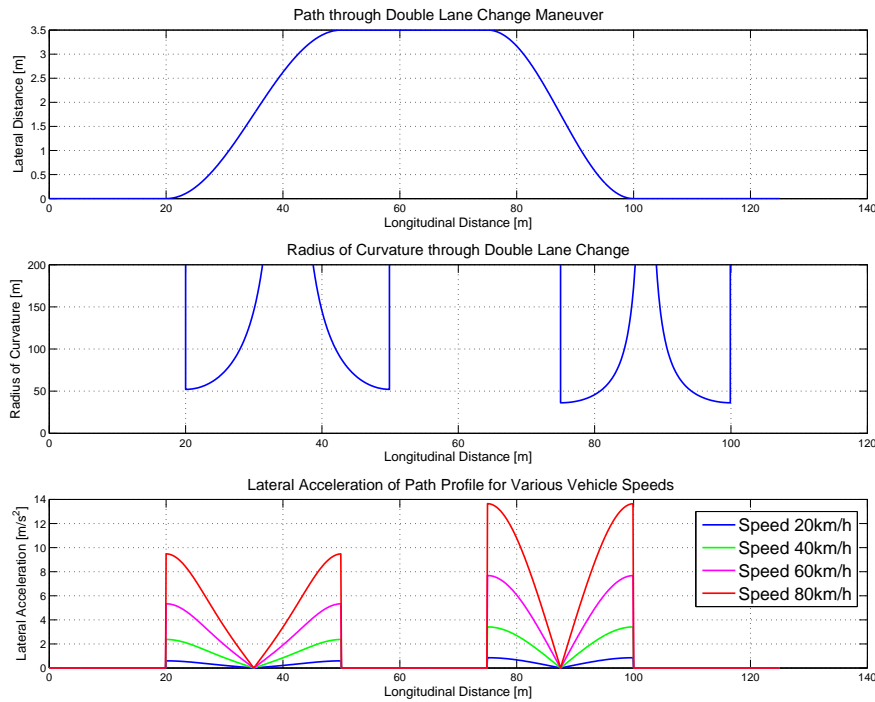
Figure 3.12: Path and heading through double lane change.

Low Speed Path Following Through DLC

A low speed of 40km/h has been chosen as it represents a speed where the dynamics of the vehicle and tyre border between linear and non-linear. This speed thus tests the slow speed accuracy of the driver model in the transitional region between linear and non-linear tyre dynamics.

Figure 3.13 shows the simulation results in terms of vehicle path, lateral acceleration and Centre of Gravity (CG) cross-track error. A maximum cross-track error slightly higher than 0.1m is obtained. The error occurs at 75m which is the region where the vehicle starts moving back into its original lane. From the study above it was anticipated that the largest cross-track error occurs within this region. The cross-track error is still less than half the width of the tyre. The controller thus performs exceptionally well at this speed. A lateral acceleration of 3m/s^2 is achieved, which can still be considered to be within the linear region.
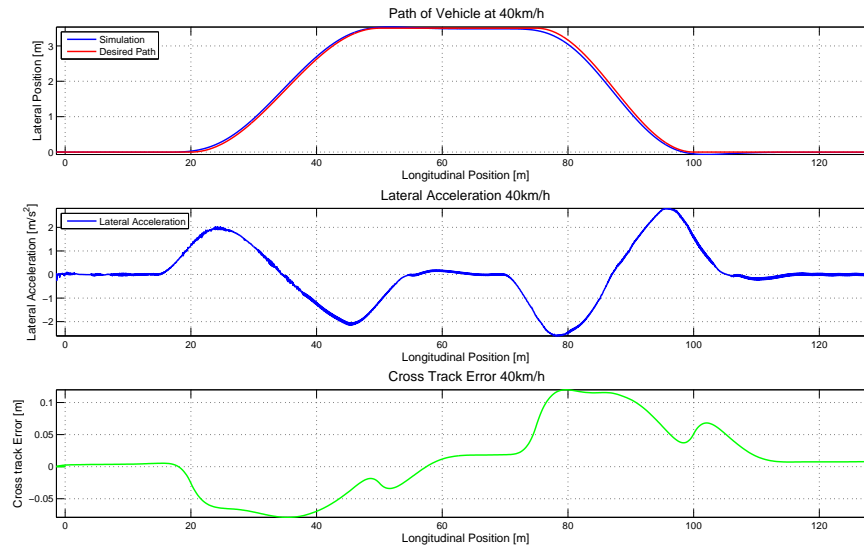
Figure 3.13: Simulation of driver model through DLC at 40km/h.

High Speed Path Following Through DLC

A speed of 70km/h was chosen to present a high speed through the DLC manoeuvre. At this speed the response of the vehicle is very non-linear. Lateral acceleration in the region of 6m/s^2 is to be expected which is well into the non-linear region of the tyre. Figure 3.14 shows the simulation results.
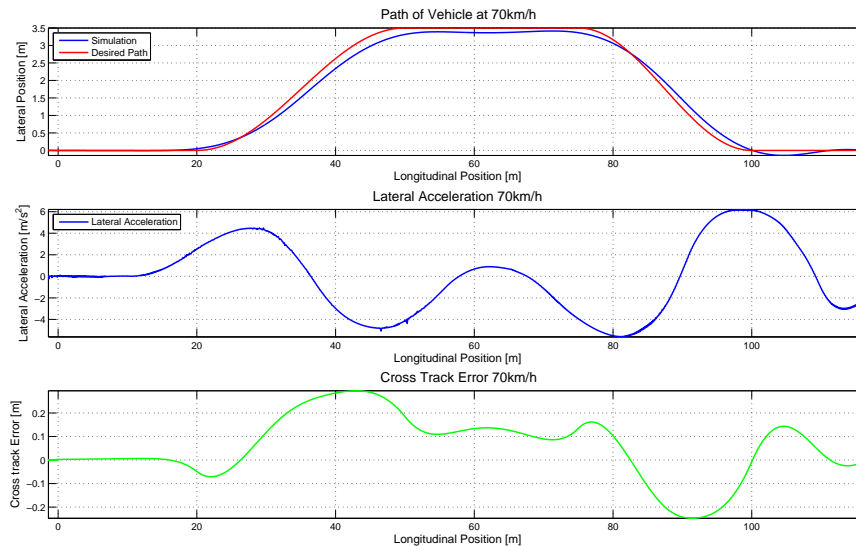
Figure 3.14: Simulation of driver model through DLC at 70km/h.

The maximum cross-track error is found to be under 0.3m - about the same as the tyre's width. The largest errors are again found to be at the end of each lane change. It is concluded that perfect path following at 70km/h was impossible for this specific path. The lateral acceleration plot indicates that the acceleration achieved is consistently between 4-6m/s^2, well into the non-linear tyre regime. The vehicle path is stable with almost no oscillatory behaviour.

The simulation results indicate that the driver model provides accurate path following at low speeds while maintaining stability and accuracy at higher speeds and higher lateral accelerations.

3.5.2 Sinusoidal Path With Increasing Frequency

This path is used to determine at what lateral acceleration the performance of the controller becomes unsatisfactory. This path thus tests the performance of the controller at low lateral acceleration where the tyre characteristics are fairly linear, as well as at higher accelerations near the saturation limit of the tyres in the non-linear regime. This test is performed at speeds of 60km/h and 120km/h. These speeds represent the urban and high-way speed limits of South Africa respectively.

The path to be followed at 60km/h is depicted in Figure 3.15 and shows that around 420m the lateral acceleration will exceed the limits of the vehicle. Figure 3.16 shows the path for the 120km/h test and shows that around 1000m the lateral acceleration will exceed the vehicle limits.
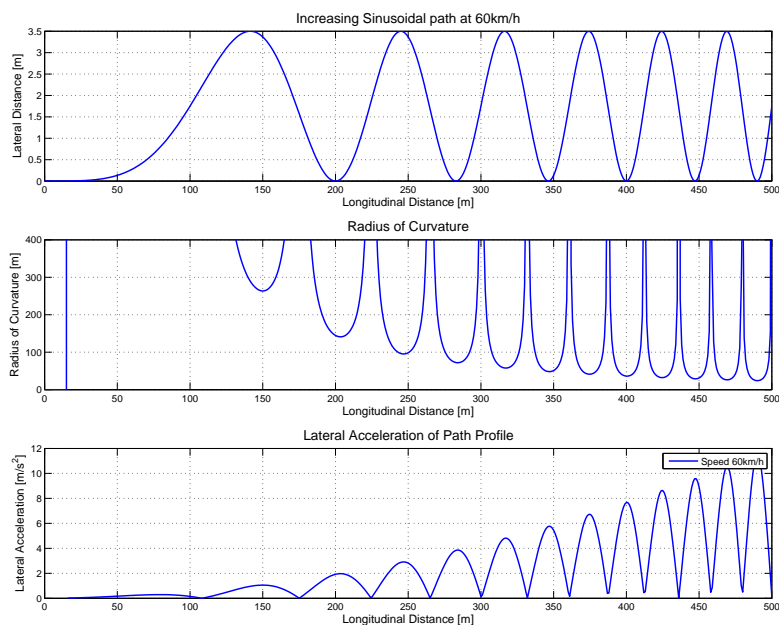
Figure 3.15: Sinusoidal path with increasing frequency for 60km/h.
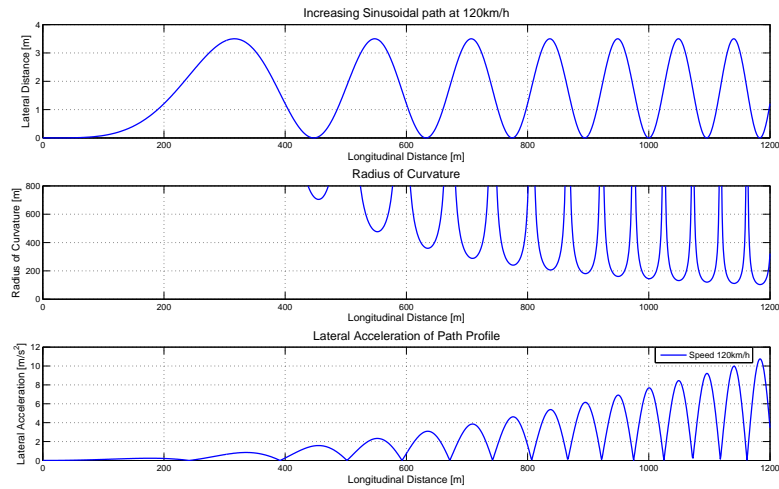
Figure 3.16: Sinusoidal path with increasing frequency for 120km/h.

Simulation of Sinusoidal Path With Increasing Frequency at 60km/h

The simulation results depicted in Figure 3.17 indicate that the vehicle remains stable as the lateral accelerations increase. The vehicle only becomes unstable after the lateral acceleration reaches the maximum the vehicle is capable of developing - around $8.2\text{m}/s^2$. The cross-track error increases slightly but seldom exceeds 0.4m. The simulation concludes that the vehicle remains stable at moderate speed as the lateral acceleration increases while still providing fairly accurate path following. This indicates that the non-linearity of the dynamics is captured well by modeling the vehicle response using the Magic Formula.

Simulation of Sinusoidal Path With Increasing Frequency at 120km/h

Figure 3.18 shows that the vehicle remains stable at a much higher speed. A possible reason explaining why perfect path following is not obtained is most likely due to the fact that the modelled vehicle response is only explicitly performed with data up to speeds of 90km/h. Thus, The Magic Formula is expected to extrapolate the vehicle response up to 120km/h. It is expected that better performance can be obtained if the vehicle response is explicitly modelled up to 120km/h. The jagged plot of the lateral acceleration in Figure 3.18 is also most likely due to the incorrect modeling at 120km/h. The controller overshoots and oscillates slightly causing the small oscillations. The cross-track errors are still not excessively large, and the test concludes that the vehicle not only remains stable at high-way speeds but also at lateral accelerations, which far exceed what normal vehicles experience at these speeds.
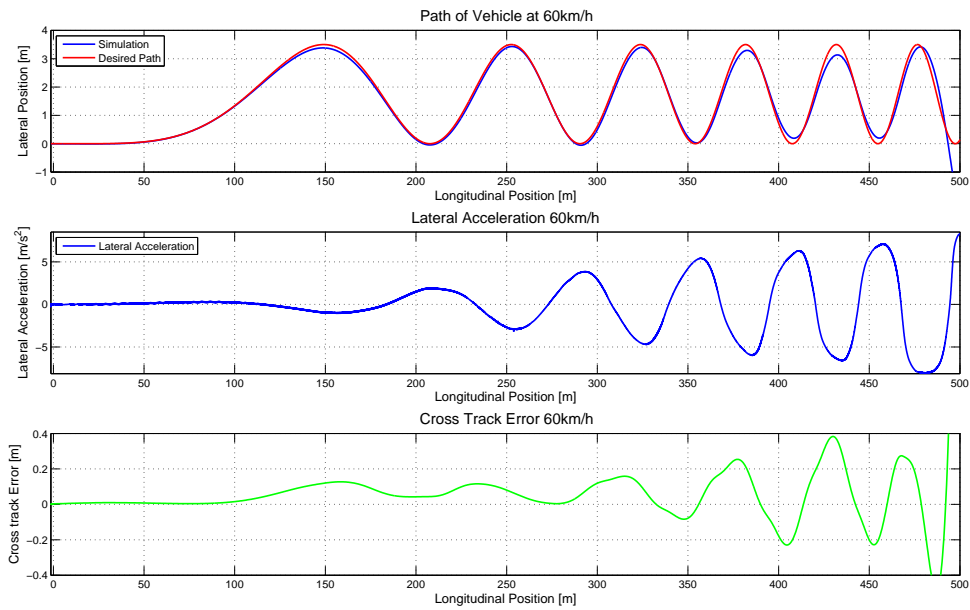
Figure 3.17: Simulation of sinusoidal path with increasing frequency at 60km/h.
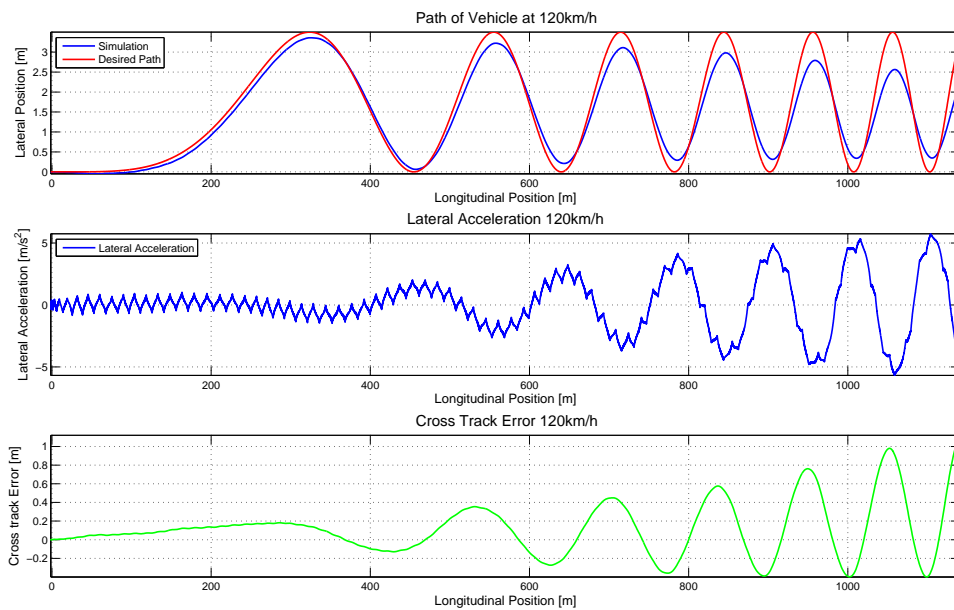
Figure 3.18: Simulation of sinusoidal path with increasing frequency at 120km/h.

Effect of Input Frequency

Another sinusoidal path with increasing frequency will be used to test the driver model to various steering input frequencies. It differs from the previous path in the sense that a

few discrete frequencies are selected as can be seen in Figure 3.19. The path is then made up of four cycles from each frequency. The amplitude at each frequency is changed such that the maximum lateral acceleration experienced in each section is the same. This test thus eliminates the increase of lateral acceleration experienced by the previous path and concentrates on the input frequency. The test is only performed at 60km/h.
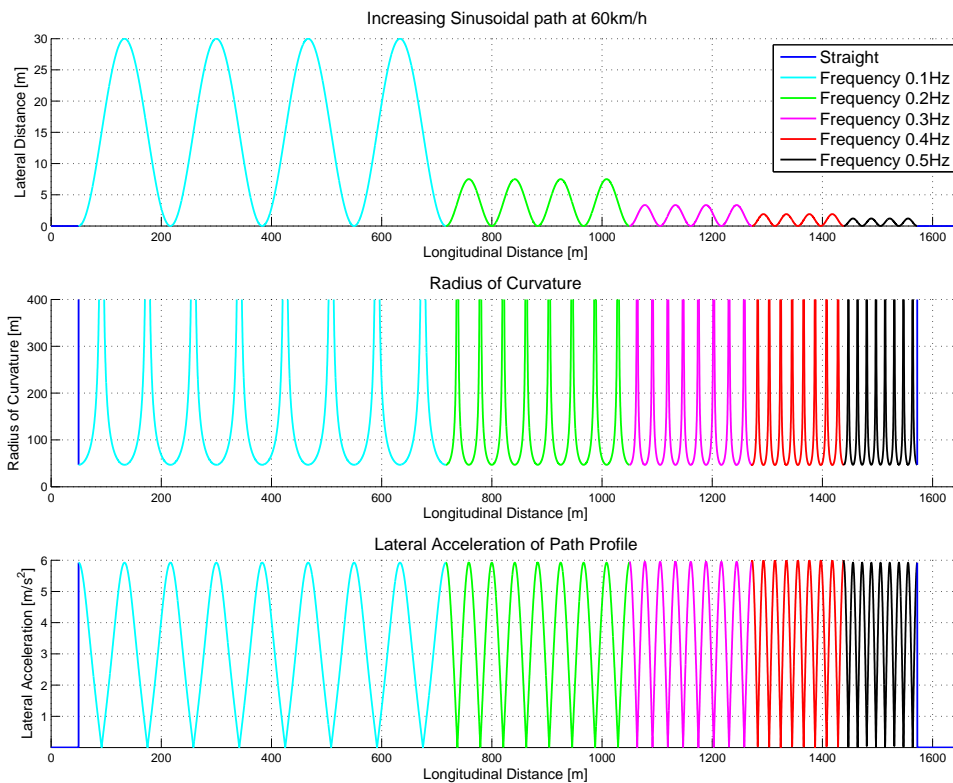
Figure 3.19: Discrete sinusoidal frequencies path.

The vehicle remains stable and provides excellent path following at all frequencies (Figure 3.20) even though the lateral accelerations experienced are consistently over 5m/s^2. This again shows that the controller, which is based on a steady state response, is not affected when the input frequency increases.
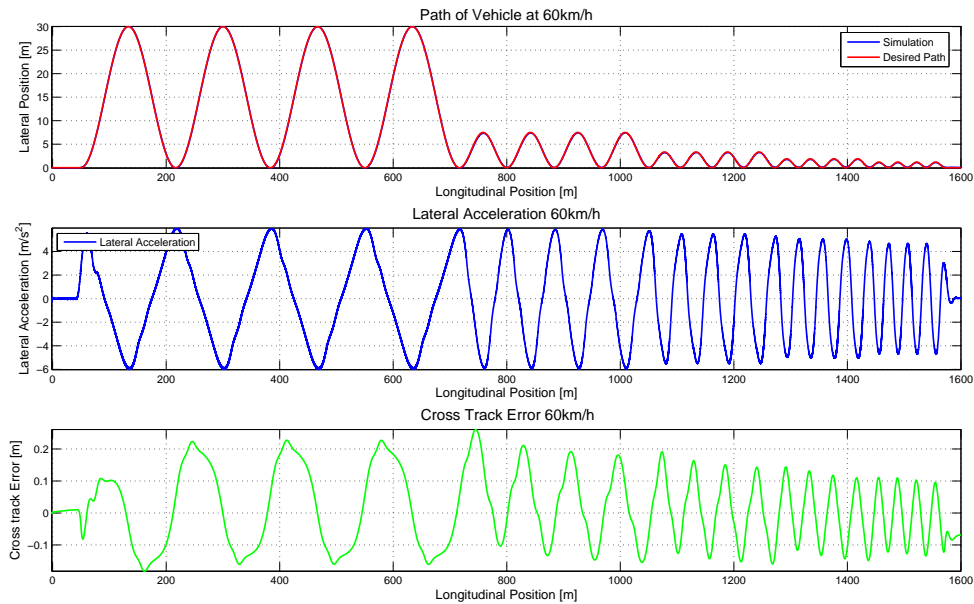
Figure 3.20: Discrete sinusoidal frequencies path following at 60km/h.

3.5.3 Constant Radii S-Curve

In the previous tests the radii of curvature of the paths were always changing representing corners that get progressively tighter as well as corners that open up. These corners are seldom found on normal roads as corners are generally designed for safety reasons to have a constant radii. This test will therefore simulate a normal road by combining two constant radii turns turning in opposite directions, commonly referred to as s-curves. An s-curve is used as opposed to a single turn to make the test more challenging as the vehicle will have to roll from the one side to the other as it changes over from a left hand turn to a right hand turn. This excites the roll of the vehicle and changes the load transfer throughout the change over, thus changing the handling of the vehicle throughout the manoeuvre.

The radii of the turns will be selected to be less than half the recommended radii of rural road designs (Anonymous, 1978) to induce higher lateral accelerations. The radii of curvature selected will produce lateral acceleration in the region of $6m/s^2$. This is in the non-linear tyre region. These lateral accelerations are typically only experienced at 60km/h when a vehicle is driven fast by a normal driver such as racing around a track (Reymond et al, 2001). At 120km/h these lateral accelerations are not even achieved by a normal driver driving fast around a racing track. The lateral accelerations achieved at 120km/h during fast driving were normally below $4m/s^2$.

Constant Radii S-Curve at 60km/h

The results at 60km/h are depicted in Figure 3.21 and shows that the vehicle follows the path fairly well with a maximum cross-track error of just over 0.3m. The maximum cross-track error occurs after the transition period indicating that the transient response at cross-over from one extreme to the other is the causing factor. The cross-track error is still minimised as soon as the vehicle response stabilises and the maximum cross-track error is still fairly small.
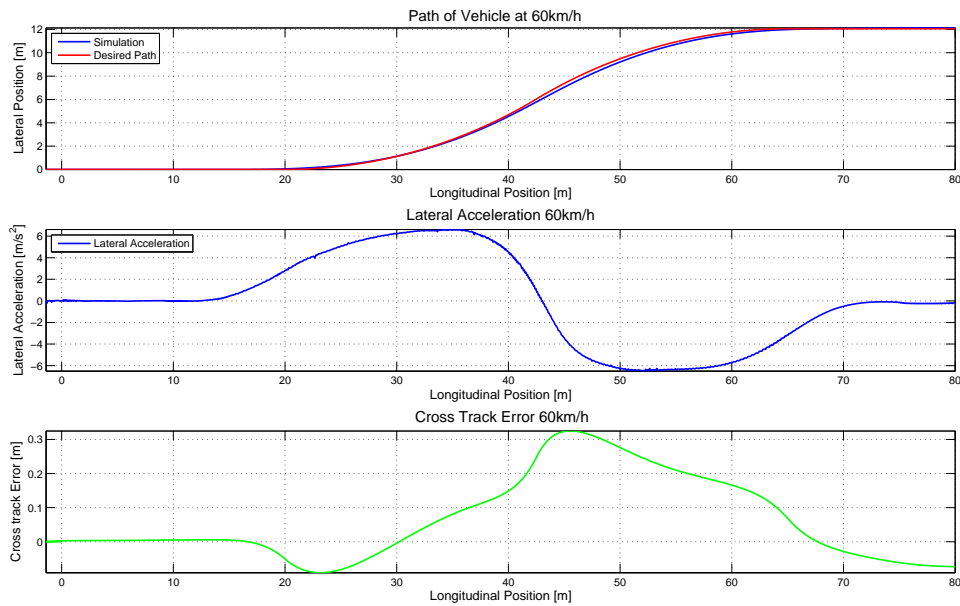
Figure 3.21: Simulation results of S-curve path at 60km/h.

Constant Radii S-Curve at 120km/h

Figure 3.22 shows the simulation results at 120km/h. From this it can be noted that a fairly large cross-track error of close to 1.8m is obtained. This is the same as the vehicle width. However, the vehicle remained stable at this speed performing a manoeuvre which is more difficult than any manoeuvre a normal driver will perform on a normal road. Better results could be expected if the manoeuvre was performed at the minimum radii, as well as explicitly modeling the vehicle up to speeds of 120km/h.
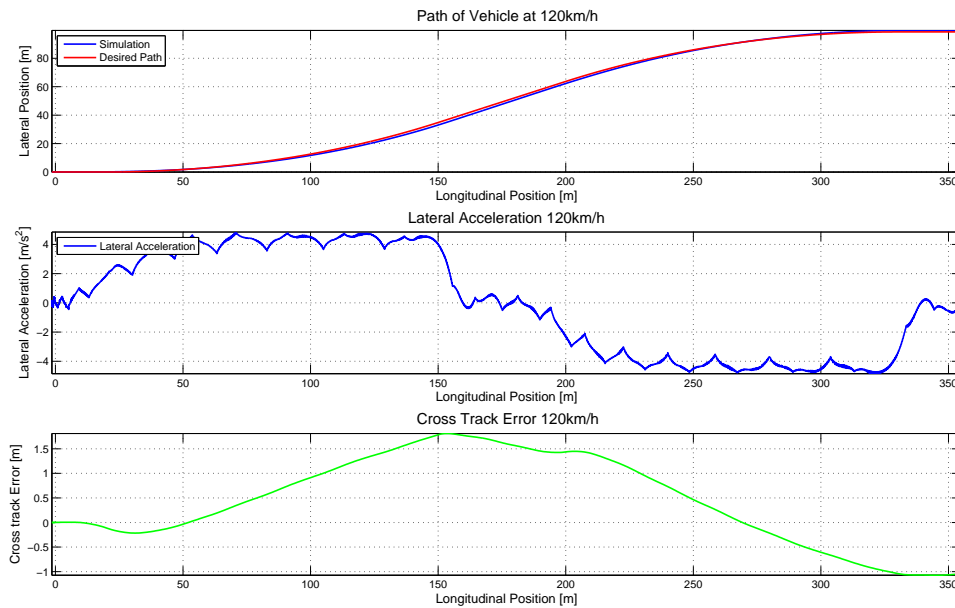
Figure 3.22: Simulation results of S-curve path at 120km/h.

3.6   Conclusion

The modeling of the steady state yaw acceleration response using the Magic Formula enabled the design of a driver model which can operate at higher speeds and lateral acceleration than similar single point preview driver models. This is due to the non-linear vehicle and tyre response which is captured by the Magic Formula. The modifications made, to the original controller developed by Thorreson (2007) not only improved the performance, but also improved its computational efficiency.

The controller, while including the vehicle and tyre dynamics as a whole, does not explicitly include the tyre dynamics. This however does not affect the performance of the controller at high speeds or high lateral accelerations. The controller was found to provide excellent performance at low speeds, as well as provide stable and fairly accurate path following at highway speeds. The higher lateral accelerations did not seem to effect the stability of the controller, but did effect the performance slightly.

The controller is derived from simulations performed on a complicated full vehicle model. Thus, the development of such a controller requires the accurate modelling of a vehicle to some degree. The following chapter will look at a more mathematical approach to a driver model as well as whether a much simpler vehicle model can be used in developing the Inverse Magic Formula Model instead of a full vehicle model.

Chapter 4

Mathematical Models of Yaw Acceleration Response

This chapter covers the development of two vehicle models. The first is a non-linear model incorporating the Magic Formula. This model is evaluated to determine its effectiveness in the construction of the Inverse Magic Formula Model. The second model is derived from the linearisation of the vehicle equations of motion. This is to understand the effect vehicle parameters have on the steady state yaw acceleration response to a constant steer rate. This model is also used to obtain a transfer function of yaw acceleration vs. steer rate. The linear model is modified to include a form of sliding mode control to incorporate the effect of load transfer and lateral tyre force generation on the yaw acceleration response at higher lateral accelerations. Thus, creating a non-linear mathematical model which can be used for control purposes (this is termed the Mathematical Model (MM)).

With slight modification the analysis of the yaw rate response to steer angle input, as presented by Abe (2009), can be used to determine the yaw acceleration response to a steer rate input. The coordinate system used in the analysis is presented first, which is then followed by the derivation of the mathematical models.

4.1 Motion of Fixed Coordinate System on Vehicle

The coordinate system used throughout this study is vehicle fixed. This coordinate system rotates with the vehicle and simplifies the analysis since the motion constraints are unchangeable. Treating the vehicle as a point moving in a plane, the velocity vector $\dot{\mathbf{R}}$ can be presented as:

$$\dot{\mathbf{R}} = u\mathbf{i} + v\mathbf{j}, \tag{4.1}$$

where u and v are the velocity components in the x and y directions. The acceleration vector $\ddot{\mathbf{R}}$ can be obtained by differentiating (4.1) to obtain:

$$\ddot{\mathbf{R}} = \dot{u}\mathbf{i} + u\dot{\mathbf{i}} + \dot{v}\mathbf{j} + v\dot{\mathbf{j}}, \tag{4.2}$$

where the change in unit vector can be obtained as (Abe, 2009):

$$\dot{\mathbf{i}} = r\mathbf{j} \tag{4.3}$$
$$\dot{\mathbf{j}} = -r\mathbf{i} \tag{4.4}$$

where r is the yaw rate. The acceleration vector can thus be written as:

$$\ddot{\mathbf{R}} = (\dot{u} - vr)\mathbf{i} + (\dot{v} + ur)\mathbf{j} \tag{4.5}$$

Assuming point P has a speed V with a angle β from the x-axis (Figure 4.1) equation (4.5) can be rewritten as:

$$\ddot{\mathbf{R}} = (-V\sin\beta\dot{\beta} - V\sin\beta r)\mathbf{i} + (V\cos\beta\dot{\beta} + V\cos\beta r)\mathbf{j} \tag{4.6}$$

Assuming small angles, therefore $\sin\beta \approx \beta$ and $\cos\beta \approx 1$, thus the final acceleration vector $\ddot{\mathbf{R}}$ is obtained as:

$$\ddot{\mathbf{R}} = -V\beta(\dot{\beta} + r)\mathbf{i} + V(\dot{\beta} + r)\mathbf{j} \tag{4.7}$$
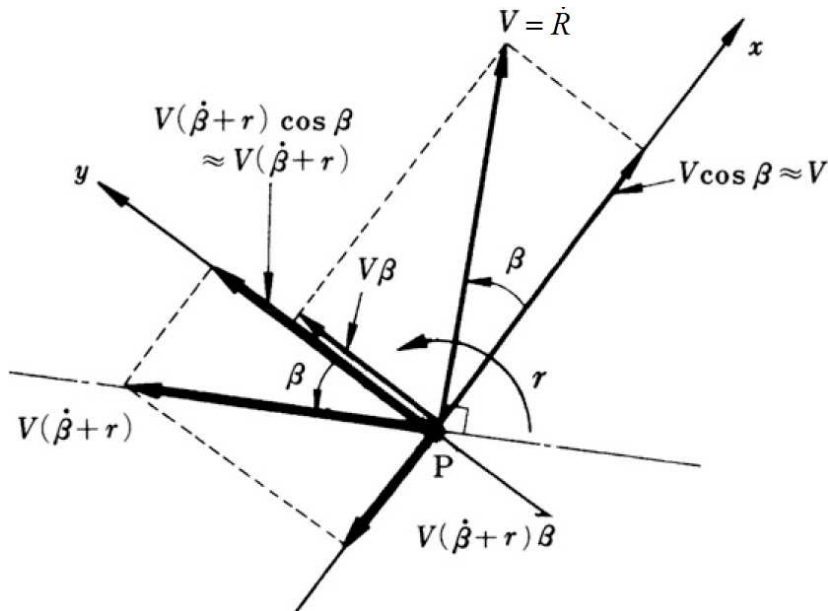
Figure 4.1: Acceleration and velocity of a point in planar motion. (Abe, 2009:51)

4.2 Derivation of Mathematical Models

The steering of the vehicle is dependant on the forces generated at each wheel, with the driver capable of directly altering the front wheel (normal vehicle without rear steering). As mentioned in section 1.2 the tyre forces F_{f1}, F_{f2}, F_{r1}, F_{r2} are dependant on the respective side-slip angle β_{f1}, β_{f2}, β_{r1}, β_{r2}. The side-slip angles are defined as the angle between the tyre's heading angle and travelling direction. Neglecting second order terms of $|\beta|$, $|l_f r/V|$, $|l_f r/V|$, $|d_f r/2V|$, $|d_r r/2V| \ll 1$, the side-slip angles are obtained from Figure 4.2 as (Abe, 2009):

$$\beta_{f1} \approx \frac{V\beta + l_f r}{V - d_f r/2} - \delta \tag{4.8}$$

$$\beta_{f2} \approx \frac{V\beta + l_f r}{V + d_f r/2} - \delta \tag{4.9}$$

$$\beta_{r1} \approx \frac{V\beta + l_r r}{V - d_r r/2} \tag{4.10}$$

$$\beta_{r2} \approx \frac{V\beta + l_r r}{V + d_r r/2} \tag{4.11}$$

The lateral forces generated by the tyres causes a planar lateral motion of the vehicle which can be described as:

$$m\ddot{y} = mV(\dot{\beta} + r) \quad = \quad F_{f1} + F_{f2} + F_{r1} + F_{r2} \tag{4.12}$$

$$\tag{4.13}$$

The lateral forces also result in a yaw moment about the vehicle's centre of gravity, which causes a yaw motion which can be described by:

$$I\dot{r} \quad = \quad l_f(F_{f1} + F_{f2}) - l_r(F_{r1} + F_{r2}) \tag{4.14}$$

In the case of the non-linear model the tyre forces can be modelled using the Magic Tyre Formula presented in section 3.2, represented here for convenience.

$$y(x) \quad = \quad D\sin(C\arctan\{Bx - E(Bx - \arctan(Bx))\}) \tag{4.15}$$

$$Y(X) \quad = \quad y(x) + S_v \tag{4.16}$$

$$x \quad = \quad X + S_h \tag{4.17}$$

where Y is the lateral force and X is the tyre side-slip angle, and the other parameters are tyre vertical load dependent. If load transfer is not taken into consideration, the vertical tyre load is taken as the static tyre load determined by the CG position and overall vehicle mass. However, load transfer will be considered later as presented in section 4.5.1. This non-linear model is used in section 4.6.1 to determine whether it is sufficient in reproducing the Inverse Magic Formula Model. Use of this model could make the construction of the Inverse Magic Formula Model much faster in terms of development and simulation time.
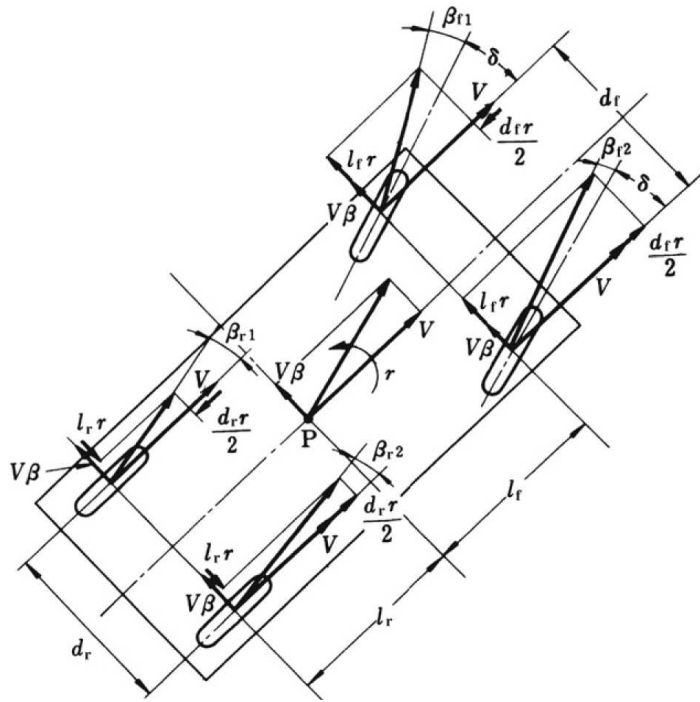
Figure 4.2: Side-slip angles of each tyre (Abe, 2009:52)

4.2.1 Linear Model used for Sliding Mode

This model is similar to the non-linear model described in section 4.2 in its approach, but linearises all equations in order to obtain a transfer function which can be used for control purposes. The side-slip angles are linearised as:

$$\beta_{f1} \approx \frac{V\beta + l_f r}{V - d_f r/2} - \delta \approx \beta + \frac{l_f r}{V} - \delta \tag{4.18}$$

$$\beta_{f2} \approx \frac{V\beta + l_f r}{V + d_f r/2} - \delta \approx \beta + \frac{l_f r}{V} - \delta \tag{4.19}$$

$$\beta_{r1} \approx \frac{V\beta + l_r r}{V - d_r r/2} \approx \beta + \frac{l_r r}{V} \tag{4.20}$$

$$\beta_{r2} \approx \frac{V\beta + l_r r}{V + d_r r/2} \approx \beta + \frac{l_r r}{V} \tag{4.21}$$

Thus, the left and the right side-slip angles can be assumed equal on each axle:

$$\beta_f = \beta_{f1} = \beta_{f2} = \beta + \frac{l_f r}{V} - \delta \tag{4.22}$$

$$\beta_r = \beta_{r1} = \beta_{r2} = \beta + \frac{l_r r}{V} \tag{4.23}$$

The equations of motion presented in (4.12) and (4.14) are linearised such that the tyre lateral force is linearly dependent on the side-slip angle.

From section 1.2 it is known that this assumption is valid for small side-slip angles. The planar lateral motion becomes:

$$m\ddot{y} = mV(\dot{\beta} + r) \quad = \quad F_{f1} + F_{f2} + F_{r1} + F_{r2} \tag{4.24}$$

$$= \quad -C_{f1}\beta_{f1} - C_{f2}\beta_{f2} - C_{r1}\beta_{r1} - C_{r2}\beta_{r2} \tag{4.25}$$

$$= \quad -2C_f\beta_f - 2C_r\beta_r \tag{4.26}$$

The yaw motion becomes:

$$I\dot{r} \quad = \quad l_f(F_{f1} + F_{f2}) - l_r(F_{r1} + F_{r2}) \tag{4.27}$$

$$= \quad l_f(-C_{f1}\beta_{f1} - C_{f2}\beta_{f2}) - l_r(-C_{r1}\beta_{r1} - C_{r2}\beta_{r2}) \tag{4.28}$$

$$= \quad -2l_f C_f\beta_f + 2l_r C_r\beta_r \tag{4.29}$$

C is the cornering stiffness of the respective tyre. In (4.26) and (4.29) the assumption that the cornering stiffness of the left and right tyres are the same for each axle is made i.e. $C_{f1} = C_{f2}$ and $C_{r1} = C_{r2}$. In section 4.5 the mathematical model introduces sliding mode to compensate for the non-linear tyre.

Substituting the side-slip angles obtained in (4.22) and (4.23) into (4.26) and (4.29) results in the vehicle's equations of motions to be in terms of the steering angle δ:

$$mV(\dot{\beta} + r) \quad = \quad -2C_f\left(\beta + \frac{l_f r}{V} - \delta\right) - 2C_r\left(\beta + \frac{l_r r}{V}\right) \tag{4.30}$$

$$I\dot{r} \quad = \quad -2l_f C_f\left(\beta + \frac{l_f r}{V} - \delta\right) + 2l_r C_r\left(\beta + \frac{l_r r}{V}\right) \tag{4.31}$$

Rearranging (4.30) and (4.31):

$$mV\dot{\beta} + 2(C_f + C_r)\beta + \left[mV + \frac{2(l_f C_f - l_r C_r)}{V}\right]r \quad = \quad 2C_f\delta \tag{4.32}$$

$$2(l_f C_f - l_r C_r)\beta + I\dot{r} + \frac{2(l_f^2 C_f + l_r^2 C_r)}{V}r \quad = \quad 2l_f C_f\delta \tag{4.33}$$

Making use of the Laplace-transform to obtain the Laplace operators $\dot{\beta}(s)$, $\dot{r}(s)$ and $\dot{\delta}(s)$ for $\dot{\beta}$, $\dot{r}$ and $\dot{\delta}$ on (4.32) and (4.33):

$$\dot{\beta}(s)\left(mV + \frac{2(C_f + C_r)}{s}\right) + \left[mV + \frac{2(l_f C_f - l_r C_r)}{V}\right]\frac{\dot{r}(s)}{s} \quad = \quad 2C_f\frac{\dot{\delta}(s)}{s}$$

$$\tag{4.34}$$

$$2(l_f C_f - l_r C_r)\frac{\dot{\beta}(s)}{s} + \dot{r}(s)\left(I + \frac{2(l_f^2 C_f + l_r^2 C_r)}{Vs}\right) \quad = \quad 2l_f C_f\frac{\dot{\delta}(s)}{s}a$$

$$\tag{4.35}$$

$$\begin{bmatrix} mVs + 2(C_f + C_r) & mV + \frac{2(l_f C_f - l_r C_r)}{V} \\ 2(l_f C_f - l_r C_r) & Is + 2(l_f^2 C_f + l_r^2 C_r) \end{bmatrix}\begin{bmatrix} \dot{\beta}(s) \\ \dot{r}(s) \end{bmatrix} = \begin{bmatrix} 2C_f\dot{\delta}(s) \\ 2l_f C_f\dot{\delta}(s) \end{bmatrix} \tag{4.36}$$

The transfer functions of $\frac{\dot{\beta}(s)}{\delta(s)}$ and $\frac{\dot{r}(s)}{\delta(s)}$ can be obtained as:

$$\frac{\dot{\beta}(s)}{\dot{\delta}(s)} = \frac{\begin{vmatrix} 2C_f & mV + \frac{2(l_fC_f-l_rC_r)}{V} \\ l_fC_f & Is + \frac{2(l_f^2C_f+l_r^2C_r)}{V} \end{vmatrix}}{\begin{vmatrix} mVs + 2(C_f+C_r) & mV + \frac{2(l_fC_f-l_rC_r)}{V} \\ 2(l_fC_f - l_rC_r) & \frac{2(l_f^2C_f+l_r^2C_r)}{V} \end{vmatrix}} \tag{4.37}$$

$$\frac{\dot{r}(s)}{\dot{\delta}(s)} = \frac{\begin{vmatrix} mVs + 2(C_f+C_r) & 2C_f \\ 2(l_fC_f - l_rC_r) & l_fC_f \end{vmatrix}}{\begin{vmatrix} mVs + 2(C_f+C_r) & mV + \frac{2(l_fC_f-l_rC_r)}{V} \\ 2(l_fC_f - l_rC_r) & \frac{2(l_f^2C_f+l_r^2C_r)}{V} \end{vmatrix}} \tag{4.38}$$

Equations (4.37) and (4.38) are complex to analyse and will be simplified before studying the effect vehicle parameters have on the response of the vehicle.

A simpler way of analysing the vehicle response is to study the characteristic equation of the vehicle motion, obtained as:

$$\begin{vmatrix} mVs + 2(C_f+C_r) & mV + \frac{2(l_fC_f-l_rC_r)}{V} \\ 2(l_fC_f - l_rC_r) & Is + 2(l_f^2C_f + l_r^2C_r) \end{vmatrix} = 0 \tag{4.39}$$

$$mIV\left[s^2 + \frac{2m(l_f^2C_f + l_r^2C_r) + 2I(C_f+C_r)}{mIV}s + \frac{4C_fC_r(l_f^2 + l_r^2)}{mIV^2} - \frac{2(l_fC_f - l_rC_r)}{I}\right]$$
$$= 0 \tag{4.40}$$

simplify to:

$$s^2 + 2Ds + P^2 = 0 \tag{4.41}$$
$$s^2 + 2\zeta\omega_n s + \omega_n^2 = 0 \tag{4.42}$$

where

$$2D = \frac{2m(l_f^2C_f + l_r^2C_r) + 2I(C_f+C_r)}{mIV} \tag{4.43}$$
$$P^2 = \frac{4C_fC_r(l_f^2 + l_r^2)}{mIV^2} - \frac{2(l_fC_f - l_rC_r)}{I} \tag{4.44}$$

The transient response of the vehicle can be studied by studying the roots of the characteristic equation:

$$\lambda_{1,2} = -D \pm \sqrt{D^2 - P^2} \tag{4.45}$$

It is evident from (4.43) that $D > 0$, thus the transient response can be classified into categories based on D and P:

1. $D^2 - P^2 \geq 0, P^2 > 0$ then $\lambda_{1,2}$ are negative integers, the motion thus converges without oscillation.

2. $D^2 - P^2 < 0$ then $\lambda_{1,2}$ are complex numbers with negative real parts, the motion thus converges but with an oscillation.

3. $P^2 \leq 0$ then $\lambda_{1,2}$ are positive and negative integers, the motion thus diverges without oscillation.

Thus, it is clear that cases 1 and 2 result in a stable system while case 3 is unstable. Vehicle designers will aim to develop a vehicle with a transient response of case 1, since even a vehicle in case 2 while stable, will be very hard to control by a normal human driver.

Two parameters used to facilitate the studying of the steering response are the Static Margin (SM) and Stability Factor (SF). These two parameters are defined as:

$$SM = -\frac{l_f C_f - l_r C_r}{l(C_f + C_r)} \tag{4.46}$$

$$SF = \frac{m}{2l} \frac{C_f + C_r}{C_f C_r} SM \tag{4.47}$$

where l is the wheel base $l = l_f + l_r$. The effect of these parameters will be discussed later. The response can also be analysed by studying the natural frequency and damping ratio obtained in (4.42) and computed as:

$$\omega_n = \frac{2l}{V} \sqrt{\frac{C_f C_r}{mI}} \sqrt{1 + SFV^2} \tag{4.48}$$

$$\zeta = \frac{m(l_f^2 C_f + l_r^2 C_r) + I(C_f + C_r)}{2I \sqrt{mIC_f C_r(1 + SFV^2)}} \tag{4.49}$$

Using the parameters in (4.46) and (4.47) as well as the natural frequency and damping ratio, it is possible to obtain a very simplified form of the transfer function presented in (4.37) and (4.38). Since only the yaw acceleration is to be studied, only its transfer function will be presented, which is obtained as:

$$\frac{\dot{r}(s)}{\dot{\delta}(s)} = G\frac{1 + T_r s}{1 + \frac{2\zeta s}{\omega_n} + \frac{s^2}{\omega_n^2}} \tag{4.50}$$

where

$$G = \frac{1}{1 + SFV^2} \frac{V}{l} \tag{4.51}$$

$$T_r = \frac{ml_f V}{2lC_r} \tag{4.52}$$

The response to a step steer rate input can now be calculated as:

$$\dot{r}(s) = G\frac{1 + T_r s}{1 + \frac{2\zeta s}{\omega_n} + \frac{s^2}{\omega_n^2}} \frac{\dot{\delta}}{s} \tag{4.53}$$

where $\frac{\dot{\delta}}{s}$ is the Laplace transform of a step input which represents a constant steer rate input to the vehicle. The steady state yaw acceleration response can be calculated as:

$$\lim_{t\to\infty} \dot{r}(t) = \lim_{s\to 0} s\dot{r}(s) \tag{4.54}$$

$$= \lim_{s\to 0} G\frac{1+T_r s}{1+\frac{2\zeta s}{\omega_n}+\frac{s^2}{\omega_n^2}}\dot{\delta} \tag{4.55}$$

$$= G\dot{\delta} \tag{4.56}$$

Thus, G is also known as the steady state yaw acceleration gain. This relationship can be used for yaw angle control purposes in the same manner as the Inverse Magic Formula Model by using the inverse as:

$$\dot{\delta}_{\psi,MM} = G^{-1}\dot{r} \tag{4.57}$$

While this currently applies to a linear vehicle model with a linear tyre model, it can still be used to estimate the effect of varying certain vehicle parameters. Later a sliding mode will be introduced whereby the non-linearity of the vehicle and tyre will be included.

4.3 Lateral Position Control

The same lateral position controller as proposed in section 3.4 is added to the yaw angle controller of the mathematical model. This controller uses the cross-track error at a preview distance, as well as a gain scheduling scheme to compensate for the longitudinal speed. As mentioned previously, as the speed increases the vehicle steering tends to become more sensitive. This increase in sensitivity is presented by the steady state yaw acceleration gain used in (4.56) and determined in (4.51). This shows that the increase is not only speed dependent, but also depends on the vehicle layout i.e. position of centre of gravity and cornering stiffness of the front and rear tyres. The steady state gain presents an ideal method of introducing the gain scheduling. Thus, the control output becomes:

$$\dot{\delta}_{e_{lat}} = f_{K_p}(V)e_{lat} + f_{K_d}(V)\frac{de_{lat}}{dt} \tag{4.58}$$

$$= \frac{K_p}{G}e_{lat} + \frac{K_d}{G}\frac{de_{lat}}{dt} \tag{4.59}$$

$$\text{where } G = \frac{1}{1+SFV^2}\frac{V}{l} \tag{4.60}$$

where K_p and K_d are the gains constants. A lower limit to G is also given to prevent the steering action approaching infinity.

4.4 Land Rover Defender Response and Sensitivity Analysis

Making use of the linear model, as well as the Land Rover Defender baseline values and tyre characteristics, a sensitivity analysis can be performed. This analysis gives an indication

of how susceptible the vehicle's handling is to a change in parameters such as mass or tyre properties.

The Static Margin (SM) and Stability Factor (SF) which are dependent on the vehicle parameters are normally used to characterise the effect of understeer or oversteer with an increase in vehicle speed. The linear model is also compared to the Inverse Magic Formula Model to demonstrate the limitations of linear models.

4.4.1 Static Margin and Stability Factor

The SM - as obtained in (4.46) - gives an indication of the vehicle's steer characteristic and can be summarised as:

1. $SM > 0$, the vehicle displays Under Steer (US) characteristic.

2. $SM = 0$, the vehicle displays Neutral Steer (NS) characteristic.

3. $SM < 0$, the vehicle displays Over Steer (OS) characteristic.

The stability factor SF which has the same sign as SM is an indication of how the steer characteristic is affected by the vehicle speed. As obtained in equation (4.51) the steady state gain is affected by vehicle speed and the stability factor, as depicted in Figure 4.3.
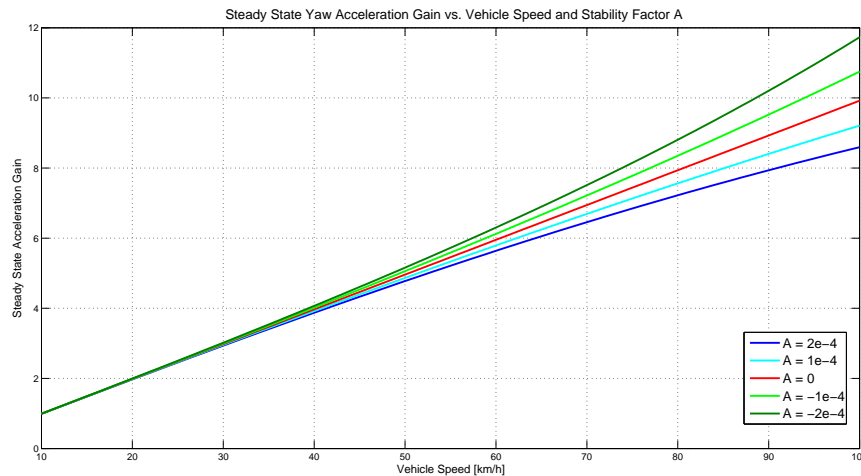
Figure 4.3: Steady state gain vs. vehicle speed and stability factor A.

From Figure 4.3 it can be observed that the steady state gain increases with vehicle speed if $SF < 0$ or $SM < 0$. This is indicative of OS, because at higher speeds a smaller steer rate is needed to obtain a specific yaw acceleration. From equation (4.51) it is observable that the vehicle becomes unstable when $1 + SFV^2 = 0$. Therefore, with OS there exist a certain speed at which the vehicle is unstable this is known as the critical velocity V_c. The critical velocity decreases with larger negative values of SF.

With US ($SM > 0$, thus, $SF > 0$) a higher steer rate is needed to obtain a certain yaw acceleration. While the vehicle remains stable at all speeds, the vehicle can become very difficult to steer at higher speeds.

Land Rover Static Margin and Stability Factor

Using the vehicle parameters (see Appendix A) the static margin and stability factor of the Land Rover Defender can be determined as:

$$SM = 1.4e - 5 \tag{4.61}$$
$$SF = 2.84e - 7 \tag{4.62}$$

Thus, the vehicle has a slight under steer characteristic. The natural frequency ω_n, damping ratio ζ and response time as a function of vehicle speed is plotted in Figure 4.4.
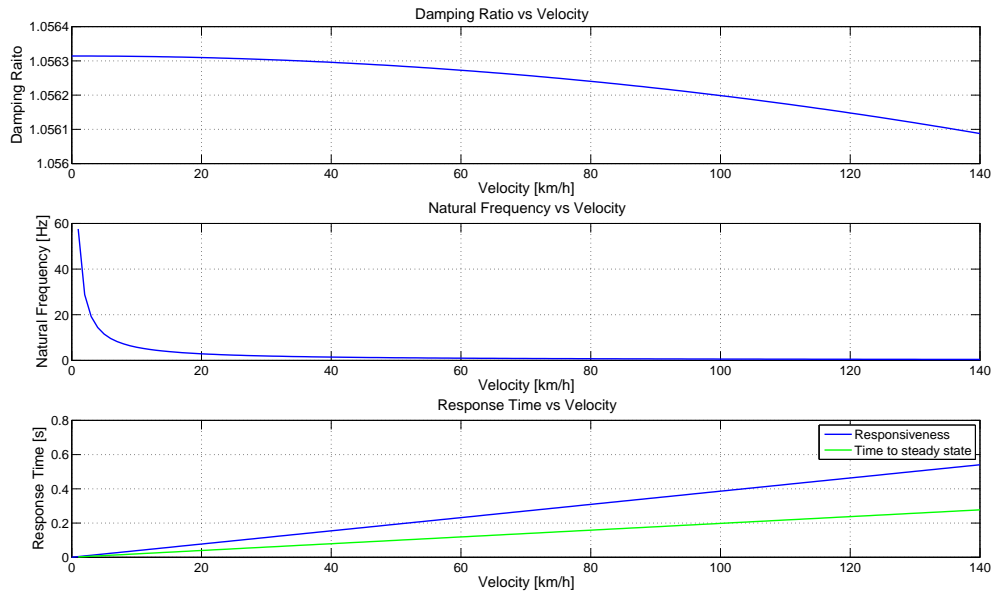
Figure 4.4: Natural frequency ω_n, damping ratio ζ and vehicle steady state response as a function of vehicle speed.

As observed in Figure 4.4 with under steer the damping ratio decreases with vehicle speed. On the other hand, with over steer the damping ratio increases with an increase in vehicle speed. The damping ratio can also be noted to be above unity. Thus, the response is over damped and will not overshoot or oscillate about the steady state response. The natural frequency decreases with an increase in vehicle speed. In the case of under steer, the damping ratio can decrease below unity as the speed increases. The vehicle can therefore becomes sensitive to very rapid steering inputs at higher vehicle speeds.

The response time, as well as time to steady state of the vehicle, is also speed dependent. This would indicate that the transient response, which is excluded by the steady state response driver models, may have a larger effect as the vehicle speed increases. This could pose a problem where sudden steering inputs are required, as in the double lane change. However, if the input slowly ramps up to a maximum, the effect of the transient response will be minimal. Typical everyday steering inputs are more gradual, while the double lane change is more abrupt. Thus, at higher speeds it may become necessary to include a means by which the transient response can be taken into consideration. One such a possibility is to sample the road input with a larger preview time, while still using the smaller preview time in the calculation of the required yaw acceleration. With reference to Figure 3.7:

$$d_{preview} = \dot{x}\tau_1 \text{ (used to get } \psi_d) \tag{4.63}$$

$$\ddot{\psi} = 2\frac{\psi_d - \psi_0 - \dot{\psi}\tau_2}{\tau_2^2} \tag{4.64}$$

$$\text{where } \tau_1 > \tau_2$$

The increase in preview time will force the vehicle to steer sooner with the same intensity, thus allowing more time for the vehicle to obtain a steady state response.

4.4.2 Linear Model Comparison with Inverse Magic Formula Model

Figure 4.5 shows the comparison of the model obtained in (4.56) with the Inverse Magic Formula Model. It can be observed that these two models correlate fairly well at low speeds. This is to be expected since at low speeds the dynamics remain fairly linear. However, as both speed and steer rate increases the correlation deteriorates. The linear model keeps a linear relationship as expected during higher lateral accelerations. The model overestimates the over steer characteristic. At higher speeds the linear model has a higher gain than that of the Inverse Magic Formula Model. The linear model also does not capture the non-linearity, which is present with an increase in steer rate at higher vehicle speeds.

4.4.3 Sensitivity Analysis

A sensitivity analysis is performed to determine which parameters most affect the steady state gain. Parameters such as the mass, location of the centre of gravity, as well as the front and rear lateral tyre stiffness are considered.

Vehicle Mass

The sensitivity of the yaw acceleration to a change in vehicle mass is depicted in Figure 4.6 where the mass was increased and reduced by 20%. From this figure it can be concluded that the vehicle mass has no effect, this is due to the almost neutral steer of the vehicle. The mass of a vehicle is one of the easiest and cheapest parameters of a vehicle to measure. Thus, the uncertainty of this parameter presents little risk to the development of the linear model. It should also be mentioned that the moment of inertia I has no effect on the steady state yaw
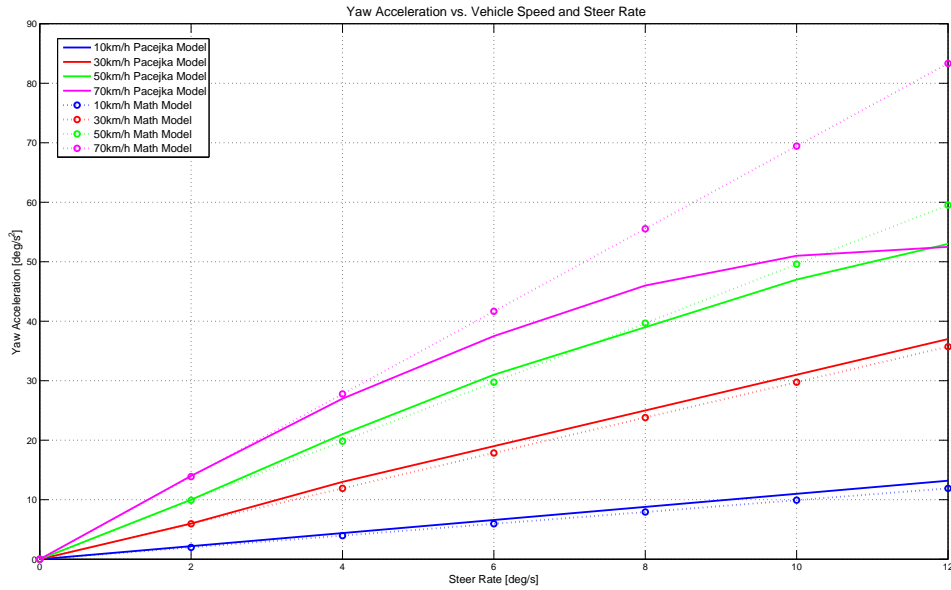
Figure 4.5: Comparison between Inverse Magic Formula Model and Mathematical Model.

acceleration gain, but does however effect the rate of response of the system. With a larger moment of inertia, the vehicle takes longer to reach a steady state and vice versa.
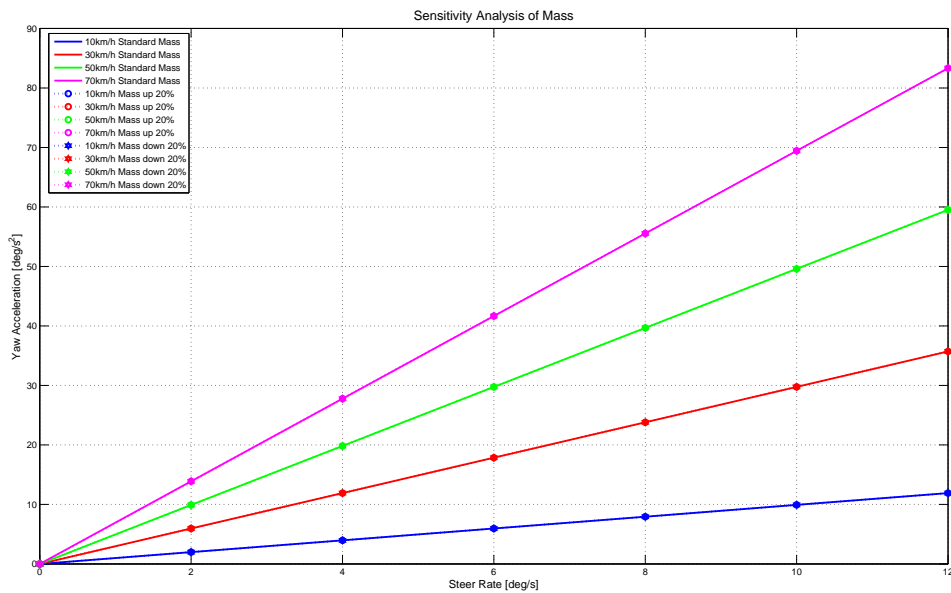
Figure 4.6: Sensitivity analysis of yaw acceleration gain with respect to vehicle mass.

Longitudinal Position of Centre of Gravity

The longitudinal position of the CG effects the distances l_f and l_r. These distances are present in both the static margin and stability factor which govern the steady state gain. Figure 4.7 depicts the sensitivity analysis where the CG was moved 5% ($\pm140mm$) of the total wheelbase forward and backward. From this figure it is clear that the position of the CG has a large effect on the gain and that this effect increases rapidly with an increase in vehicle speed. The CG is fairly easy and inexpensive to determine, but can change considerably depending on how the vehicle is loaded.
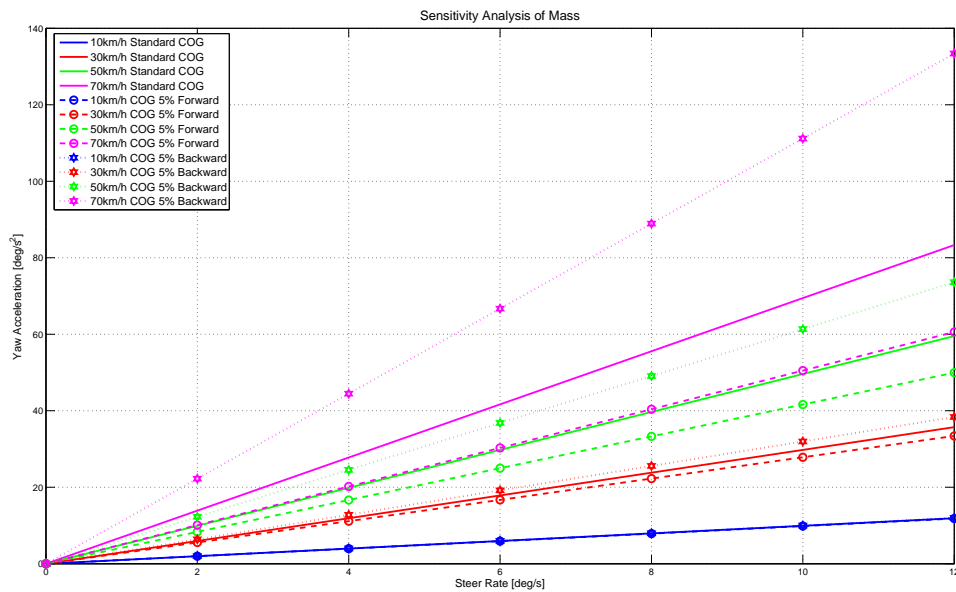
Figure 4.7: Sensitivity analysis of yaw acceleration gain with respect to vehicle longitudinal centre of gravity position.

Front and Rear Tyre Lateral Stiffness

The tyre lateral stiffness is very important since it dictates the amount of force generated at a tyre depending on that tyre's vertical load and side-slip angle. Figure 4.8 depicts the sensitivity of the gain to a 5% increase in front lateral tyre stiffness. It is clear that the effect of this parameter increases with an increase in vehicle speed. It should be noted that with an increased front lateral tyre stiffness, the gain increases as a result of a much larger over steer characteristic.

Figure 4.9 depicts the sensitivity of the gain to a 5% increase in rear lateral tyre stiffness, the effect is similar to that of an increase in front stiffness except that a more under steer characteristic is obtained.
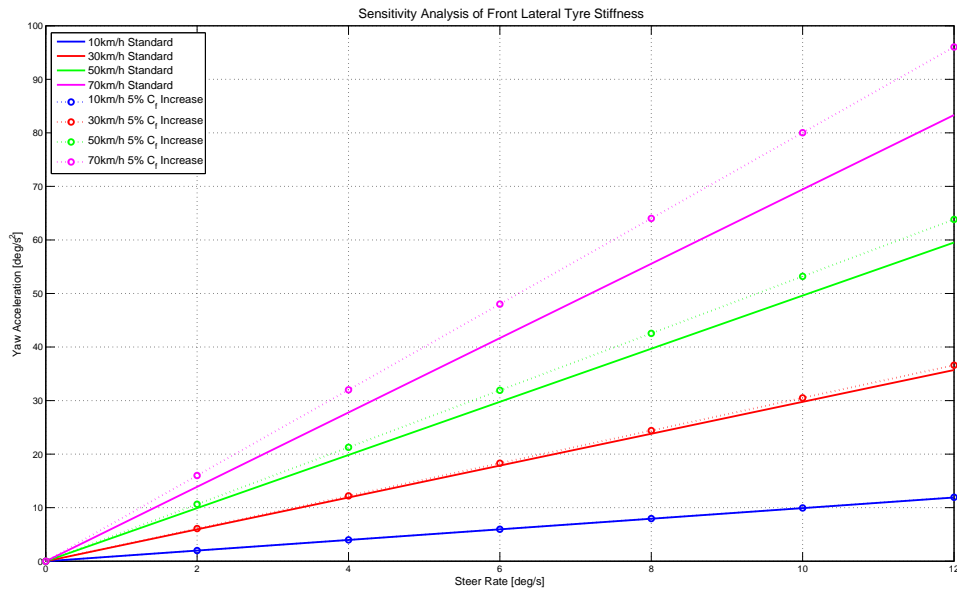
Figure 4.8: Sensitivity analysis of yaw acceleration gain with respect to front lateral tyre stiffness.
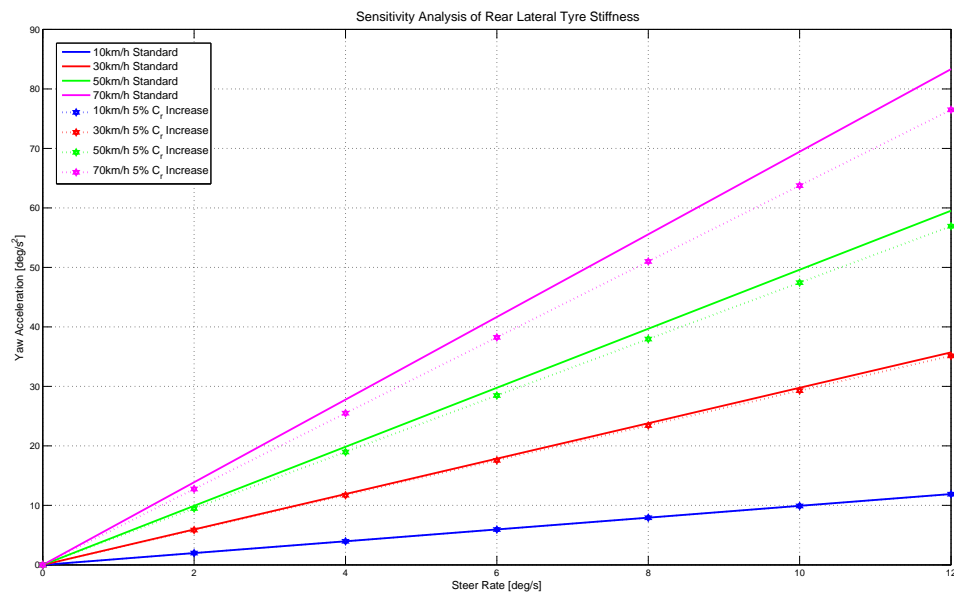
Figure 4.9: Sensitivity analysis of yaw acceleration gain with respect to rear lateral tyre stiffness.

DEPARTMENT OF MECHANICAL & AERONAUTICAL ENGINEERING

Figure 4.10 shows an analysis where both the front and rear lateral tyre stiffness are increased by 5%. It is observed that the effect is minimal, because the increase of both front and rear cornering stiffness partially cancels one another. An over steer handling still remains due to the fact that the distance from the CG to the rear wheels l_r is smaller than the distance to the front wheels l_f.
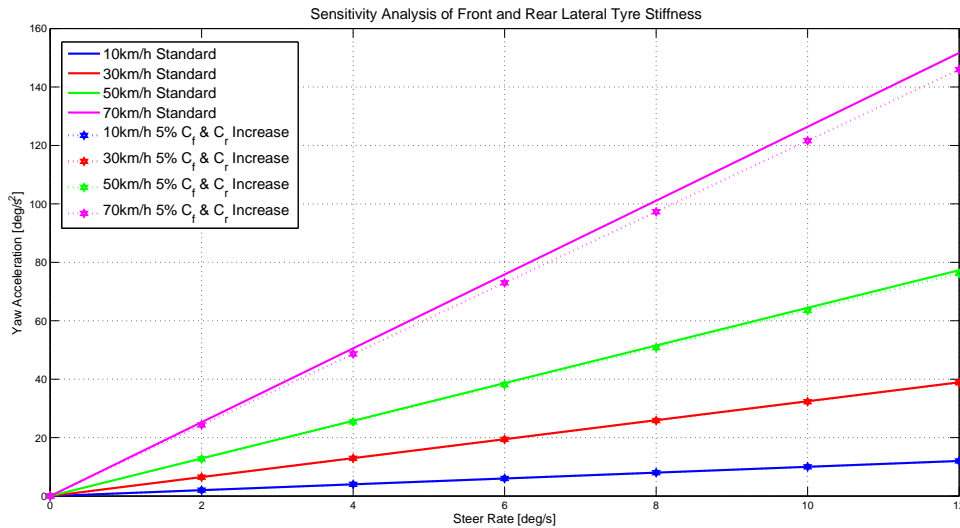
Figure 4.10: Sensitivity analysis of yaw acceleration gain with respect to front and rear lateral tyre stiffness.

4.5 Load Transfer and Tyre Force Generation Effects

The models developed in section 4.2 was based on the assumption that the weight on the front and rear wheels are split evenly left to right. However, due to the lateral acceleration experienced during cornering there is a load transfer from the inner to the outer wheel. As mentioned in section 1.3.2 the load transfer has a net effect of reducing the resultant lateral force depending on the amount of load transferred.

In the linear model it was also assumed that the cornering stiffness remains constant irrespective of the side-slip angle. In truth the cornering stiffness changes as the tyres produce either a lateral or a longitudinal force (i.e. change in side-slip angle, see section 1.2) or the vertical tyre load changes. The model developed in section 4.2 will be modified to make provision for both the load transfer and the reduction in cornering stiffness with an increase in side-slip angle.

4.5.1 Lateral Load Transfer

The load transfer presented in this section will be applied to both the linear model and the non-linear model.

The free body diagram shown in Figure 4.11 depicts the forces present during a cornering manoeuvre, the load transfer can be obtained as:

$$F_{zo} - F_{zi} \quad = \quad 2F_y \frac{h_r}{t} + 2K_\phi \frac{\phi}{t}, \tag{4.65}$$

where K_θ is an equivalent roll stiffness of the suspension.
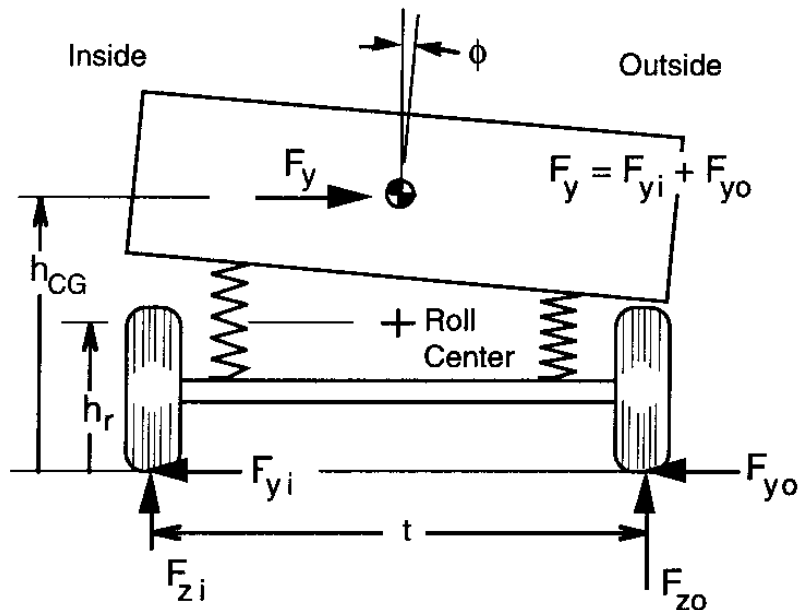
Figure 4.11: Force analysis of vehicle during cornering (Gillespie, 1992:211).

From (4.65) it is evident that there are two mechanism to the lateral load transfer. The first term is the load transfer due to the cornering forces which arises from the lateral force imposed on the axle. The load transfer is independent of vehicle roll and moment distribution and is also an instantaneous effect.

The second mechanism is a result of the vehicle roll and is thus dependant on the roll dynamics and the front/rear roll moment distribution. This mechanism may also have a phase lag which is related to the roll stiffness and damping. The phase lag is reduced with a higher roll stiffness and lower damping.

The load transfer due to the cornering forces can be divided into a front and rear axle component by simply making use of the cornering forces in the front and rear as:

$$\Delta F_{zf} = F_{yf} \frac{h_f}{t} \tag{4.66}$$

$$\Delta F_{zr} = F_{yr} \frac{h_r}{t} \tag{4.67}$$

Since the load transfer due to roll is dependant on the front/rear roll moment distribution, the whole vehicle needs to be considered. Figure 4.12 depicts the roll axis as a line connecting the roll centres in the front and rear.
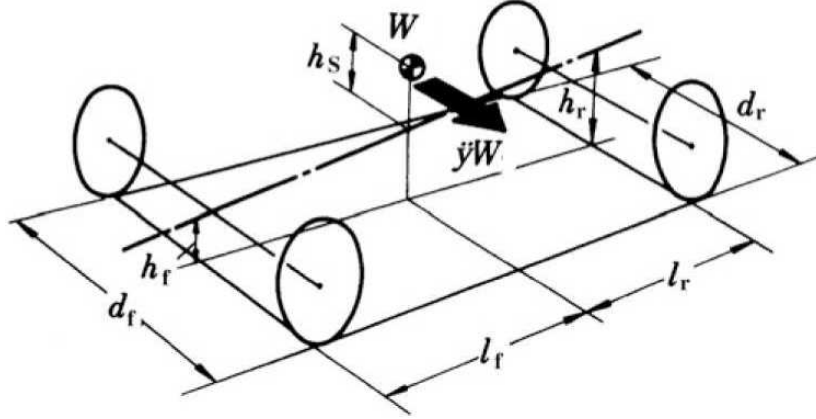
Figure 4.12: Vehicle roll axis and moment distribution (Abe, 2009:169).

The moment about the roll axis is then:

$$M_\phi = W_s h_s \sin \phi + m\ddot{y}h_s \cos \phi \tag{4.68}$$

The roll moment can also be expressed as:

$$M_\phi = M_{\phi f} + M_{\phi r} = (K_{\phi f} + K_{\phi r})\phi \tag{4.69}$$

Substituting (4.69) into (4.68) and assuming small angles, the roll angle can be obtained as:

$$\phi = \frac{mh_s}{K_{\phi f} + K_{\phi r} - W_s h_s} \tag{4.70}$$

From this it follows that the front and rear load transfer can be obtained as:

$$\Delta F_{zf} = \left[K_{\phi f} \frac{mh_s}{K_{\phi f} + K_{\phi r} - W_s h_s} + F_{yf}h_f \right] \frac{1}{t} \tag{4.71}$$

$$\Delta F_{zr} = \left[K_{\phi r} \frac{mh_s}{K_{\phi f} + K_{\phi r} - W_s h_s} + F_{yr}h_r \right] \frac{1}{t} \tag{4.72}$$

The final vertical load on the wheels can then simply be obtained by adding or subtracting the load transfer from the static load on the wheel.

$$F_{zf1} = F_{zf1,static} - \Delta F_{zf} \tag{4.73}$$

$$F_{zf2} = F_{zf2,static} + \Delta F_{zf} \tag{4.74}$$

$$F_{zr1} = F_{zr1,static} - \Delta F_{zr} \tag{4.75}$$

$$F_{zr2} = F_{zr2,static} + \Delta F_{zr} \tag{4.76}$$

Thus, the vertical load on each tyre can simply be obtained from the lateral acceleration. This means that the vertical load on each tyre can be estimated on-line by simply making use of an accelerometer measuring the lateral acceleration.

4.5.2 Tyre Force Generation

This section will deal with the generation of a lateral force only and not with longitudinal forces. During cornering the generation of a side-slip angle produces a lateral force. The more severe the manoeuvre - at high lateral acceleration - the more the increase in the side-slip angle. The side-slip angle can change to such an extent that the cornering stiffness changes. This change results in a change of gain between the steer rate and the yaw acceleration response.
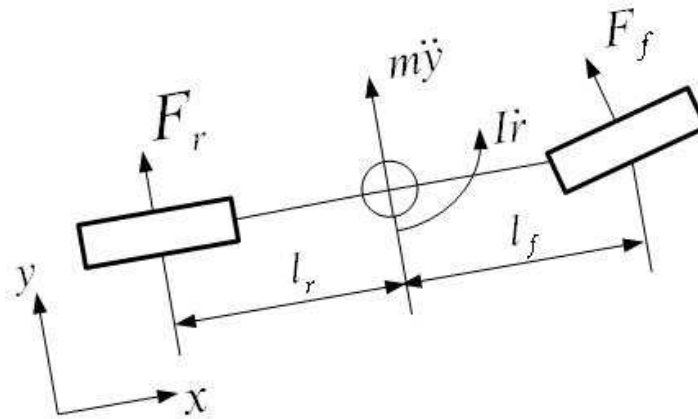
Figure 4.13: Free body diagram of vehicle during cornering.

Considering Figure 4.13 the equations of motion for the vehicle are:

$$m\ddot{y} = F_f + F_r \tag{4.77}$$

$$I\dot{r} = l_f F_f - l_r F_r \tag{4.78}$$

Solving for the front and rear axle forces.

$$F_r = \frac{l_f m\ddot{y} - I\dot{r}}{l_f + l_r} \tag{4.79}$$

$$F_f = m\ddot{y} - F_r \tag{4.80}$$

By assuming that the side-slip angles at the left and at the right tyres on each axle are equal (see (4.22) and (4.23)) and by making use of the calculated vertical forces, the individual front and rear tyre forces can be determined, as well as the respective side-slip angles. This can be done by making use of the Magic Formula and an iterative process. Given the vertical loads on both front tyres, it is possible to determine at which side-slip angle the combined tyre forces equal the axle force F_f determined in (4.80). Repeating this for the rear tyres will yield the side-slip angle present at each wheel. This relies on the assumption that the Magic Formula fit is available for the respective tyre and road, which may be obtained through experimental measurements.

Once each tyre force and side-slip angle has been determined, it is possible to determine the cornering stiffness of each tyre. This can be done by making use of finite differences and the Magic Formula as:

$$C \quad = \quad = \frac{MTF(\beta + \Delta\beta, F_z) - MTF(\beta, F_z)}{\Delta\beta} \tag{4.81}$$

where, MTF represent the Magic Formula given in 1.1. This procedure is then repeated for each tyre.

Once each tyre's cornering stiffness has been determined the stiffness in the linear model of section 4.2.1 can be replaced by:

$$2C_f \quad = \quad C_{f1} + C_{f2} \tag{4.82}$$
$$2C_r \quad = \quad C_{r1} + C_{r2} \tag{4.83}$$

This model requires two parameters to determine the cornering stiffness at each axle, namely the yaw acceleration and lateral acceleration. The lateral acceleration is used to quantify the amount of load transfer while both parameters are used to determine the lateral forces produced at each axle. The required yaw acceleration calculated to produce the required yaw angle change (3.3) can be used as the yaw acceleration parameter. This assumes that the yaw acceleration produced as a result of the steer rate input is the same as the required yaw acceleration. While there will be small differences between the actual and required yaw acceleration, the yaw acceleration has a minimal effect compared to the lateral acceleration. The small error will thus have a negligible effect. The lateral acceleration is thus the only additional parameter which is to be measured in order to quantify both the load transfer and the non-linearity of the tyre.

From the above a model can be derived which includes both the effect of the load transfer, as well as the non-linear tyre dynamics by simply measuring the lateral acceleration. From these parameters a linearised cornering stiffness C can be determined for all tyres. The new linearised values are used to update the values of the A and SM parameters as the lateral acceleration changes. Consequently, the steady state gain G is updated as well. This new updated gain can then be used to determine what steer rate is required to produce the required yaw acceleration using (4.57). Thus, as the lateral acceleration increases, the vehicle parameters are adjusted to better represent the vehicle handling at that instant. This produces a form of sliding mode control. The sliding mode control driver model is termed the Mathematical Model (MM) driver model.

4.6 Comparison of Models

Two separate models have now been developed in this chapter, the first model uses the set of differential equations developed in section 4.2. However, instead of using a linear tyre model the tyre lateral forces are modelled using the Pacejka '89 tyre model. Thus, the tyre forces are obtained by using the vertical load on each tyre obtained from the steady state lateral

acceleration model of section 4.5.1, as well as the side-slip angles obtained from equations (4.8)-(4.11). An investigation into whether this model is sufficiently accurate to construct the Inverse Magic Formula Model follows.

4.6.1 Simplified Model to Construct Inverse Magic Formula Model

If the simplified non-linear model is to be used to construct the Inverse Magic Formula Model the transient yaw acceleration response to a steer rate input must be similar to the full vehicle model with specific emphasis on the steady state response. Figures 4.14 and 4.15 displays the comparison between the full vehicle model and the simplified model yaw acceleration response for 20, 40, 60 and 80km/h.
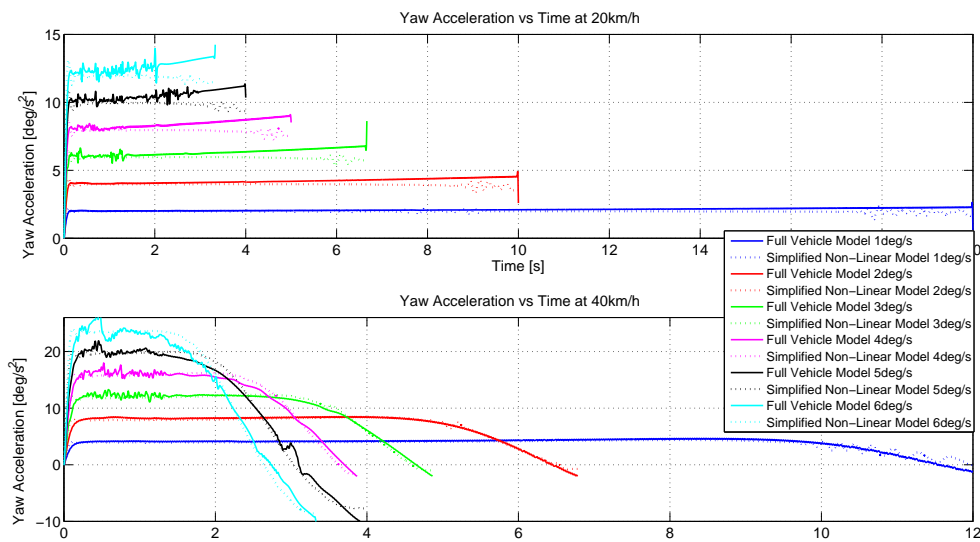
Figure 4.14: Comparison between simplified non-linear model and full vehicle simulation for the yaw acceleration response at 20 and 40km/h.

The two models compare very well and obtain very similar steady state values at all speeds. While the Inverse Magic Formula Model was not reconstructed with this model, the comparison shows that the same trends can be expected. It is also possible to construct the Inverse Magic Formula Model by means of experimental tests. However, this requires accurate measurement of either yaw rate or acceleration, as well as accurate control of wheel steer rate.
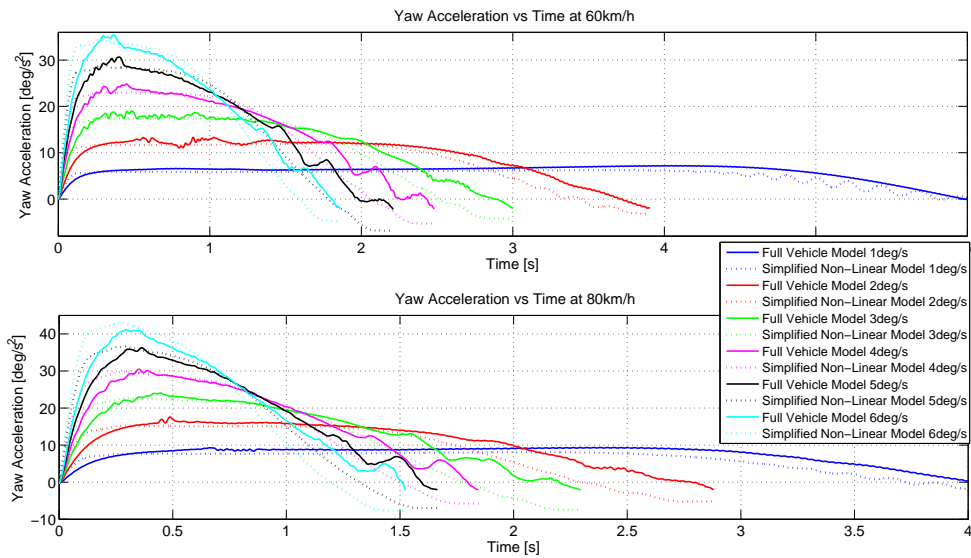
Figure 4.15: Comparison between simplified non-linear model and full vehicle simulation for the yaw acceleration response at 60 and 80km/h.

4.6.2 Mathematical Model (Simplified Sliding Mode Model) Comparison

The second model is the Mathematical Model driver model which can be directly used for control purposes replacing the Inverse Magic Formula Model. The vertical and lateral tyre forces as well as the side-slip angle will initially be used to validate the model. Finally, the yaw acceleration vs. lateral acceleration of the model will be compared to that of the full vehicle model.

The vertical tyre load of the MM driver model is compared to the full vehicle model while performing a sinusoidal path with increasing frequency at 60km/h (see Appendix B for a comparison at 120km/h). This path tests all levels of lateral acceleration - reaching a maximum of around 7m/s^2 -as well as varying input frequencies. For interest sake the simplified non-linear model is also included in the comparison.

Figure 4.16 depicts the vertical tyre load comparison. This figure indicates that the load transfer model used accurately determines the vertical loads on the tyres during cornering. It will be noted that the full vehicle model has a slight phase shift, which is due to the steady state assumption made in the load transfer model. The steady state assumption thus provides satisfactory results without increasing the complexity of the model as opposed to a roll differential equation.
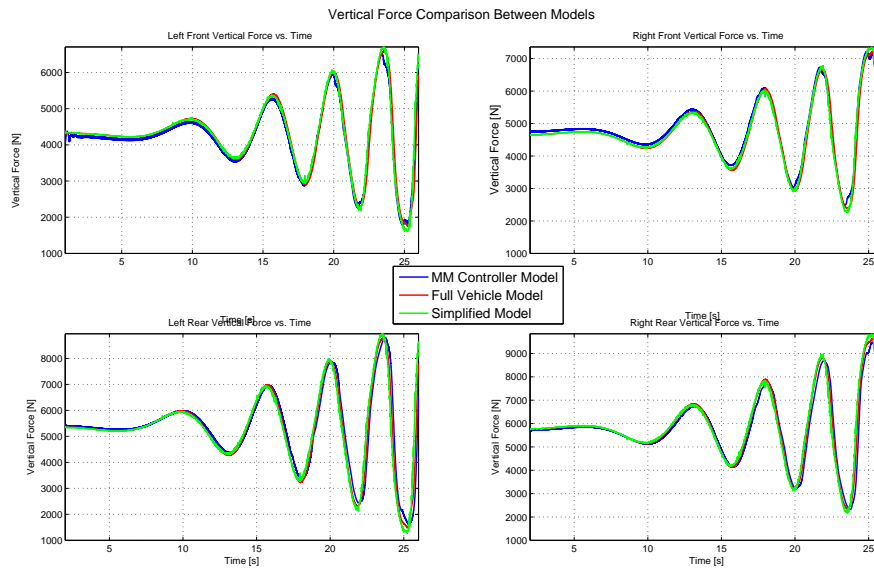
Figure 4.16: Comparison between simplified models and full vehicle simulation for vertical tyre load performing a sinusoidal path with increasing frequency at 60km/h.

The side-slip angle of the models are compared in Figure 4.17, the side-slip angle of all the models compare very well. Almost no difference between the non-linear and linearised side-slip angles can be seen. Thus, the assumption that the side-slip angles at the left and right wheels on each axle are equal, seems to be valid.
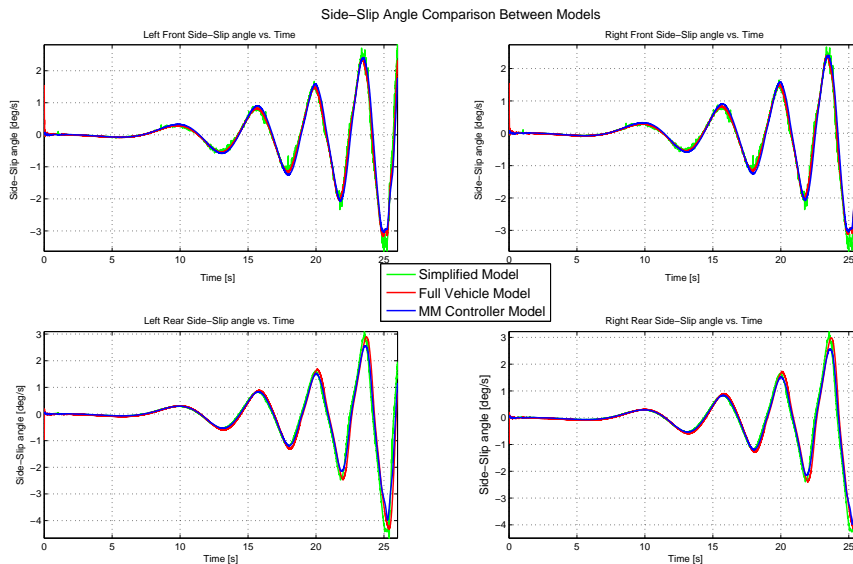
Figure 4.17: Comparison between simplified models and full vehicle simulation for side-slip angle performing a sinusoidal path with increasing frequency at 60km/h.

The lateral tyre force of all three models correlate very well as depicted in Figure 4.18. The effect of lateral load transfer on the vertical and, thus, the lateral force is evident from this figure. At high lateral acceleration about two thirds of the front and rear axle lateral forces are being carried by a single wheel.
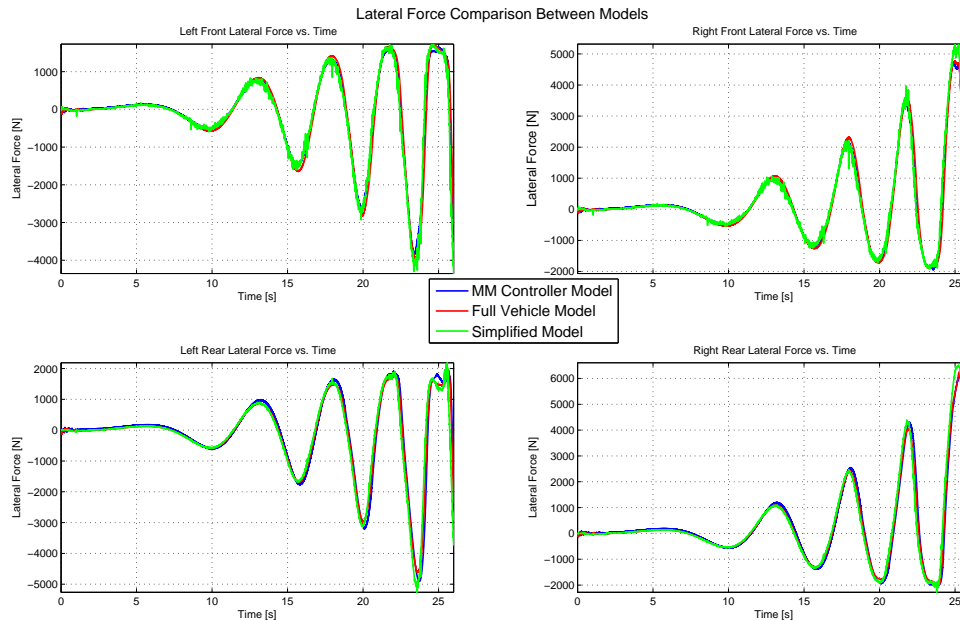

Figure 4.18: Comparison between simplified models and full vehicle simulation for lateral tyre force performing a sinusoidal path with increasing frequency at 60km/h.

Since both the vertical and lateral forces of each tyre are computed fairly accurately, the tyre cornering stiffness should be obtained fairly accurately as well. The yaw acceleration response of the MM driver model against lateral acceleration for a constant steer rate input at various vehicle speeds, compared to simulation results in Figure 4.19. The model correlates fairly well with the simulation results especially at lower speeds. The model captures the trend of decreasing yaw acceleration gain as the lateral acceleration increases. It is thus expected that the controller using this model will work better at higher lateral acceleration than the Inverse Magic Formula Model.
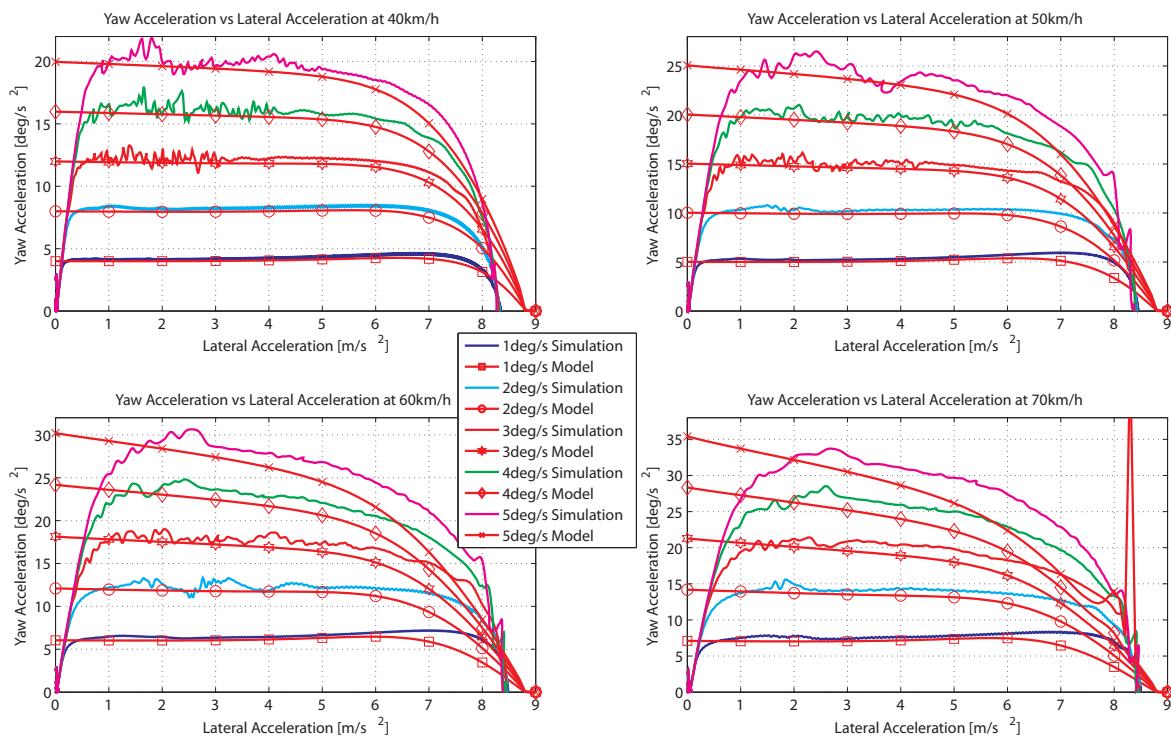
Figure 4.19: Comparison of MM driver model steady state yaw acceleration vs. steer rate and lateral acceleration with simulations results.

4.7 Mathematical Model Driver Model Simulation Results

The lateral position controller, discussed in section 3.4, is also added to the Mathematical Model driver model to obtain the final driver model. The complete driver model is evaluated based on its performance in controlling the full vehicle simulation model, through the same paths used to evaluate the Inverse Magic Formula Model. The MM driver model requires the measurement of the yaw rate, lateral acceleration, current heading and preview heading. The desired yaw acceleration can be determined by using the yaw rate, current heading and preview heading. The tyre vertical and lateral forces can be determined and thus the cornering stiffness by using the desired yaw acceleration and the measured lateral acceleration. The required steer rate can be determined by computing the gain in (4.51) and using the inverse relationship of (4.56). This desired steer rate coupled together with the PD controller provides the final output to the simulation.

4.7.1 Severe Double Lane Change

The same stated profile as used in section 3.5 is again employed. In Figures 4.20 and 4.21 it can be observed that the controller provides excellent control through a DLC at 40 and 70km/h. The performance at 40km/h is comparable to that of the Inverse Magic Formula Model. At 70km/h a slightly better performance is obtained compared to the Inverse Magic

Formula Model. Compared to the Inverse Magic Formula Model, the performance through a DLC of the Mathematical Model is on par or better at higher speeds.
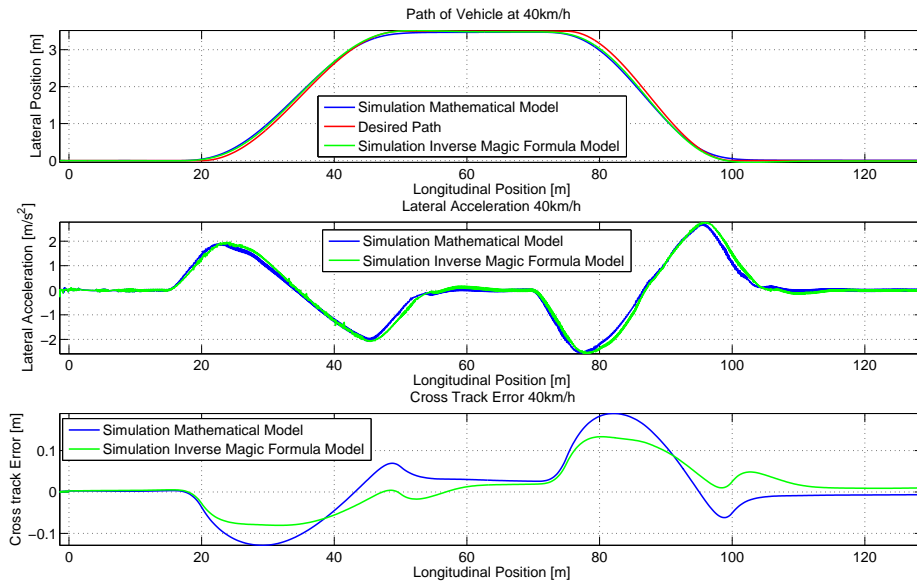
Figure 4.20: Performance of Mathematical Model controller through DLC at 40km/h.
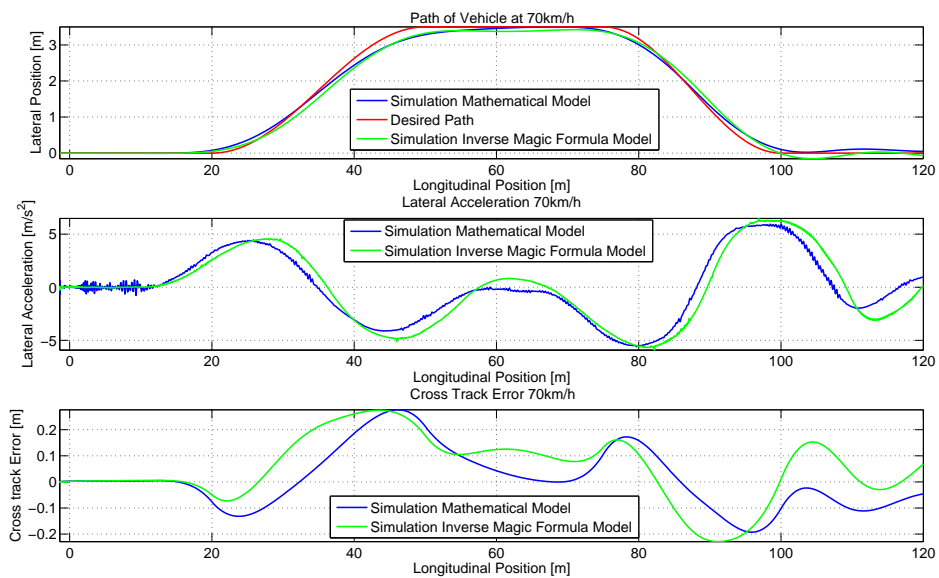
Figure 4.21: Performance of Mathematical Model controller through DLC at 70km/h.

4.7.2 Sinusoidal Path with Increasing Frequency

From Figure 4.22 it is clear that the controller provides a stable output allowing the vehicle to follow the path fairly well at higher lateral acceleration. When the tyre forces saturate at around 0.84g, the vehicle simply slides out as it is impossible to follow the desired path further. Thus, the Mathematical Model driver model remains stable at the urban driving speed of 60km/h. Compared to the Inverse Magic Formula Model, the Mathematical Model has smaller lateral errors thus providing better path following at higher lateral accelerations.
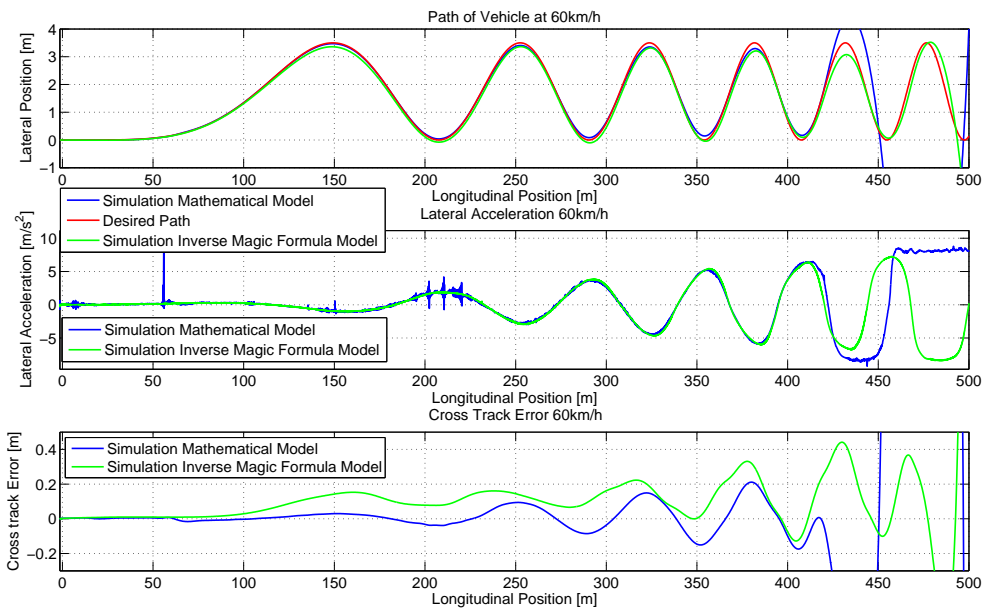
Figure 4.22: Performance of Mathematical Model controller through sinusoidal path with increasing frequency at 60km/h.

Figure 4.23 displays the vehicle following the increasing frequency path at 120km/h. The controller performs path following at highway speeds better than the Inverse Magic Formula Model. As mentioned before the Inverse Magic Formula Model is not directly modelled for speeds higher than 90km/h while the Mathematical Model driver model is modelled for all vehicle speeds. Thus, it is no surprise that better performance at higher speeds are obtained. The test also shows that if stability is to be maintained when the vehicle is to follow a path at lateral accelerations greater than is possible, the vehicle has to follow a path less severe than the desired path (or reduce vehicle speed). Due to the better performance at higher lateral accelerations the lateral error of the Mathematical Model is smaller. The vehicle thus reaches its traction limit sooner (thus sliding out sooner), compared to the Inverse Magic Formula Model.
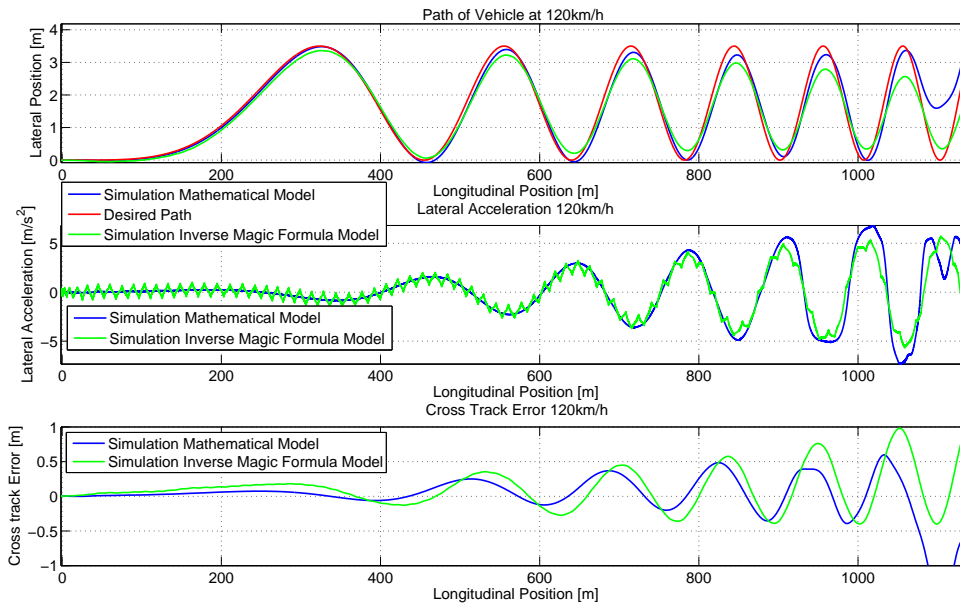
Figure 4.23: Performance of Mathematical Model controller through sinusoidal path with increasing frequency at 120km/h.

Effect of Input Frequency

The effect of various input frequencies is depicted in Figure 4.24, the figure shows good path following at all input frequencies comparable to that of the Inverse Magic Formula Model (reproduced in Figure 4.25 for convenience). The average lateral acceleration experienced is around 5m/s^2. This shows that the vehicle remains stable at all input frequencies and a fairly high lateral acceleration.
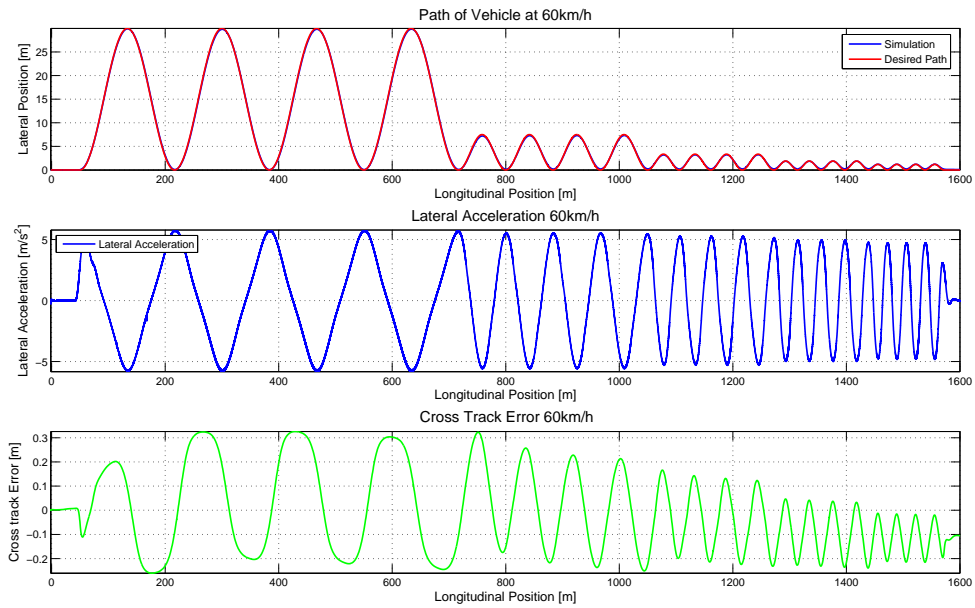
Figure 4.24: Mathematical Model controller through discrete input frequencies at 60km/h.
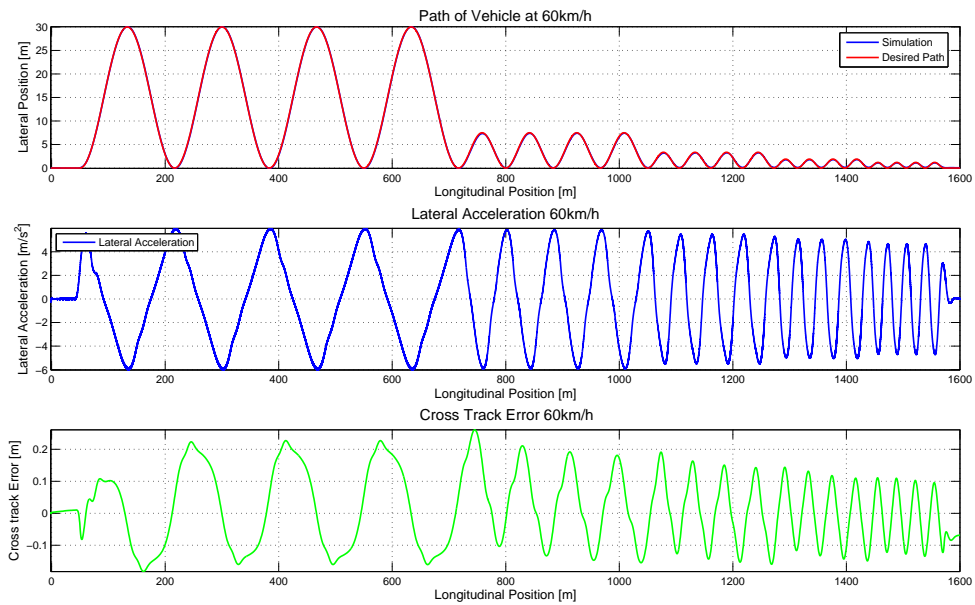
Figure 4.25: Inverse Magic Formula Model through discrete input frequencies at 60km/h.

4.7.3 S-Curve

The s-curve path at both 60km/h and 120km/h in much tighter turns than typical urban roads, shows that the controller allows satisfactory path following at both low and high speeds.
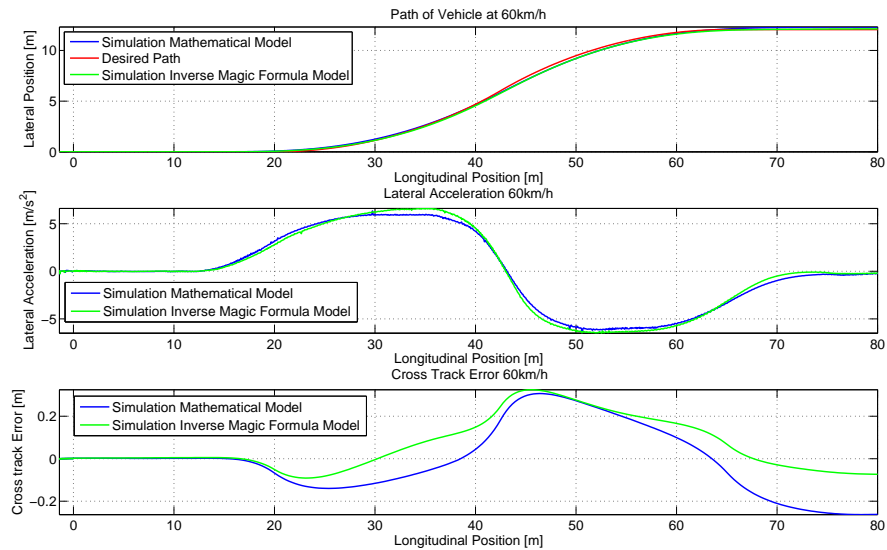
Figure 4.26: Performance of Mathematical Model through 45m radii s-curve at 60km/h.
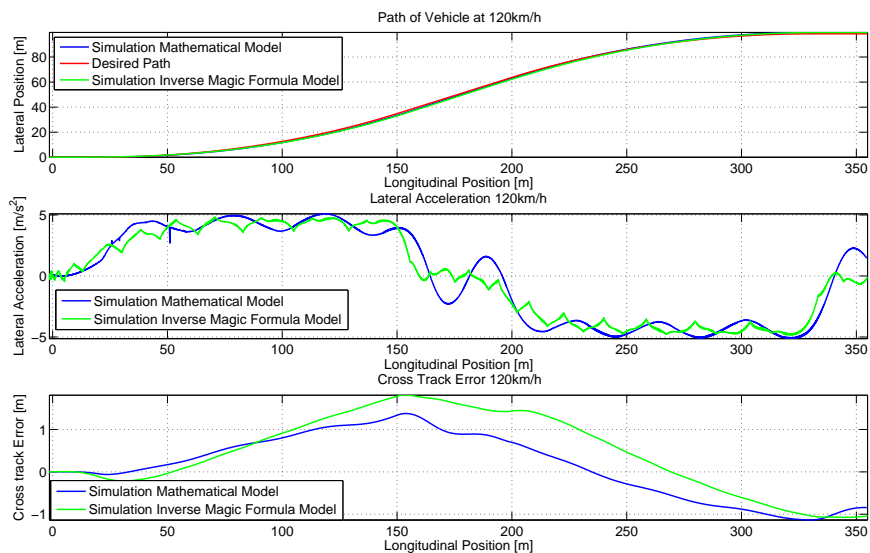
Figure 4.27: Performance of Mathematical Model through 260m radii s-curve at 120km/h.

4.8 Open-loop Stepper Motor Controller

Driver models have now been develop which has the front wheels steer rate as output. Thus, a controller still needs to be developed which can assure that the front wheels steer at the required steer rate. Since a steer rate as opposed to steer angle is required, it is possible to use a open loop control strategy. This is because speed control of electric motors and especially stepper motors are easy to implement. Thus, there is no need for a sensor which can accurately provide feedback of steer rate or steer angle as long as the open loop control operates as required. This makes the system easier and cheaper to implement.

The stepper motor of section 2.1.4, used in combination with the Festo's CMMS-ST stepper controller which incorporates microstepping (allowing for smaller incremental steps) and allows for a total of 2048 steps per revolution. The controller is set to synchronisation mode which allows the stepper motor to rotate one step per single pulse provided. The speed of the motor can thus be controlled by providing a certain amount of pulses per second or stepping frequency. Input to the controller is thus a stepping frequency and a direction (either clockwise or anti-clockwise). The stepping frequency is obtained by means of a Voltage to Frequency (V/F) converter. The V/F converter allows any frequency to be obtained by means of a simple voltage output which can be generated from most data acquisitioning devices. The V/F converter is adjusted to deliver 4096Hz at a full scale voltage of 5V, thus allowing a maximum stepper motor speed of 2 revolutions per second or $720°/s$. As mentioned in section 2.1.4 the maximum speed was selected on the basis of the NHTSA's fishhook rollover test procedure. This enables the same actuator to be used in rollover testing.

Slight modifications to the steering system were made, such as the removal of one intermediate shaft to reduce overall length. This allowed for better positioning and reduced the angles formed by the universal joints. All universal joint connections were equipped with grub screws to remove as much free play within the system as possible.

It can generally be assumed that a stepper motor would not have any slippage since it would rotate a set amount as long as the required torque is below the nominal torque. If the required torque is larger than the motor's nominal torque the stepper motor would be incapable of stepping at all, thus the assumption of no slippage can be made. With this assumption a basic transfer function for the stepper motor's rotational speed from the input voltage to the V/F converter can be obtained as:

$$\dot{\omega}_a = \left(\frac{revolutions}{steps}\right)\left(\frac{deg}{revolutions}\right) V/F \tag{4.84}$$

$$= \left(\frac{1}{2048}\right)\left(\frac{360}{1}\right)\left(\frac{4096}{5}\right) \tag{4.85}$$

$$= 144 \ deg/s/V \tag{4.86}$$

The steering box has a reduction ratio of 22 from steering wheel to tyre. Incorporating this into Equation (4.86) we obtain a final transfer function for the tyre steering rate to V/F converter input as:

$$\dot{\omega}_{tyre} \quad = \quad n_{steerboxratio} \left(\frac{revolutions}{steps} \right) \left(\frac{deg}{revolutions} \right) V/F \qquad (4.87)$$

$$= \quad \left(\frac{1}{22} \right) \left(\frac{1}{2048} \right) \left(\frac{360}{1} \right) \left(\frac{4096}{5} \right) \qquad (4.88)$$

$$= \quad 6.55 \ deg/s/V \qquad (4.89)$$

4.9 Open-loop Stepper Motor Tests

Tests were conducted using the stepper motor model given in Equation (4.89) to determine the performance of the stepper motor (with 24V motor supply) under load (wheels on ground) with a vehicle speed 5-10km/h. These tests included ramp as well as sinusoidal steer rate inputs. Figure 4.28 depicts the result from a ramp test where an initial response of 5deg/s was desired and increasing at 0.15deg/s^2. The settling time from full clockwise to anti-clockwise rotation for all response magnitudes (not significantly affected by rotation speed) was determined to range between 0.2-0.3s.
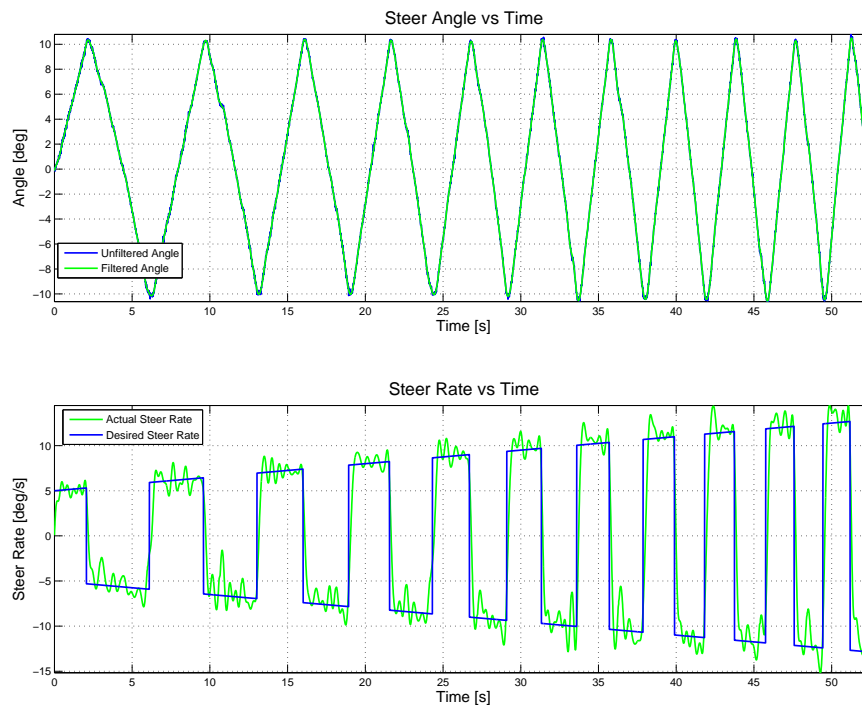
Figure 4.28: Stepper motor response to ramp input.

The slight oscillations around the set point are most likely caused by the universal joint connecting the stepper motor and steering box which are not perfectly in plane. It can however be concluded that the open loop control of the stepper motor provides reasonable set point following with an acceptable settling time.

A sinusoidal input which resembles the steer rate required to perform a DLC at 80km/h was also used. The results, shown in Figure 4.29, indicate that the largest response time delay occurs when changing the direction of rotation. The delay could be attributed to play in the steering system which causes a dead band in the system. From the angle graph in the top plot it can be observed that the angle has a slight drift. The drift would indicate that the motor in combination with the non-linear steering system kinematics has a slightly better response in one rotational direction than the other. The motor response and model is deemed sufficient for the intended purpose.
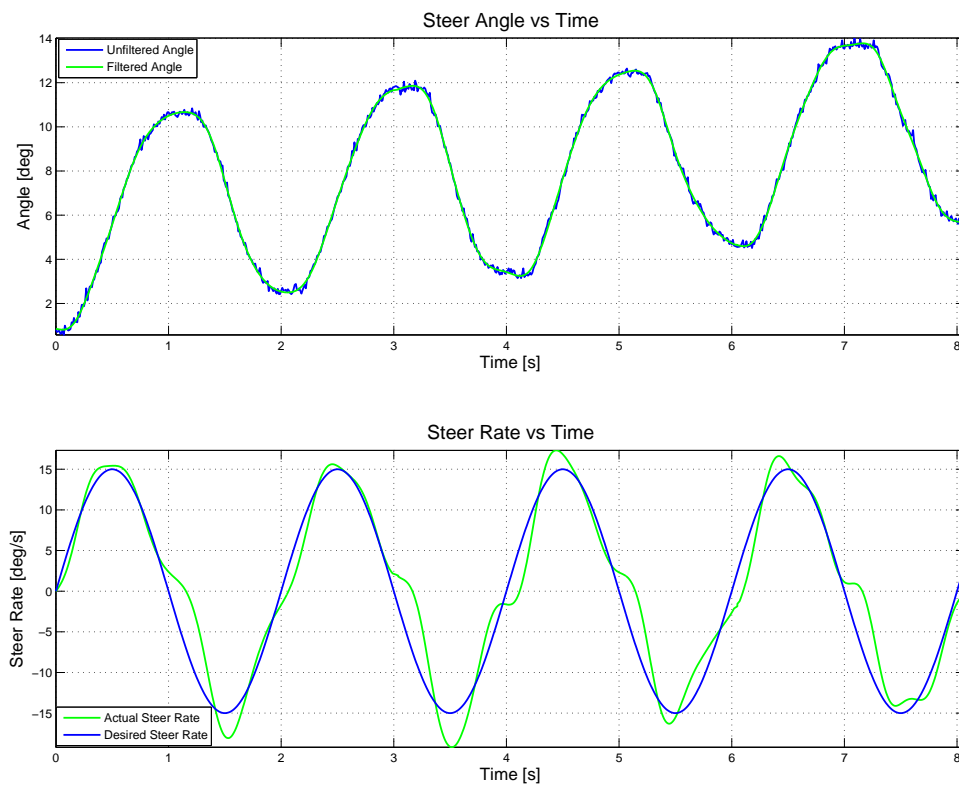
Figure 4.29: Stepper motor response to 0.5Hz, 15deg/s magnitude sinusoidal input.

The Mathematical Model driver model, with open-loop stepper motor controller, is shown in the block diagram of Figure 4.30.
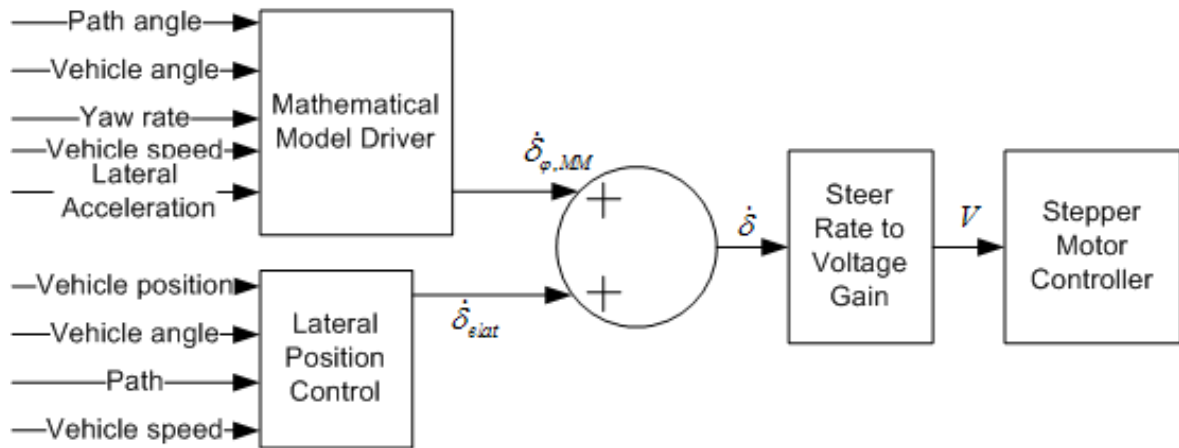
Figure 4.30: Block diagram of the Mathematical Model driver model.

4.10 Conclusion

The developed simplified non-linear model with load transfer provides a similar yaw acceleration response as the full vehicle model. This model is sufficient in replicating the relationship which is presented by the Inverse Magic Formula Model. This model is much simpler and requires a fraction of the computation time required by the full vehicle model.

The linear model developed, clearly illustrates that a steady state yaw acceleration response is obtained from a constant steer rate. This response does however decrease with higher lateral accelerations mainly caused by the load transfer and force generation of the tyres causing the tyres to saturate. The Mathematical Model incorporating sliding mode, which takes these effects into account, displays the same yaw acceleration vs. lateral acceleration trend as the full vehicle simulation results. This controller successfully allows the vehicle to navigate through a DLC at both low and high speeds. The controller also remains stable at high lateral acceleration as well as at higher frequency inputs.

A simple open loop control showed satisfactory results in controlling the front wheel steer rate as desired. The open loop control does not require the need for a sensor which can accurately measure the front wheel steer rate or even steer angle. Thus, making the system easier and cheaper to implement.

Chapters 6 discusses the experimental validation of both the Inverse Magic Formula Model and Mathematical Model combined with the lateral position control. Chapter 5 discusses global navigation satellite systems which are often used to provide satellite navigation to civilians. A system which is more accurate than typically found in vehicles, is used to provide position information to the control system.

Chapter 5

Global Navigation Satellite Systems

Thus far, this study has concentrated on the development of the two driver models, namely the Inverse Magic Formula Model and the Mathematical Model. These driver models require only a few inputs such as the yaw rate obtained from a gyroscope, as well as the vehicle speed and position - and lateral acceleration for the Mathematical Model. It is also assumed that the vehicle has to follow a predetermined path. The path planning aspects of autonomous control is therefore not considered, only the path following aspect.

There are several ways in which vehicle position can be determined, such as the use of stereo vision or Light Detection and Ranging (LIDAR) (Thrun et al, 2006), or the use of magnetic pickups in the road (Yoshida, 2010). However, most of these methods require considerable postprocessing to obtain vehicle position and are fairly expensive. Both stereo vision and LIDAR provide in addition to position, the benefit that it can determine whether an obstacle is blocking the vehicle path. These two methods are also susceptible to vehicle vibration, rolling and pitching. Additional postprocessing or the use of a very stable inertial platform is required on which they are mounted to remove these effects. Magnetic pickups are a viable method, but also requires numerous powerful magnets, which either need to be permanently embedded or securely fixed to the road. This method also adds significant infrastructure costs.

Another method of positioning is to make use of a Global Navigation Satellite System (GNSS), whereby an object's position can be located via satellites orbiting the globe. This technology has advanced to such an extent in recent years that positioning within a few centimetres is possible. This solution is very portable and easy to use, requiring almost no postprocessing to obtain vehicle position. For these reasons it was the method of choice for determining vehicle positioning, as well as vehicle speed. The focus of this chapter is on the basics behind this technique, as well as various factors affecting Global Navigation Satellite Systems' accuracy. The conversion of latitude and longitude values to Cartesian coordinates, as well as tests conducted on the available system are provided in this chapter.

5.1 Introduction to Global Navigation Satellite Systems

GNSS is a term used to refer to a constellation of satellites used as satellite navigation systems (sat-nav). These systems provide autonomous geo-spatial positioning with global coverage. The system consists of a constellation of satellites which orbit the earth at a known orbit. The positions of the satellites are thus accurately known. Each satellite sends out a signal which contains both the satellite's position as well as the time the signal was sent. The time on board a satellite is maintained to a very high degree of accuracy by means of an atomic clock. A receiver acquires these signals and can determine the distance from a satellite by determining the time of flight for the signal and using the speed the signal travels at - typically near the speed of light. The time of flight is computed using the receiver's built-in clock. The receiver generates the same signal being broadcasted by the satellite and determines the phase between these signals by delaying the internal signal until the signals line up (Corvallis Microtechnology, 1996 and Trimble, 2010). The more accurate the built-in clock, the more accurate the positioning. Typically, normal quartz crystals are used due to the cost of more advanced timers such as the atomic clocks aboard the satellites. In general the time can be measured to about 1% of one-width, that is to say 1% of the signal period. This creates a spherical range about the satellite where the receiver could possibly be stationed. The position can be refined by combining the distances from a number of satellites as depicted in Figure 5.1. The position in all three dimensions can be obtained by combining a minimum of four satellites' spherical range.

Currently there are two complete operational GNSS systems, the Global Positioning System (GPS) and GLObal NAvigation Satellite System (GLONASS). The GPS system is widely known and is the system developed by the US Department of Defence (DOD) and contains around 30 working satellites. GLONASS has been developed by the Russian Space Forces with 24 operational satellites.

5.2 GNSS Accuracy

There are various factors which influence GNSS accuracy. Some of these factors can be compensated for to improve accuracy. This section provides a summary of most of the factors influencing GNNS accuracy as well as techniques used to improve accuracy.

5.2.1 Atmospheric Conditions

The earth's ionosphere and troposphere refract the GNSS signals. As a result, the speed at which the GNSS signal passes through these layers differs from the speed through space. Thus, the speed of light does not remain constant. This effect can cause as large as 0-30m errors (Corvallis Microtechnology, 1996).
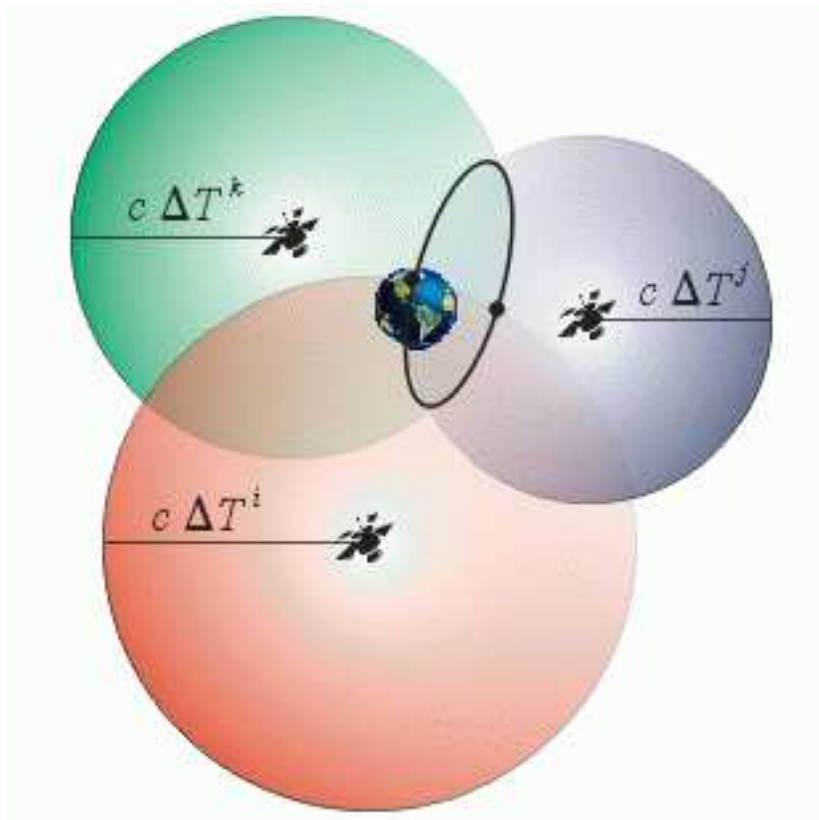
Figure 5.1: Satellite navigation: obtaining position of receiver (Bernstein, 2010).

5.2.2 Ephemeris Errors/Clock Drift/Measurement Noise

Ephemeris error or orbital position errors are sent from each satellite to increase accuracy. However, the model used to determine satellite position may not be entirely accurate. The same problem is inherent in the modeling of the rate of clock drift. The addition of measurement noise adds additional distortion of the signals. All of these effects can further increase positional error.

5.2.3 Selective Availability

Selective Availability (SA) is the intentional alteration of the time and ephemeris signals by the DOD. These alterations were made in the past to reduce the accuracy of the GPS signals which normal civilians have access to. This was in an attempt to reduce the possibility that the widely accessible GPS system was used against the USA as a means of targeting missiles or other incendiary devices. This can introduce as much as 70m horizontal positioning errors (Corvallis Microtechnology, 1996). However, as of 2 May 2000 SA was switched off to allow civilians and manufacturers access to more accurate GPS systems. All GPS satellites still, however, produce another signal at a different frequency which is encoded to prevent civilians from having access to the information. The military make use of both this signal and the

normal signal to improve the accuracy of GPS. GLONASS satellites do not have SA and are thus not affected by it.

5.2.4   Multipath

Multipath is the phenomenon whereby the GNSS signal bounces of reflective surfaces before reaching the receiver, thus travelling further distances. The receiver can also receive the original signal and reflected parts which arrive later. Most advanced GNSS systems can distinguish between the original and the reflected signals. However, if the receiver only receives the signals which were reflected, this could result in position errors as much as 1m (Corvallis Microtechnology, 1996).

5.2.5   Dilution of Precision

The factors affecting the accuracy mentioned above are predominately external factors. Another major factor is the geometry or alignment of the satellite constellation in view by the receiver. The accuracy of the GNSS is evaluated for several factors based on the satellite geometry, all of which fall into the category Dilution of Precision (DOP). Figures 5.2a and 5.2c show satellite constellations where the DOP is high. This indicates a poor satellite measurement configuration. A low DOP (shown in Figures 5.2b and 5.2d) represents a satellite constellation with a better measurement configuration (Corvallis Microtechnology, 1996).

The DOP value changes throughout the day, thus there will be periods where the satellite configuration will provide better accuracy and periods with worse accuracy. If more satellites are used - for instance using both GLONASS and GPS satellites - the possibility that a low DOP value is obtained is higher. As a result of the change in DOP it will generally be observed that tests requiring good GNSS accuracy are scheduled during specific periods of the day with low DOP values.

5.3   Increasing GNSS Accuracy

Three methods are mainly used when improving GNSS accuracy, namely:

- Differential GPS (DGPS)

- Carrier Phase receivers or Dual-Frequency receivers

- Inertial navigation

5.3.1   Differential GPS

Differential GPS (DGPS) is a means to improve accuracy by means of a known fixed location. An additional GNSS receiver is used with a fixed position to provide correctional data. Since the receiver remains stationary, the location of the receiver is either known or is determined

(a) Satellite constellation showing a high DOP value and thus poor measurement configuration.

(b) Satellite constellation showing a low DOP value and thus better measurement configuration.
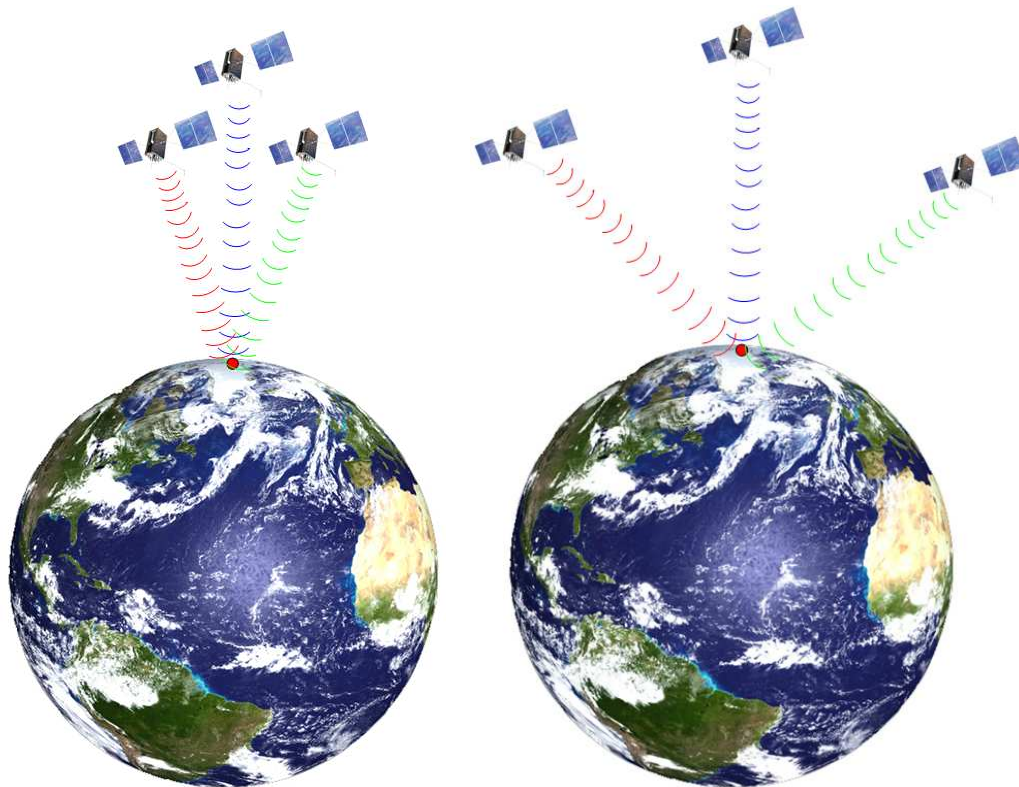
(c) Satellite constellation showing a high DOP value and thus poor measurement configuration.

(d) Satellite constellation showing a low DOP value and thus better measurement configuration.

Figure 5.2: Dilution Of Precision of various satellite geometry.

by averaging its GNSS location over a period of time, typically 20min. The receiver can then compute the difference between its known location and the location provided by the GNSS. This difference is then broadcasted to moving GNSS receivers allowing them to improve their positional accuracy.

There are a few ways in which to acquire the correctional data for DGPS. There are currently a few ground reference stations which calculates GPS correctional messages such as ionospheric delays, individual satellite clock drift and so forth. The correctional data is then send via separate satellites to GPS receivers. This results in a large area with correctional data known as Wide Area Augmentation System (WAAS). Currently most of these WAAS stations are in North America with a few being developed in Europe and Japan. Another method known as Local Area Augmentation System (LAAS) which provides similar correctional data to WAAS is also available. In LAAS correctional data is sent from local sources such as airports where accurate positioning is needed. The correctional data is available to all within a 30-50 km range of the local source. (Federal Aviation Administration, 2011).

5.3.2 Carrier Phase receivers or Dual-Frequency receivers

The GPS system transmits two signals, namely the L1 and L2 carrier waves transmitted at 1575.42MHz and 1227.60MHz respectively. The L1 signal is used to carry Clear/Acquisition (C/A) code, also known as the civilian code. The L2 frequency carriers the Protected-code or P-code. This code is only available to the USA military and other authorised users. These codes are modulated onto the carrier waves transmitting at a frequency 1540 or 1200 times lower than the carrier wave. Figure 5.3 illustrates typical signal modulation (Universal Tracking, 2010).

It was noted earlier that the signal time of flight can only be measured up to 1% of the period of the signal. Thus, using the normal C/A code running around 1.023 MHz (0.98μ s period) it is possible to achieve an accuracy of 0.01 μs. This relates to an accuracy of 3m, using the military P-code running at 10.23MHz an accuracy of 30cm is possible, this is termed the ambiguity of the signal (Universal Tracking, 2010).

Another means to improve accuracy known Carrier-Phase Enhancement (CPGPS) is also used. This technique utilises the 1.575 GHz L1 carrier wave to determine the distance between the receiver and the satellites. Thus, an error of $\pm1\%$ in L1 carrier phase measurement results in a ±1.9mm error in baseline estimation. This is also more commonly known as Real Time Kinematic (RTK) technique. The difficulty in a RTK system is the aligning of the internal and external signals. The navigation signals (C/A code) are deliberately encoded in order to allow them to be aligned easily, whereas every cycle of the carrier wave is similar to every other cycle. Thus, making it extremely difficult determine whether proper alignment has been achieved or whether the signal is "off by one", thus introducing an error of 20cm or a multiple thereof. This ambiguity can be addressed to some extent by making use of statistical methods on the C/A signal (Universal Tracking, 2010).
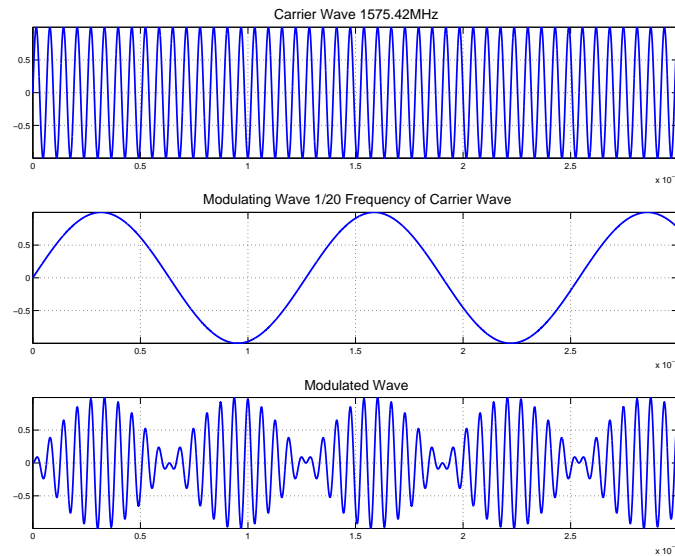
Figure 5.3: Signal modulation where carrier wave is transmitted at a frequency 20 times higher than the data signal.

This method can be enhanced by employing this technique on both the L1 and L2 signals. Since the signals differ in broadcast frequency they will be affected differently through the ionosphere, as such it is possible to calculate the ionosphere effect and reduce its influence. Receivers that use both L1 and L2 signals in this way is more commonly known as dual frequency receivers (Universal Tracking, 2010).

5.3.3 Inertial Navigation System

Inertial Navigation Systems (INS) are typically employed on aircraft, submarines, spacecraft and guided missiles as they can at times be thousands of kilometres away from a fixed base station. As a result, inertial measurement units are used. These systems commonly consist of a GNSS receiver, gyroscopes and accelerometers. An INS system starts off with a known location provided by GNSS or other means. By integrating the information supplied by all the measurement units the system can compute its own updated position. These systems suffer from integration drift due to small errors made in measurements of the accelerations and velocities. As a result the integrated position becomes slightly affected. These position errors are compounded resulting in larger errors over time. Consequently, these systems require a reset in absolute position every now and then. These systems are generally costly, because they require almost no external reference they do not suffer from the problems affecting normal GNSS systems (Universal Tracking, 2010).

5.4 Converting Longitude and Latitude to Cartesian Coordinates

To facilitate the implementation of a controller it is desirable to represent the positional coordinates in terms of Cartesian X-Y coordinates rather than geodetic latitude and longitude. Latitude and longitude can be converted to linear Cartesian coordinates by means of a suitable earth model. Various models are used for a variety of applications ranging from simple spherical to more complex ellipsoidal models that consider the flattening of the earth. At the basis of the models are the relationship between a circle's arc length and radius given as:

$$s = r_{arc}\theta \tag{5.1}$$

Most models differ in how this radius is derived, with some making use of different radii that are used for the latitudinal and longitudinal directions. The radius of the longitudinal coordinate is also dependent on the latitude as depicted in Figure 5.4.
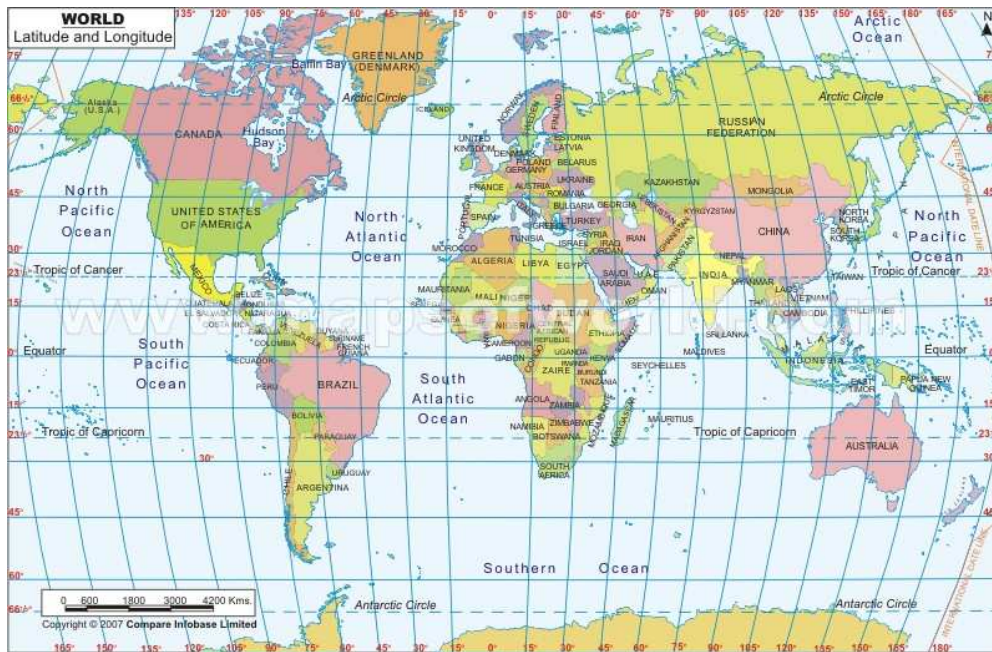
Figure 5.4: Latitude and longitude of earth (Segura, 2010).

Using a spherical model the latitude and longitude can be converted by means of (Clynch, 2006):

$$dN = Rd\phi \tag{5.2}$$
$$dE = R\cos\phi d\lambda \tag{5.3}$$

where R represents the radius of the earth, ϕ is the latitude and λ is the longitude. The parameters dN and dE represent the Cartesian coordinates in the Northern and Eastern directions respectively. Taking North as Y and East as X we obtain the position in terms of $X - Y$ coordinates.

For an ellipsoidal earth model there are three radii each which are a function of latitude. The two which are most frequently used are called the radii of curvature as presented in Figure 5.5. These radii are termed the radius of curvature in the prime vertical R_n and radius of curvature in the meridian R_m. Using these radii the coordinates can be linearised according to Clynch (2006):

$$
\begin{aligned}
dN &= R_m d\phi & (5.4) \\
dE &= R_n \cos \phi d\lambda & (5.5)
\end{aligned}
$$

these radii can then be determined as:

$$
\begin{aligned}
R_n &= \frac{a}{\sqrt{1 - e^2 \sin^2 \phi}} & (5.6) \\
R_m &= R_n \frac{1 - e^2}{1 - e^2 \sin^2 \phi} & (5.7)
\end{aligned}
$$

where e represents the flattening of the earth, given as:

$$
e = \sqrt{1 - \frac{b^2}{a^2}} \tag{5.8}
$$

with a being the semi-major axis (equatorial radius) and b the semi-minor axis (polar radius) of the ellipsoid. Using these formula the longitude and latitude can easily be converted to an accurate linear X-Y coordinates expressed in meters. GNSS systems typically also provide both heading (typically measured from North or Y axis) and speed which are determined directly from the position coordinates.
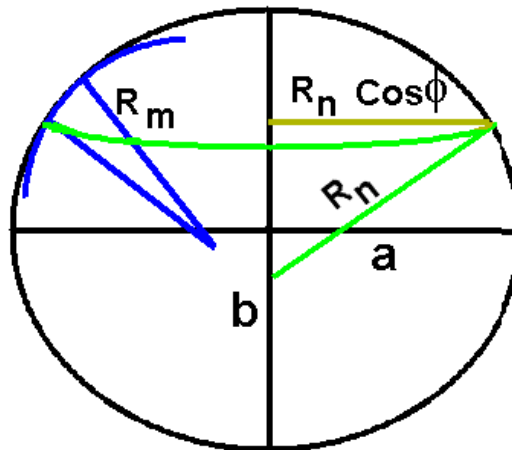
Figure 5.5: Radii of curvature (Clynch, 2006).

5.5 GNSS Performance Tests

As mentioned, this study is only concerned with path following and the aim is to obtain position as well as heading feedback from Racelogic's VBOX3, a 50Hz, 2cm RTK DGPS system (Racelogic, 2010). The system boasts a position accuracy of 2cm and heading accuracy of 0.1° on RTK mode using both GPS and GLONASS satellites. Before using this system in vehicle testing, it is required to ascertain its performance in the proposed test environment.

5.5.1 Accuracy

For the purposes of this study two tests were conducted to evaluate the performance of the GNSS. The first was to determine both accuracy and latency of the GNSS receiver. The second test was to test the consistency of the receiver. The first test was conducted by placing the GNSS antennae on an X-Y table of which the table's X-Y positions are measured using linear displacement transducers. The result of the test is shown in Figure 5.6. This figure indicates that the accuracy of the GNSS is sufficient with errors smaller than 100mm, but there is also some drift in the system. Better results could have been obtained by conducting the test in a better environment since various buildings were present causing multipath error effects. The system could have been left stationary for longer to obtain better positioning accuracy as well. The GNSS system, although not achieving its published specification of 2cm in the test environment, shows adequate accuracy and negligible latency needed for use in positioning in the driver models.
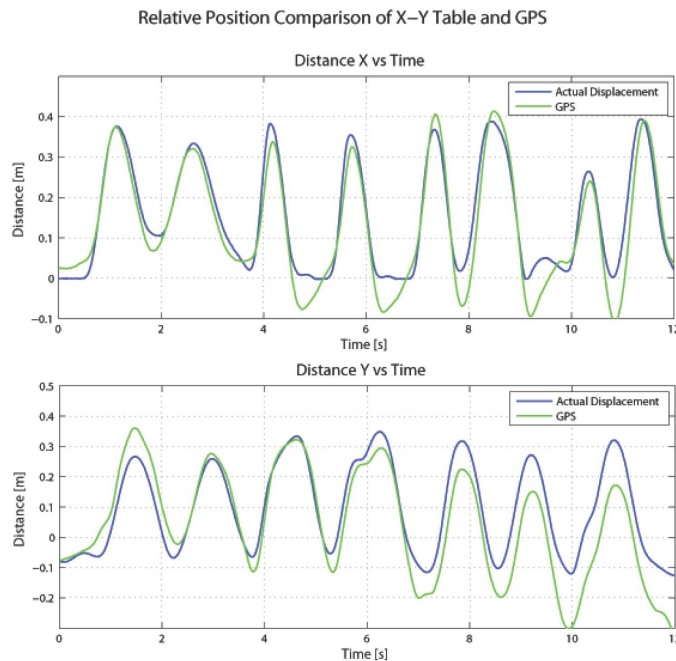

Figure 5.6: Positional accuracy of GPS using X-Y table.

5.5.2 Consistency of GNSS

To test the consistency of the GNSS system, various DLC manoeuvres were performed in a known location. The tests were conducted at various vehicle speeds, as well as with different $4S_4$ suspension settings. This, in combination with driver inconsistencies, results in the same path not always being followed. However, the entry and exit locations were the same for all tests. Figure 5.7 displays the consistency test with the tests shown relative to the entry of the DLC manoeuvre. The paths of the tests are shown to overlap, indicating that the GNSS system has very good consistency.
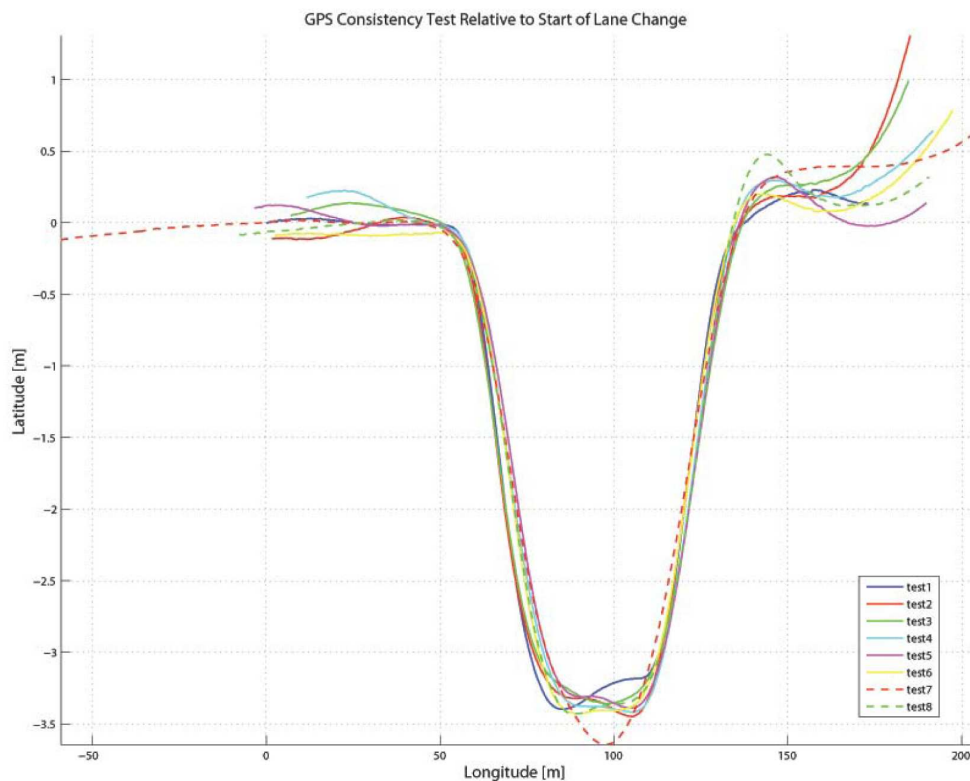

Figure 5.7: Consistency of GPS performing various DLC manoeuvres in same location

The proposed GNSS system provided position information with very little set up time. This allowed the system to be very portable, and allowed testing at various places within minutes. The set-up time depended on the time required by the base station to obtain positioning, at times 10min was sufficient.

5.6   Conclusion

The VBOX3 GNSS system displayed sufficient accuracy to provide position feedback to the driver models. The system provides heading information which is required by the yaw angle controller. The heading information can also be used to create the preview points which are used by both the controllers without having to manually place the receiver at the preview point. This makes it very easy as the yaw controller's preview point is speed dependent and thus would have required a system which manually moves the preview point depending on the vehicle speed.

The driver models now have all the available inputs they require to provide path following. Chapter 6 discusses the experimental validation of the controller while performing DLC at various speeds as well as being driven around a race track.

Chapter 6

Experimental Results

After integrating the GNSS, control strategy and the vehicle sensors, experimental tests were conducted to experimentally evaluate the performance of the two driver models, namely the Inverse Magic Formula Model and the Mathematical Model. Since noise and other dynamic effects are ever present which are generally not modelled, the performance of any controller in real life is generally not as perfect as in simulations. Experimental validation of driver models are rare with the exception of a few (see Thrun et al, 2006; and Urmson et al, 2008). Almost no experimental published results are available. In this chapter the focus is on the experimental validation of the two mentioned driver models on the Land Rover Defender test vehicle performing a DLC and other manoeuvres.

6.1 Controller Tests

The controller code for this study was written in C++ with the program running at 100Hz and GNSS position feedback at 50Hz. If 20km/h is considered the lowest vehicle limit required for control, the associative responsiveness can be determined to be about 0.1s (Figure 4.4). Perdikaris (1991) suggests a rule of thumb that the sampling frequency be 10-20 times the bandwidth of the system. From Sobering (1999) the bandwidth and response time are related by:

$$BW = \frac{0.35}{t_r} \tag{6.1}$$

$$= \frac{0.35}{0.1} \tag{6.2}$$

$$= 3.5Hz \tag{6.3}$$

$$\therefore 35Hz < f_s < 70Hz \tag{6.4}$$

Thus, the sampling frequencies f_s of 50, 100Hz seem adequate for control purposes.

Tests were conducted at Gerotek Test Facilities (Gerotek Test Facilities, 2008). Outriggers were fitted to the vehicle to prevent rollover allowing the test to be conducted in a safe manner (see Figure 6.1). The DGPS base station was erected and allowed sufficient time to obtain its own position (see Figure 6.1).

Figure 6.1: Test vehicle equipped with outriggers to prevent rollover.

6.1.1   Initial Tests

Before any closed loop control tests were performed, the controller algorithms were tested off-line, this was performed for debugging purposes. The tests were conducted by first recording a path through a DLC and then manually repeating the path while recording the controller outputs. Thus, the controller was tasked to follow the recorded path with the stepper motor turned off and steering performed by a human driver. The driver was the supervisor of the study, who has performed on numerous occasions a DLC manoeuvre with this vehicle.

The controller inputs and outputs are shown in Figure 6.2. The first plot shows the recorded path, vehicle path and the cross-track error of a test performed at 60km/h. From inspection the cross-track error seems to be computed correctly. The third plot shows the PD controller output, this plot shows that the noise in the cross-track error is exacerbated by the derivative term. The solution to this was to filter the derivative term with a digital 10Hz low pass filter. The filtering added a slight delay in this term. However, the slight delay affected the control action minimally and simulation results showed that the inclusion of the filtered derivative term still improved performance. The second plot shows the heading of both path and the vehicle, which are the inputs to the main yaw angle controller. The vehicle entered the DLC slightly later, as a result the controller output was slightly affected.

A post processed controller output was created by shifting the inputs to the controller slightly sooner to simulate the vehicle entering at the correct time. The last plot depicts the modified controller output compared to the actual steer rate supplied by the human driver. Since closed loop control was not used the controller does not exactly resemble the driver input. However, the controller has peaks at the same locations as the actual input with some amplitudes comparing well. The cross-track error reaches up to 1m after the late turn in. The first lane change cross-track error is about 0.25m and the return slightly over 0.3m. This shows that not even an experienced driver can follow identical paths every time. The conclusion of the test was that the driver model displayed adequate correlation with a human driver input to allow for closed loop tests to be conducted.
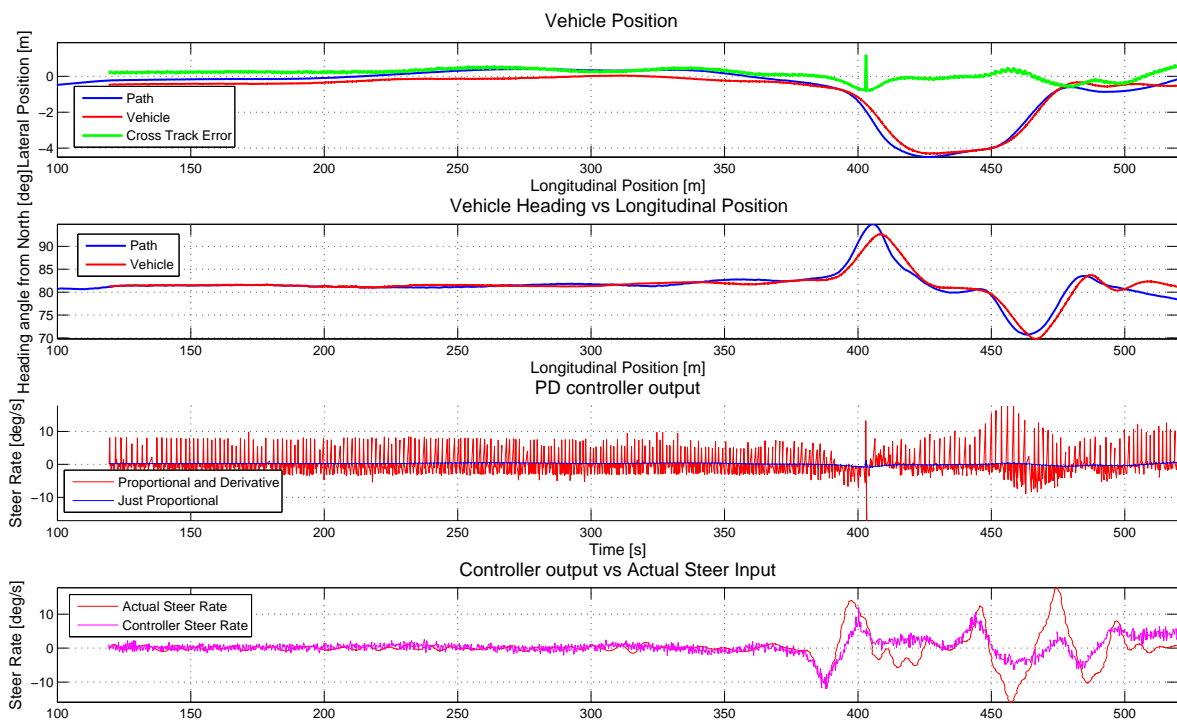

Figure 6.2: Off-line tests of driver model through DLC.

6.2   ISO-3888 Double Lane Change

The DLC was the main manoeuvre used to evaluate the performance of the driver models. The performance was tested at various speeds which included the linear and non-linear tyre regime, with the final test performed at 80km/h to simulate a high speed manoeuvre performed at high lateral accelerations.

6.2.1 Experimental Procedure

The path of the DLC was laid out using high visibility cones. The vehicle was manually driven through the DLC with an entry speed of 40km/h to record a path. This path, recorded at 40km/h, was then followed at various entry speeds with the driver model supplying a steering input. Figure 6.3 depicts a compilation of photos superimposed on top of one another. The photo displays the vehicle at the start of the first lane change, the middle of the lane change, the end of the first lane change, the middle of the second lane change and the end of the whole manoeuvre.

Figure 6.3: Vehicle recording path at 40km/h.

DLC at 20km/h

The first test was conducted at a speed of 20km/h with the $4S_4$ suspension set on the ride comfort (soft) setting and the Inverse Magic Formula Model supplying the steering input.

Figure 6.4 shows the path the vehicle followed through the DLC. The multicoloured plot in the first graph shows the path following of the driver model where the colour indicates vehicle speed according to the colour bar. It is evident from this figure that the driver model allowed for very good path following at 20km/h. The middle graph indicates the lateral acceleration experienced, the noise in the sensors are evident with a low signal to noise ratio at low lateral acceleration. The bottom graph of Figure 6.4 shows both the previewed lateral error used by the PD controller as well as the actual cross-track error from the vehicle's CG. The cross-track error remains lower than 200mm throughout the manoeuvre. The graph also indicates 400m is driven before the actual DLC occurred. This data is included to indicate

the model's capability of following a fairly straight line. This is important because it shows the stability of the driver model and in particular that of the lateral position controller.
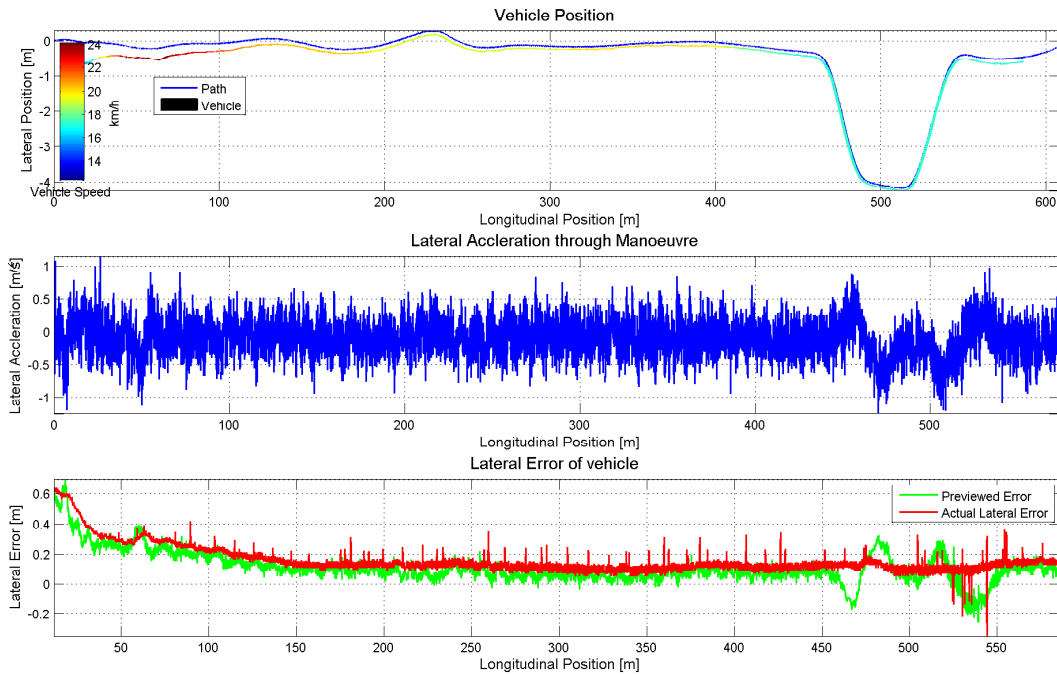

Figure 6.4: Vehicle path through DLC at 20km/h.

Figure 6.5: Vehicle following path through DLC at 20km/h.

A compilation of photos showing the vehicle through the DLC at 20km/h is presented in Figure 6.5. It can be observed from the photos that the vehicle remains within the DLC boundaries at all times.

Figure 6.6 indicates the inputs to the yaw angle controller as measured by the sensors. Again the noise in the gyroscope at low yaw rates is observed. The last graph shows the heading angle of the driver model and the recorded path.

The Inverse Magic Formula Model and the Mathematical Model controller outputs, as well as the actual front wheel steer rate, is plotted in Figure 6.7. The desired yaw acceleration can be noted to be very noisy, this is mainly due to the noise present in the yaw rate measurement. The controller outputs are also noisy, but the slower dynamics of the stepper motor filters out some of the noise as seen in the bottom right figure. Both models are observed to provide almost exactly the same control actions.
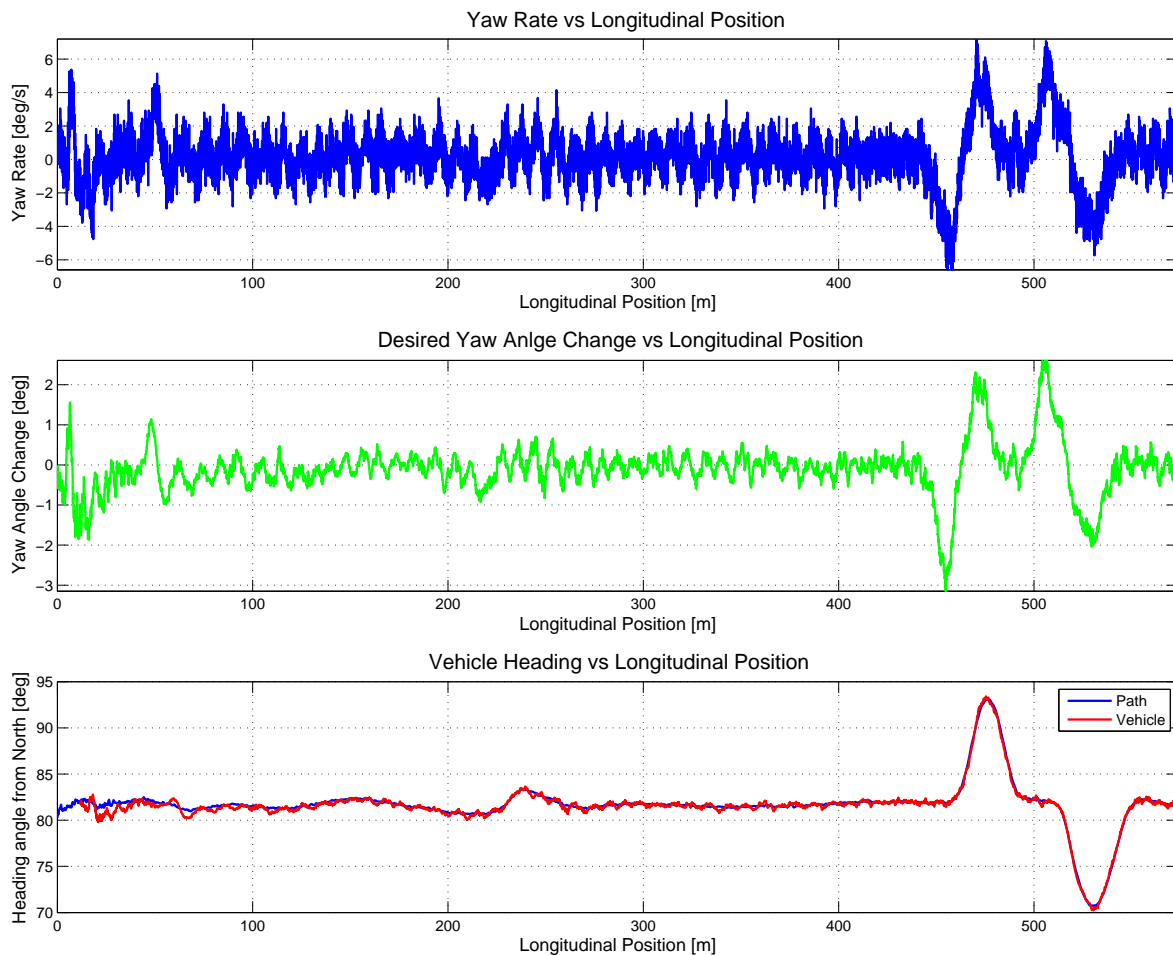

Figure 6.6: Vehicle heading through DLC at 20km/h.
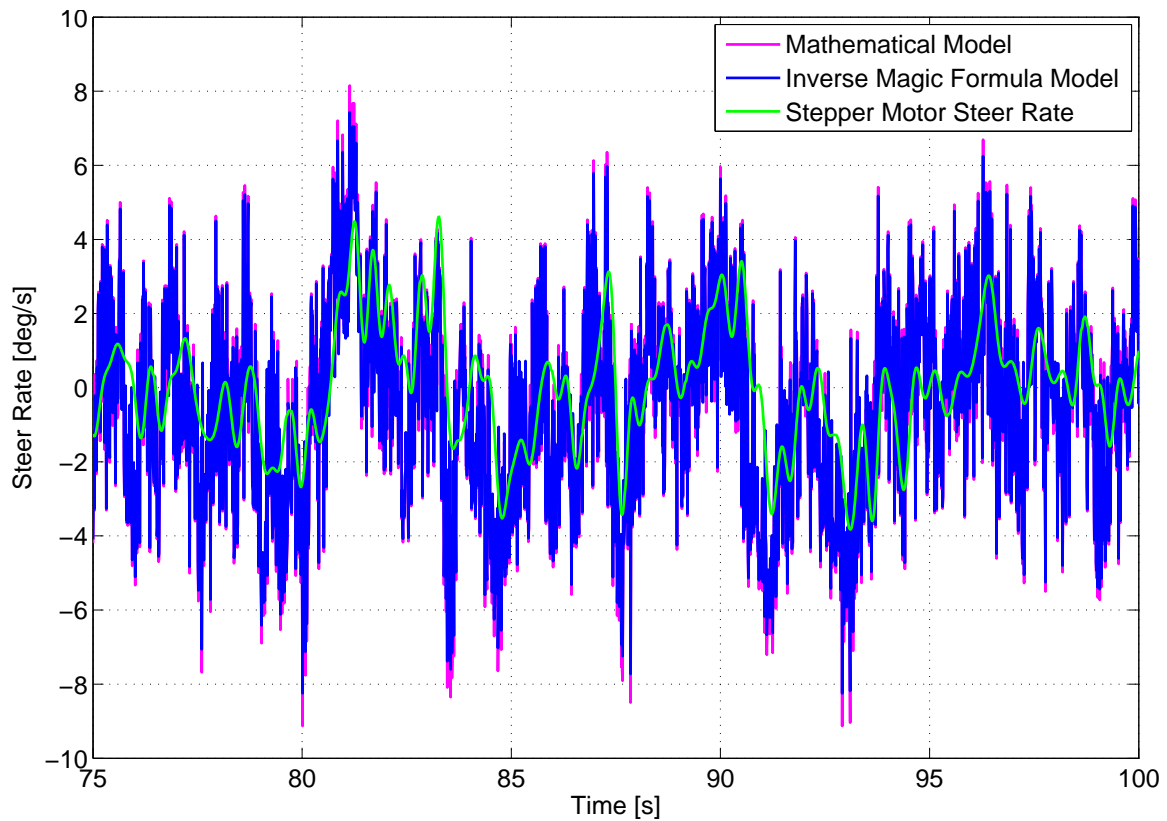
Figure 6.7: Controller outputs through DLC at 20km/h.

The driver models thus appear to provide stable and accurate path following at a speed of 20km/h.

DLC at 40km/h

The 40km/h test was performed with the 4S$_4$ suspension set on ride comfort mode (soft), and the Inverse Magic Formula Model was again used.

Figure 6.8 shows the path the vehicle followed through the DLC. It is observed that the straight line following is slightly oscillatory, however the cross-track error remains within 200mm. The oscillatory nature is partially caused by the measurement of the cross-track error. Discrete position measurements of which the spacing is vehicle speed dependent (ranging from 0.2m at 40km/h to 0.4m at 80km/h) are used. Furthermore, no interpolation is performed resulting in the cross-track error seldom being smaller than 0.1m (i.e $-0.1 < e_{lat} < 0.1$). Thus, even when the actual error is 0m, the controller will compute a value larger than 0.1m and provide a steering action until the value reaches the negative and return. This causes the oscillatory nature observed on the vehicle path as demonstrated in Figure 6.8.

The photo compilation of Figure 6.9 shows the vehicle through the DLC at 40km/h. The compilation shows that the vehicle still remains within the lanes of the DLC manoeuvre.
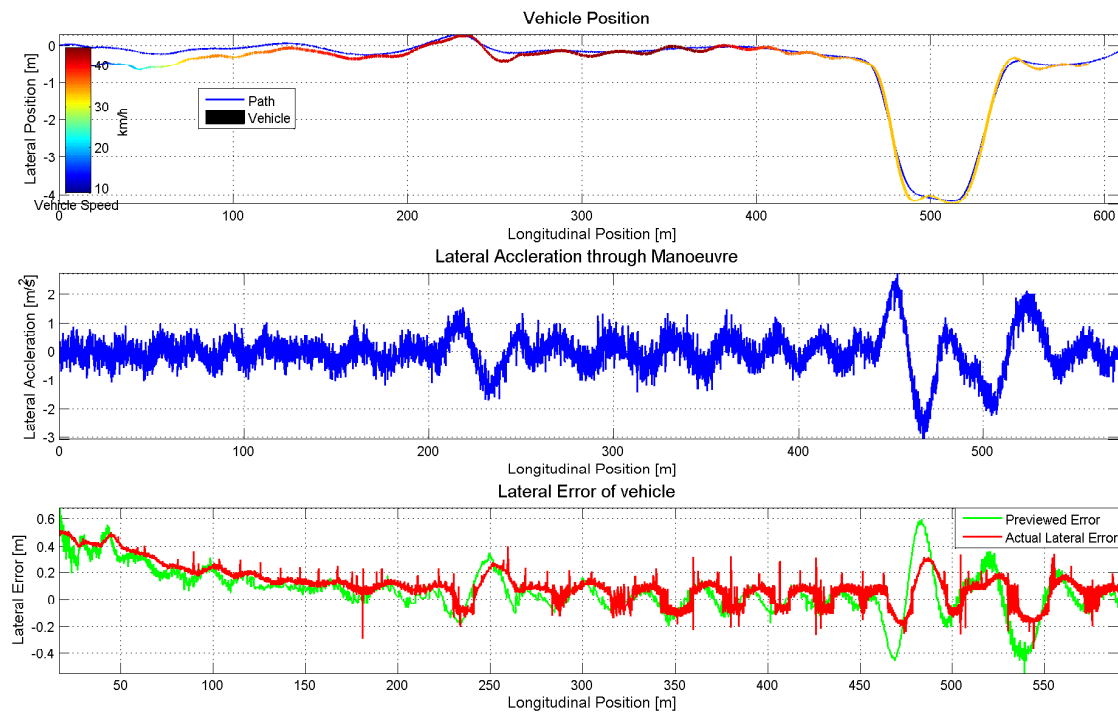
Figure 6.8: Vehicle path through DLC at 40km/h.

Figure 6.9: Vehicle following path through DLC at 40km/h.

Figure 6.10 indicates the inputs to the yaw angle controller. A higher signal to noise ratio is obtained at higher yaw rates. It is evident that the better yaw rate measurement results in a much cleaner desired yaw acceleration and controller outputs. Both the Inverse Magic Formula Model and the Mathematical Model controllers provide similar control outputs as indicated in Figure 6.11. Similar path following performance from these two controllers, can be expected.
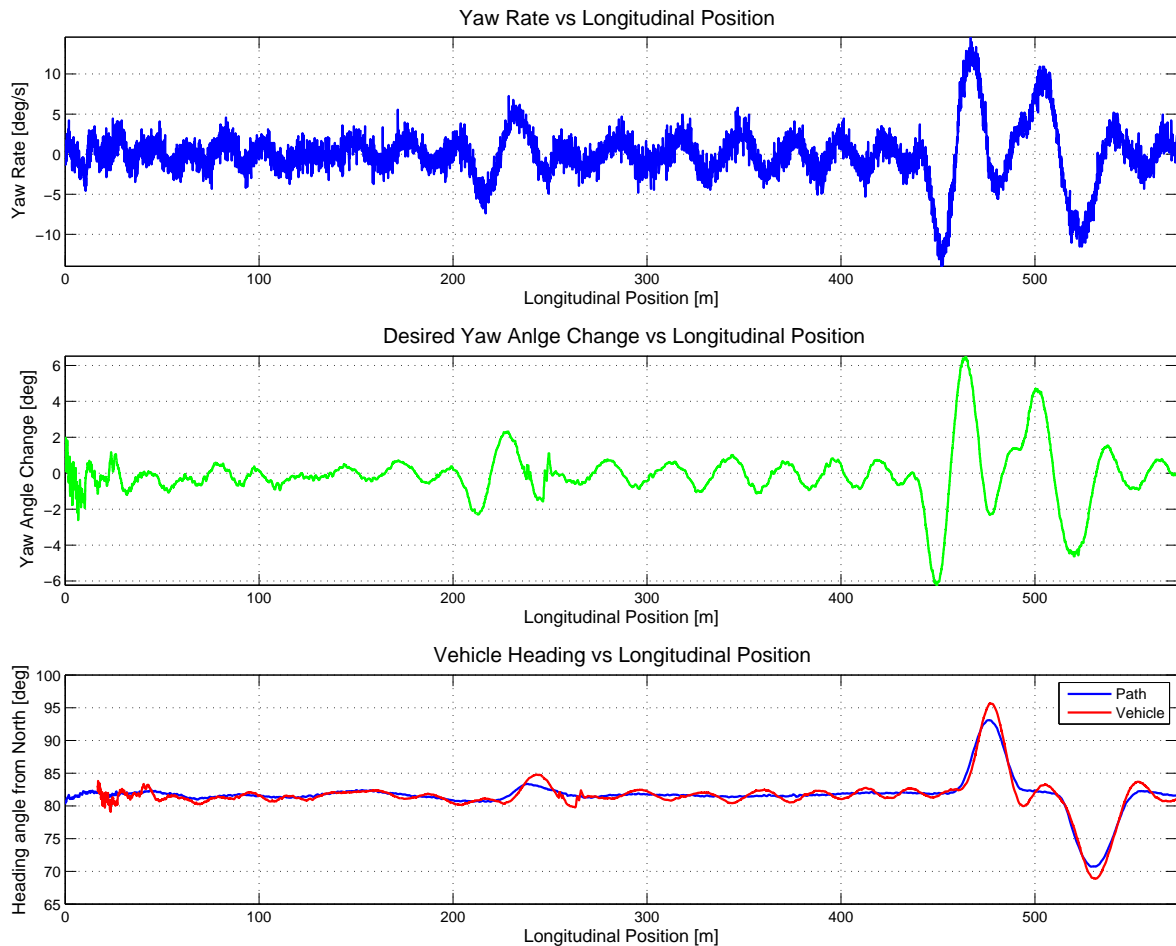

Figure 6.10: Vehicle heading through DLC at 40km/h.
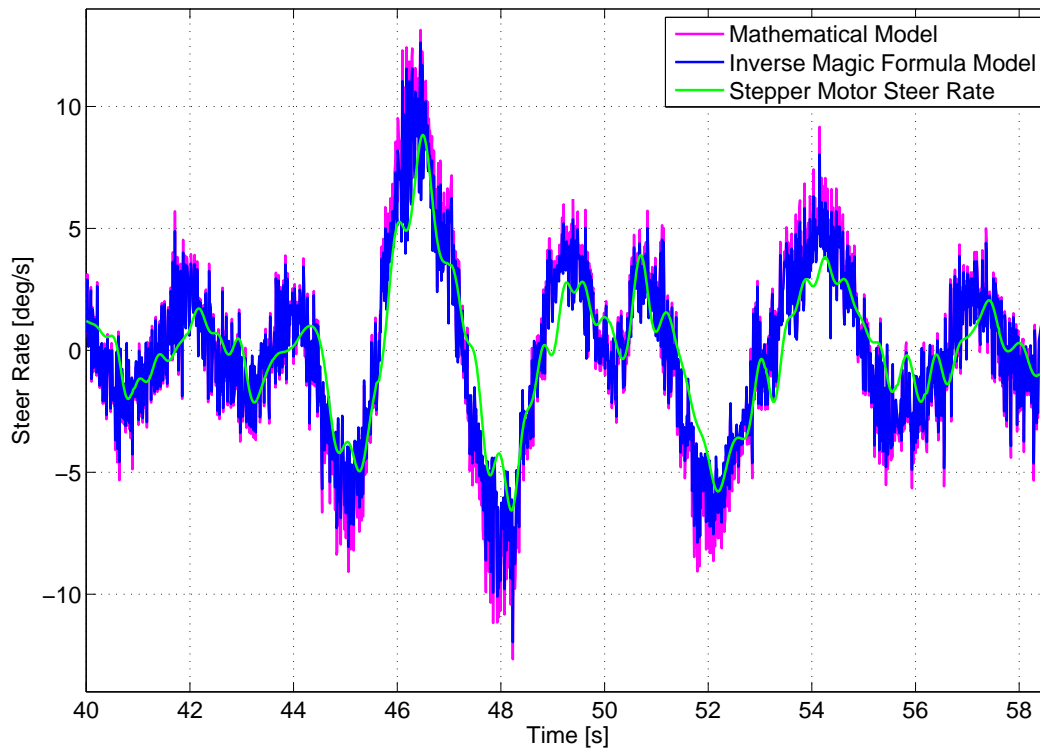
Figure 6.11: Controller outputs through DLC at 40km/h.

DLC at 60km/h

The handling (harder) $4S_4$ suspension setting was used with the Mathematical Model for the DLC at 60km/h. Figure 6.12 shows the path the vehicle followed through the DLC. The same slight oscillatory straight line following, as at 40km/h, is present. However, the gain scheduling prevents the oscillatory action from increasing as vehicle speed increases. As a result, the same 200mm cross-track error in straight line following is achieved at 60km/h. The cross-track error over the DLC is slightly larger, the initial 600mm overshoot observed is due to the delay between the stepper motor action and the controller output. A stepper motor delay of 0.1s at 60km/h will result in a overshoot of slightly over 1.5m. This can be compensated for by increasing the preview time in equations (4.63) and (4.64) as discussed in section 4.4.1. The actual lane overshoot is 500mm for the first lane change and 700mm for the second lane change. To put these values in perspective, an overshoot of 250mm is representative of the tyre width, while 0.5m is slightly more than a quarter of the total vehicle width. The result of this test is indicated in Figures 6.13 to 6.14.

The overshoot of the vehicle centre line causes the vehicle to move slightly out of the lane boundaries. This is shown in the photo compilation of Figure 6.13 and shows that after the first lane change, the outer tyres are slightly over the lane boundary. This is the same for the second lane change. The lane departure is at most half the tyre width.
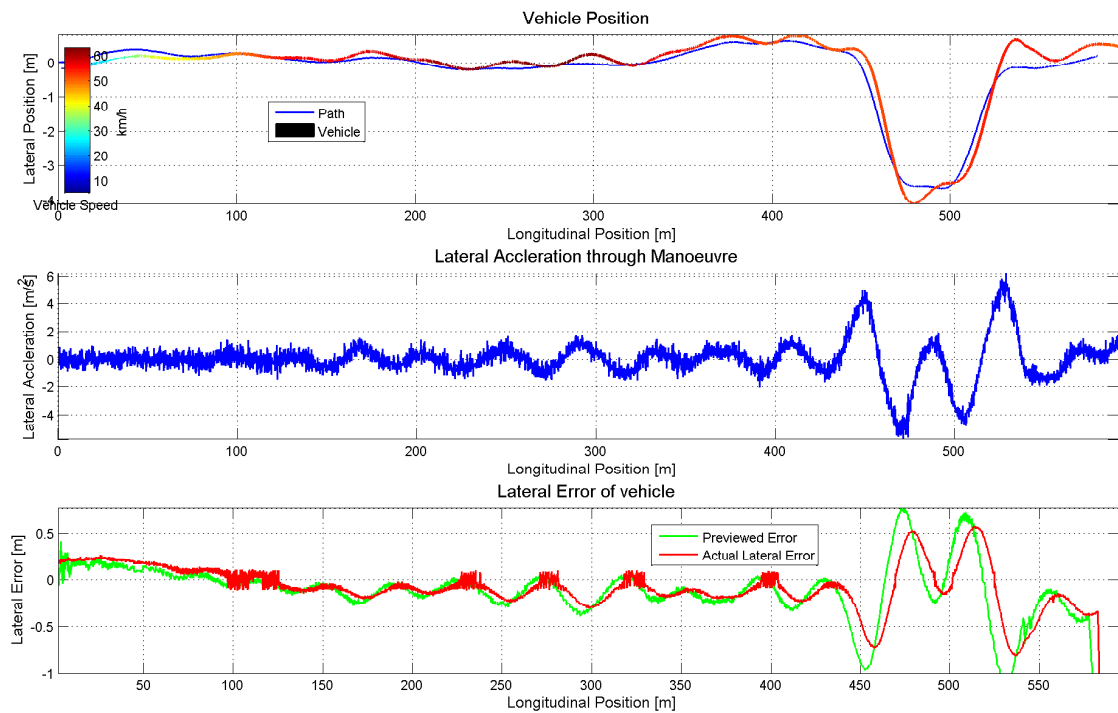
Figure 6.12: Vehicle path through DLC at 60km/h.

Figure 6.13: Vehicle following path through DLC at 60km/h.

The overshoot of the lane changes can partially be explained by the stepper motor not perfectly following the desired steer input as seen in Figure 6.14 (controller output filtered

using 20Hz lowpass zero phase filter). The slight delay in the initial turn in (around 33 second mark) is evident. The actual steer input also does not follow the required input from the controller as noted at the 35, 37 and 39 seconds marks. The imperfect following can be caused by either slipping of the stepper motor or the drive belt of the motor, as a result the vehicle does not turn as required and can thus be the source of most of the overshooting. It should also be noted that the path used was recorded at 40km/h. It is therefore possible that the path is not realistic at higher speeds, i.e the vehicle might not be able to successfully follow the path at higher speeds.
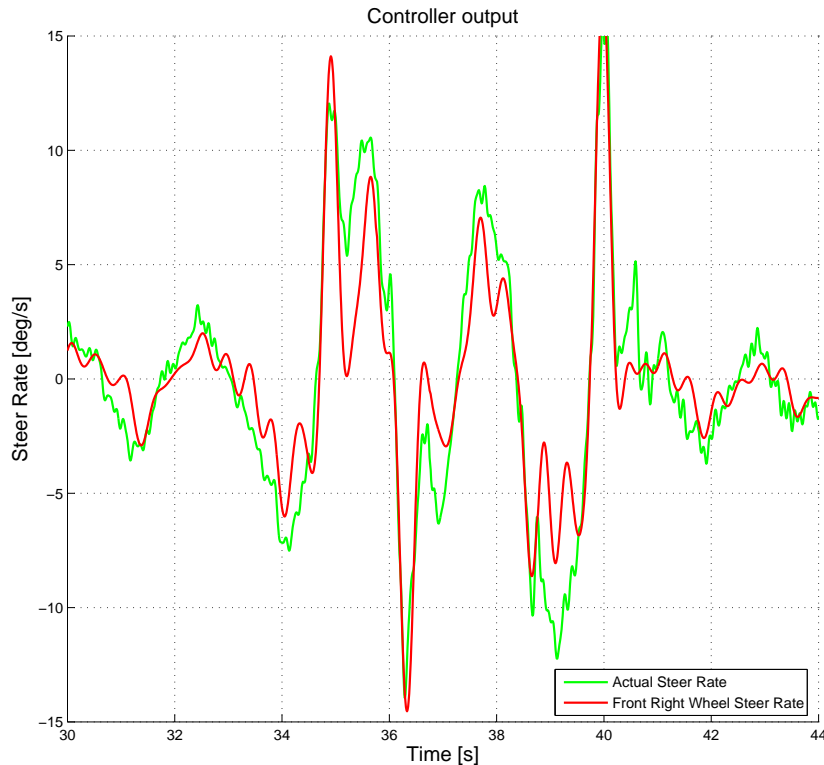

Figure 6.14: Zoomed in controller outputs through DLC at 60km/h.

Figure 6.16 indicates that, at this speed, the Mathematical Model provides a much larger steering action than the Inverse Magic Formula Model. Thus, at higher lateral accelerations the Mathematical Model compensated more for the decrease in yaw acceleration gain.

Lateral acceleration as high as 6m/s^2 is reached through the DLC, this is almost three quarters of the maximum that the vehicle can develop. The vehicle is therefore operating in the non-linear tyre regime. The driver model, however, still provides excellent stability and reasonable path following.
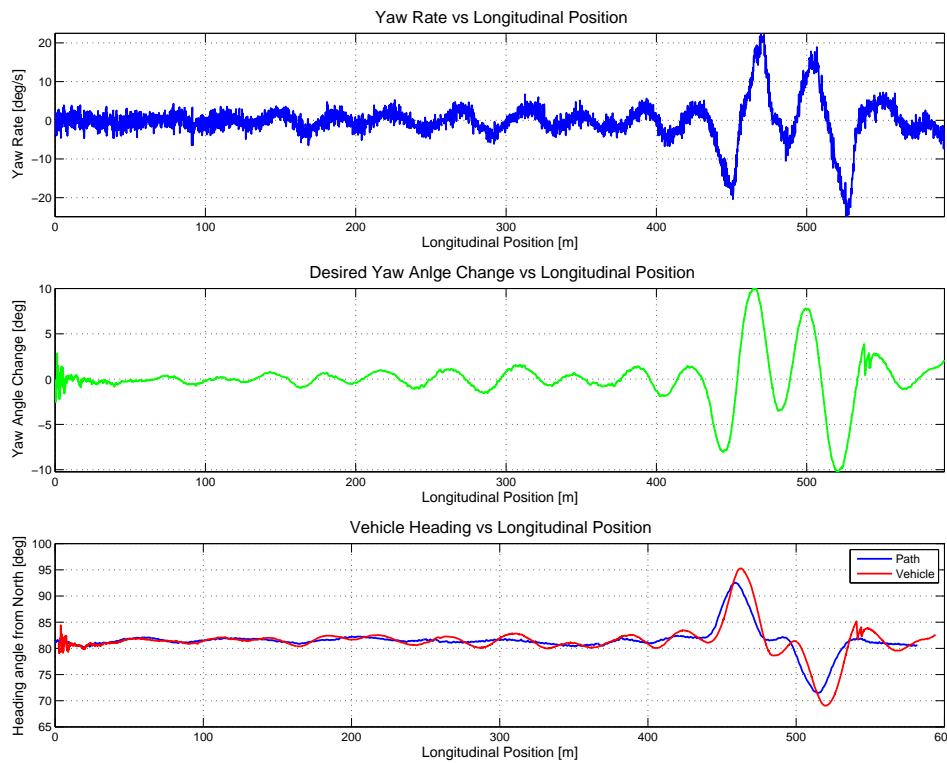
Figure 6.15: Vehicle heading through DLC at 60km/h.
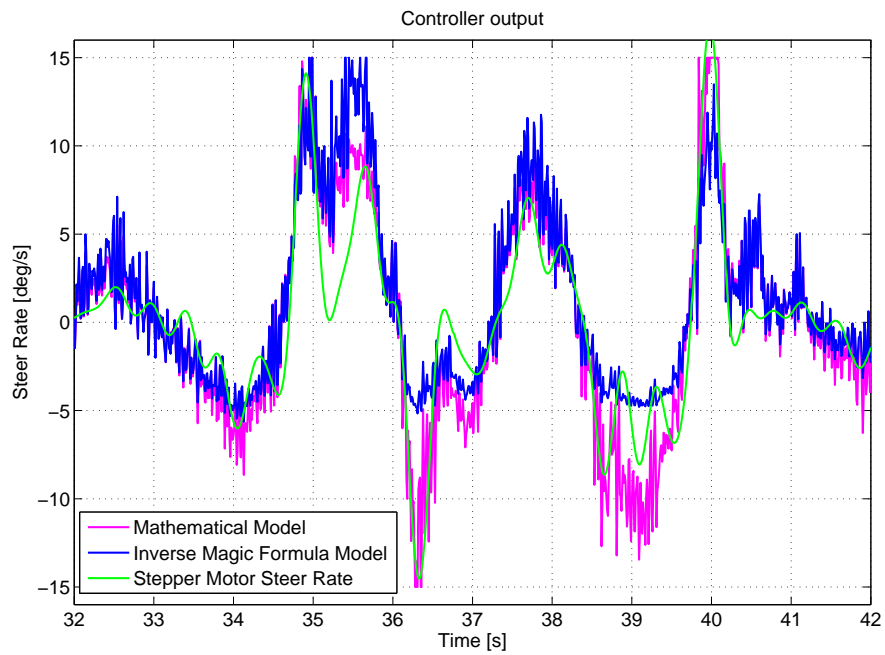
Figure 6.16: Controller outputs through DLC at 60km/h.

DLC at 80km/h

The speed of 80km/h represents almost the limit at which the DLC manoeuvre can be performed with the test vehicle, with even average human drivers failing to negotiate the lane changes successfully. The maximum speed achievable in this vehicle with an experienced test driver is in the region of 90km/h.
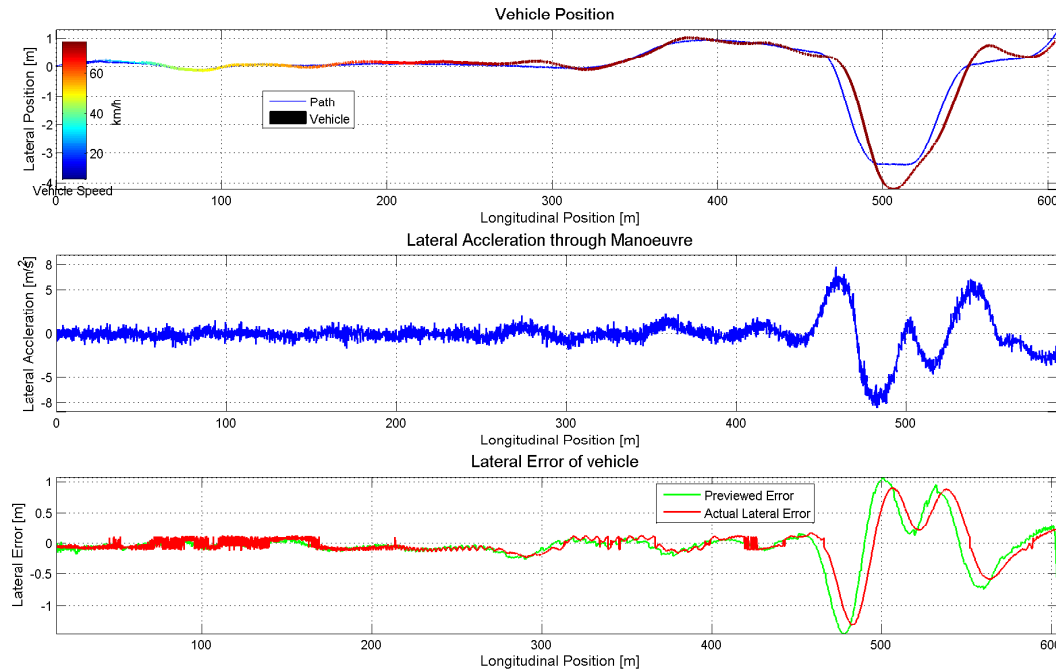

Figure 6.17: Vehicle path through DLC at 80km/h.

The oscillatory straight line following seen at 40 and 60km/h is hardly noticeable at 80km/h (Figure 6.17). A 200mm cross-track error in straight line following is achieved at 80km/h. Again, the cross-track error over the DLC is slightly larger. The initial 1.2m overshoot observed is due to the delay between the stepper motor action and the controller output. A stepper motor delay of 0.1s at 80km/h will result in an overshoot in excess of 2m. The actual measured lane overshoot is 700mm for the first lane change and 500mm for the second lane change, less than half the vehicle's width. Analysing Figure 6.18 it can again be observed that the actuator does not accurately follow the controller command, contributing to some of the overshooting. The photo compilation of Figure 6.19 shows that the overshoot of the centre line causes the vehicle to slightly leave the lane boundaries. The outer wheel is almost completely outside the lane boundary after the first lane change. The body roll of the vehicle is also evident at the end of the lane change indicating the severity of the lane change.
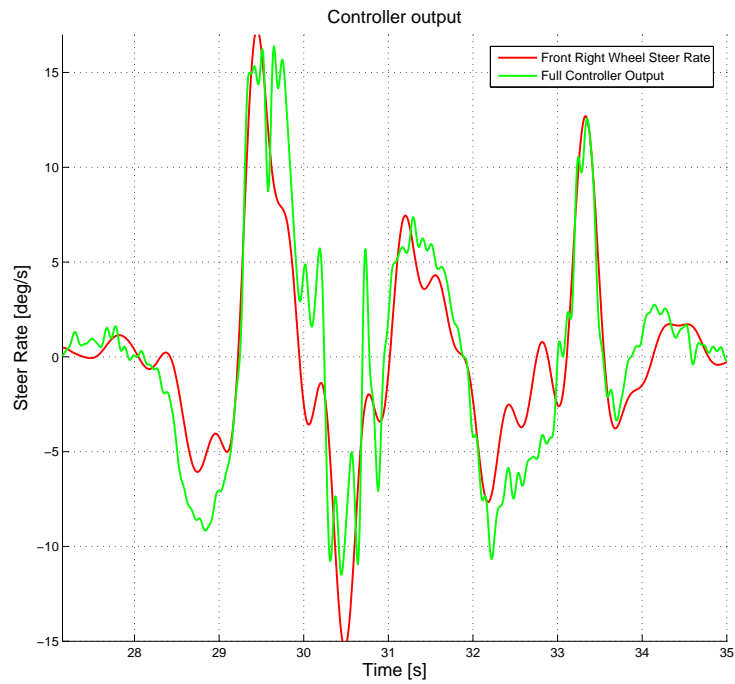
Figure 6.18: Zoomed in controller outputs.

Figure 6.19: Vehicle following path through DLC at 80km/h.

The question whether the path recorded at 40km/h is representative of a path which can easily be followed at 80km/h also arises. A study was therefore conducted to investigate whether the path recorded at 40km/h is suitable at 80km/h. This included determining the expected lateral acceleration the vehicle will experience while performing perfect path following of the recorded path, at various speeds. The lateral acceleration expected from this path can be calculated from the radius of curvature of the path, as presented in section 3.5. The first plot in Figure 6.20 shows the correlation of this method compared to the lateral acceleration measured with the accelerometers. This plot shows good correlation and thus this method can be used to estimate the expected lateral acceleration of a path at different speeds. The top right plot shows the expected lateral acceleration of the path - recorded at 40km/h - at various speeds. This shows that while the lateral accelerations are below the vehicle limit at 80km/h, lateral acceleration as high as 7.5m/s^2 can be expected. The lateral acceleration thus approaches the vehicle limits.
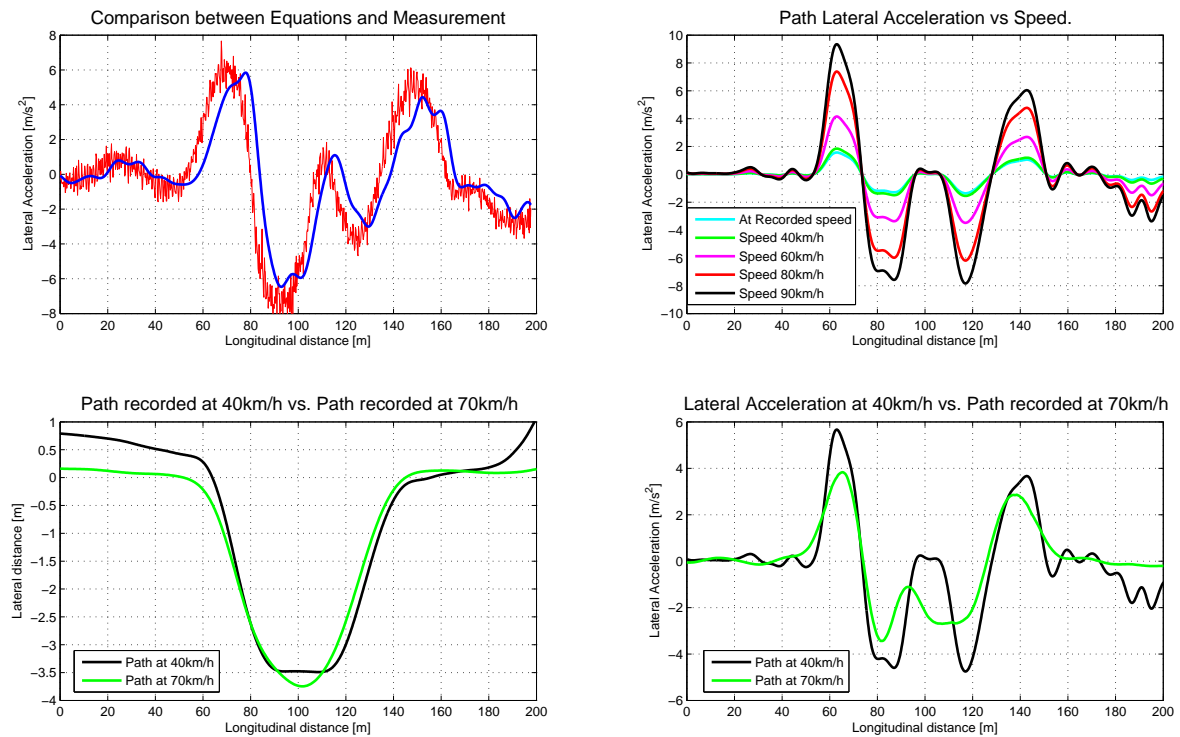
Figure 6.20: Investigation into whether path recorded at 40km/h is suitable at 80km/h.

A comparison with a human driver (same driver) performing the DLC at a higher speed ($\pm$70km/h) is presented in the bottom two plots. At first the path recorded around 70km/h seems similar to that recorded at 40km/h. However, if we scale the lateral acceleration expected from the path recorded at 40km/h to the same speed as the 70km/h path, we reach a different conclusion. The lateral acceleration of the 70km/h path is 2m/s^2 lower at the first peak, with the other peaks about 1m/s^2 lower on average. This shows that it is possible to obtain a path through the DLC that will yield a lower average lateral acceleration on the

peaks. This path should allow for better path following at higher speeds.

The Mathematical Model provides a larger steering action than the Inverse Magic Formula Model (see Figure 6.21) again compensating for a loss in yaw acceleration response as the lateral acceleration increases. Lateral acceleration as high as 6m/s^2 is reached through the DLC, this is almost three quarters of the maximum that the vehicle can develop. The vehicle is thus operating well into the non-linear tyre regime, the driver model however still provides excellent stability and reasonable path following.

The rapid oscillations in the Mathematical Model, between 30 - 31s, is caused by the noise in the lateral acceleration sensor. A filtering of the lateral acceleration shows the average acceleration to be just over 7.5m/s^2. However, the noise in the unfiltered lateral acceleration, which is used in the controller, causes certain measurement points to jumps to over 8.5m/s^2. This is over the limit of the vehicle causing the Mathematical Model to assume the vehicle is past its limits, this causes the output to become oscillatory. Use of an inertial measurement unit to provide yaw rate and lateral acceleration measurements would reduce the noise in the sensors, thus providing better performance and reducing the chance of oscillations in the controller output.
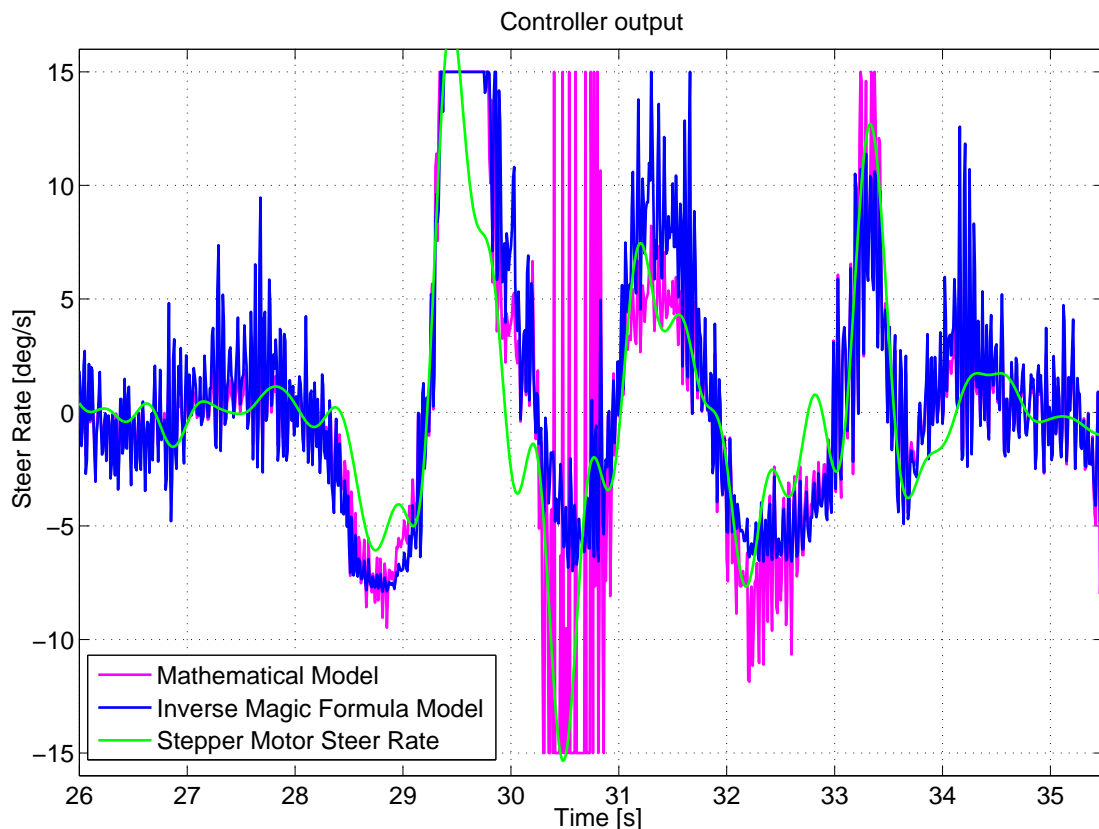

Figure 6.21: Controller outputs.

Additional DLC manoeuvres are provided in Appendix C.

6.3   Gerotek: Dynamics Handling Track

The dynamic handling track at Gerotek contains multiple turns designed to test the handling of a vehicle. Two sections of the track were chosen because tree coverage resulting in a loss of GNSS signal, prevented the whole track from being used.

6.3.1   Section 1 : Top Section

The vehicle was set to the $4S_4$ handling (hard) suspension setting and the Mathematical Model driver model was used. The test was performed with a changing vehicle speed reaching a maximum of 50km/h. The test consisted of a short straight, followed by a slow left hand turn and then a sharp 180° decreasing radius right hand turn.

Figure 6.22: Satellite image of Gerotek dynamic handling track top section with lane boundaries (Gerotek, 2011a).

Figure 6.23 shows that the vehicle followed the path very accurately with the cross-track error staying below 400mm. The vehicle remained stable throughout the test with almost no oscillatory nature. From Figure 6.24 it can be observed that the yaw angle controller follows the desired heading angle very well. The two different controllers gave very similar control outputs as depicted in Figure 6.25. Thus, the Inverse Magic Formula Model would perform similarly as the Mathematical Model.

Figure 6.23: Vehicle path through section 1 of dynamic handling track.
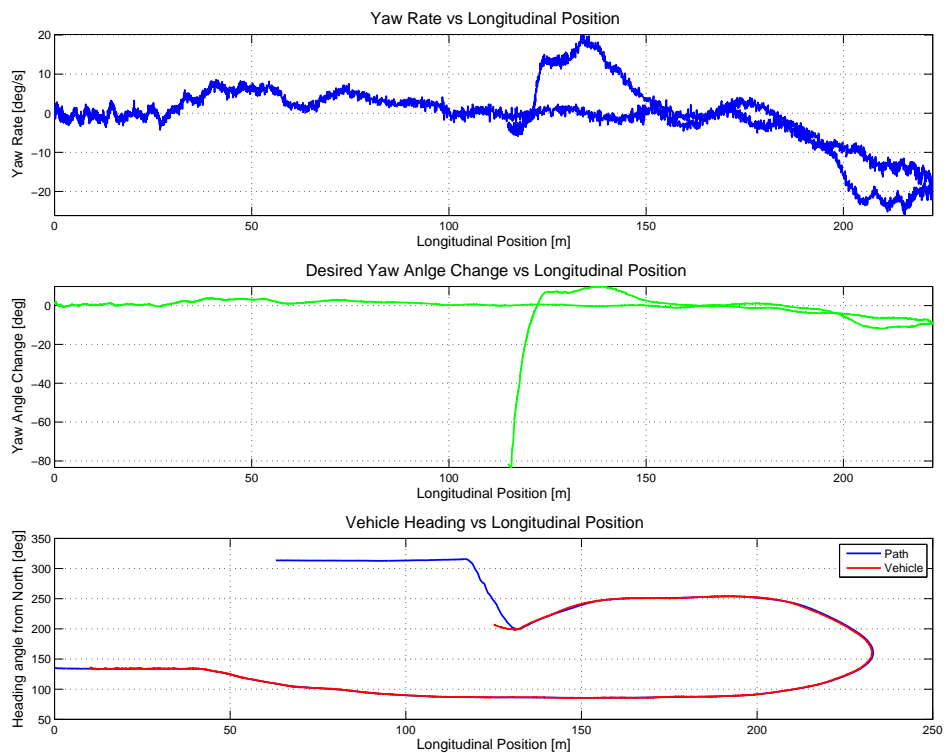
Figure 6.24: Vehicle heading through section 1 of dynamic handling track.
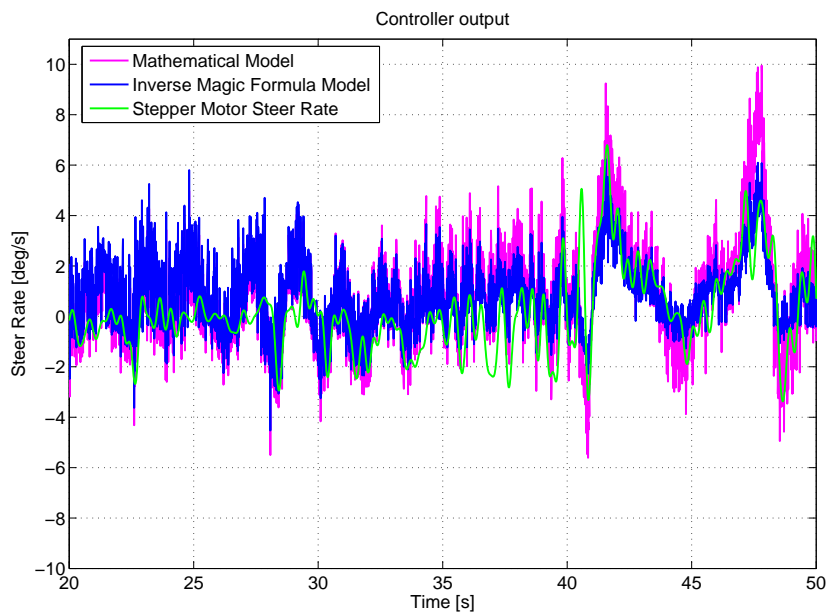
Figure 6.25: Controller outputs through section 1 of dynamic handling track.

6.3.2 Section 2: Final Section

The vehicle remained on the hard suspension setting with the Mathematical Model again being used. This section is very similar to the previous section as it consist of a sharp 180° right hand turn, which is then however followed by a long straight section.

Figure 6.26: Satellite image of Gerotek dynamic handling track last section with lane boundaries (Gerotek, 2011b).

The vehicle reached a top speed of around 55km/h. The vehicle remained stable at all speeds (Figure 6.27) keeping very small cross-track errors. The two different controllers gave very similar control outputs as depicted in Figure 6.28. Thus, the Inverse Magic Formula Model would perform similarly as the Mathematical Model.
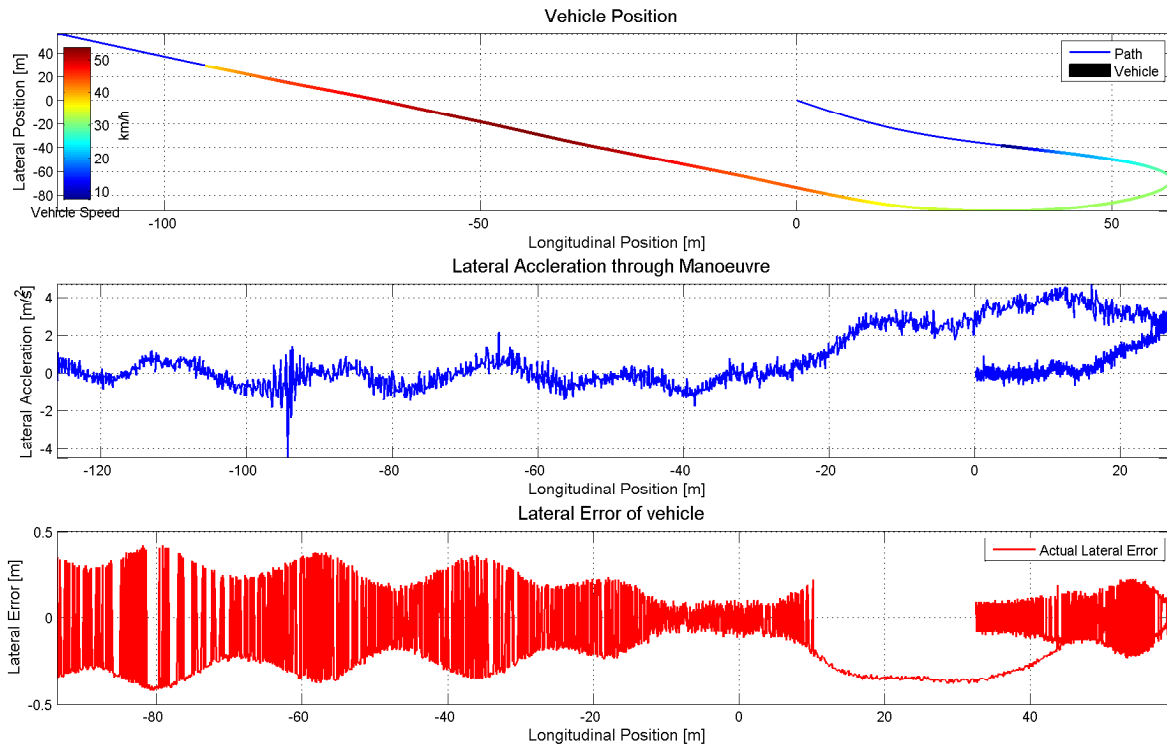

Figure 6.27: Vehicle path through section 2 of dynamic handling track.
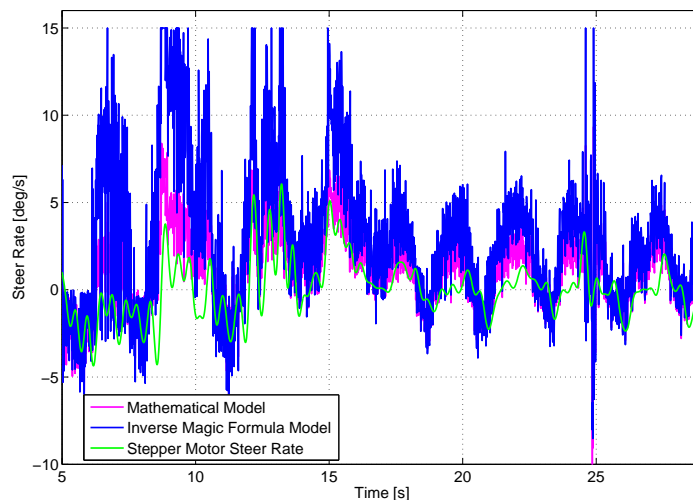
Figure 6.28: Controller outputs through section 2 of dynamic handling track.

From Figure 6.29 it can be observed that the yaw angle controller follows the desired heading angle very well.
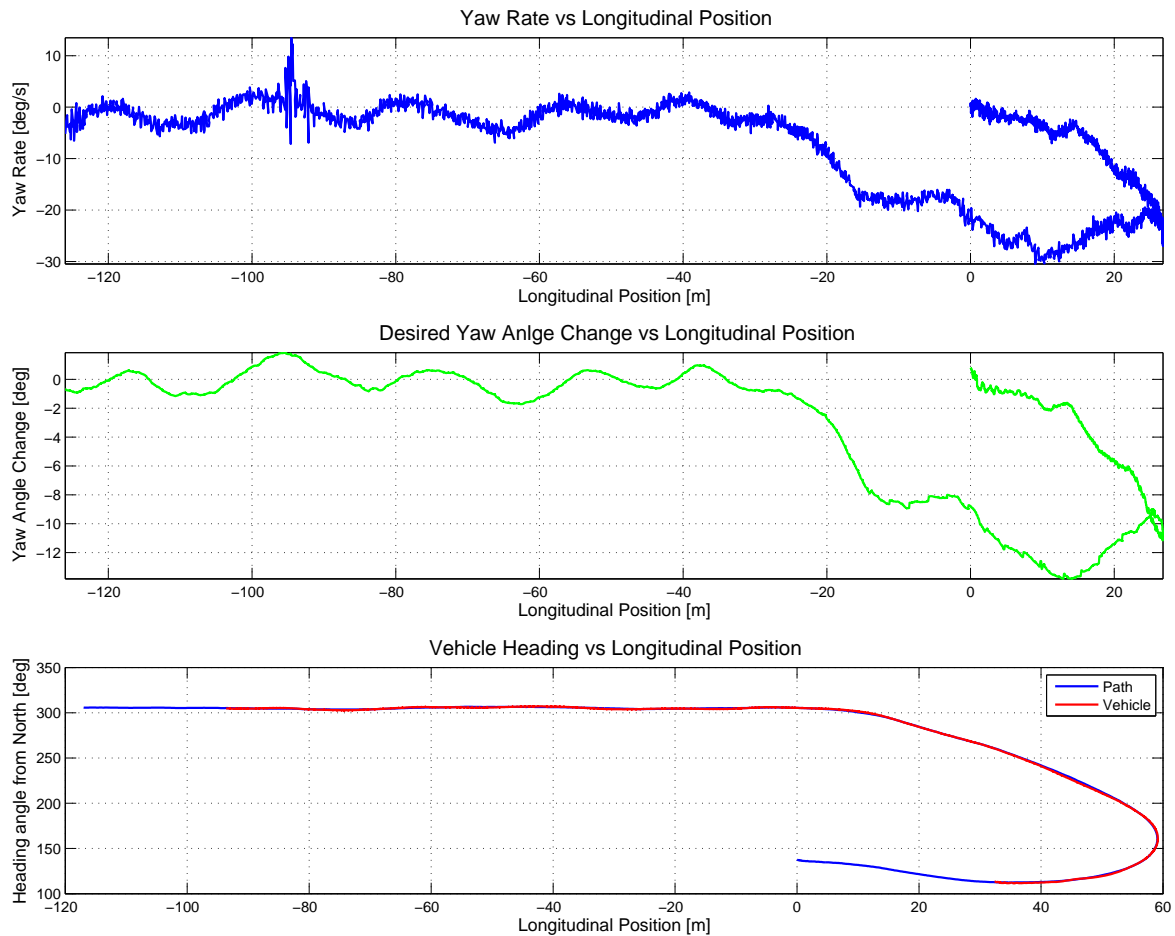
Figure 6.29: Vehicle heading through section 2 of dynamic handling track.

The Mathematical Model performed excellent in all tests. Providing stable and accurate path following during severe manoeuvres such as at DLC at 80km/h as well as more typical everyday roads. The Inverse Magic Formula provided similar outputs as the Mathematical Model, except at higher lateral accelerations as in the DLC at 80km/h. However, during more typical roads, such as the dynamic handling track, the controller outputs were very similar to the Mathematical Model. Therefore, similar performance is expected at normal driving conditions.

6.4 Conclusion

Both driver models provided stable responses at all vehicle speeds tested through the DLC. It can be concluded that the driver models worked exceptionally well, and thus that a path following driver model was successfully implemented on the test vehicle. The reduced handling that occurred at higher vehicle speeds and lateral acceleration was sufficiently modelled by the Mathematical Model to provide acceptable steering action at 80km/h through the DLC. At 80km/h through a DLC the vehicle reaches lateral acceleration which are around 75% of its limits. The Inverse Magic Formula Model provided similar outputs at all speeds but at slightly lower lateral accelerations. Aspects affecting the performance of the driver model were identified to be mostly mechanical components such as the slip in the motor. While some modification to the controller can be made to improve performance such as increasing the preview time as mentioned in section 4.4.1. Preprocessing of the prescribed path can also be performed to optimise the path in order to keep the lateral acceleration to the lowest level at the vehicle's operating speed. The calculation of the cross-track error can be improved to include a form of interpolation between the discrete GNSS coordinates. Thus, smoothing the PD response and reducing some of the oscillatory nature present between speeds of 40-60km/h.

Chapter 7

Conclusion and Recommendations

7.1 Conclusion

This study set out to develop a robust driver model which can be used for path following in autonomous vehicles. The driver model has to be capable of performing manoeuvres at high-way speeds and high lateral accelerations. The autonomous vehicle will then be capable of performing collision avoidance at high-way speed by performing very demanding manoeuvres by supplying a steering input.

The instrumented Land Rover Defender 110 of the University of Pretoria's Dynamics Systems Group, was chosen as a platform to experimentally evaluate the driver model. A full vehicle ADAMS simulation model is available for this vehicle, as well as all vehicle parameters required to develop other mathematical models.

Two driver models were developed in this study. The first is a modified version of the novel driver model developed by Thoresson (2007). This model made use of simulation results conducted on the ADAMS vehicle model to construct the relationship between the steady state yaw acceleration vs. steer rate as a function of vehicle speed. This relationship was successfully modelled by means of the Magic Formula normally used to model tyre lateral forces vs. side-slip angle as a function of vertical load. The inverse of the Magic Formula yielded the steer rate as subject of the equation which could be used for control purposes. This driver model was termed the Inverse Magic Formula Model and was curve fitted with a FFNN to simplify and improve computation time. A simplified non-linear mathematical model, which included a non-linear tyre model was also developed. This non-linear model was sufficient in reconstructing the Inverse Magic Formula Model, thus, not requiring the development of a more complex ADAMS model. It could also be possible to derive this model solely on Pacejka tyre model coefficients and vehicle mass properties.

The second driver model uses a linear vehicle model as a basis. This model is used to obtain a transfer function which can be used for control purposes. The load transfer and the non-linear tyre effect was included in the model by means of a form of sliding mode. The tyre

cornering stiffness was linearised at the tyres' current side-slip angle. The side-slip angle was obtained by first determining the axle forces by means of lateral acceleration measurement, as well as the desired yaw acceleration - which will allow the vehicle to have the same yaw angle as the path at the preview point. The load transfer modelled by means of a steady state assumption allowed for the side-slip angles to be computed from the tyre vertical forces and the axle forces. The linearised cornering stiffness was then used to update the transfer function and improve the modeling at higher lateral accelerations. This model successfully captured the non-linear effect of the tyres.

The proposed use of a GNSS system to provide position information, not only made the experimental validation possible, but required very little set-up time. This allowed the system to be very portable, and allowed testing on various tracks within minutes. The set-up time depended on the time required by the base station to obtain positioning, at times 10min was sufficient. The system provided accurate enough information which allowed the vehicle to follow a path through a severe double lane change at speeds of up to 80km/h.

Both driver models were experimentally validated by performing a double lane change. Initially the Inverse Magic Formula Model was used at the slower speeds with the vehicle on the 4S$_4$ ride comfort (soft) suspension setting. The model provided excellent path following up to 50km/h on the 4S$_4$ ride comfort suspension setting. At 60km/h the vehicle was set to the handling (hard) suspension setting as the vehicle starts to become unstable at this speed on the soft suspension. The inclusion of the non-linear tyre model in the Mathematical Model provided for better path following at higher speeds. The better performance was mainly due to the controller performing better at higher lateral accelerations as a result of the tyre model, which compensates for the reduction in yaw acceleration gain. Both driver models showed good stability and reasonable path following at higher speeds while maintaining accuracy at lower speeds.

7.2 Recommendations

Multiple aspects which could improve the performance of the driver models at higher speeds have been identified. These include:

- The slippage present in the steer system, the delay of the stepper motor and the non-ideal path. If slippage in the system is motor related, it can be prevented by either increasing the stepper motor torque or by using a more powerful motor. If the slippage came as a result of the belt slipping, then a belt tensioner can be added.

- The delay of the stepper motor can be overcome by sampling the path with more preview. The additional preview time should however not be added to the calculation of the desired yaw acceleration, as this will reduce the desired yaw acceleration and therefore the steering action. Rather, the path should be sampled with more preview, but retaining the same steering action, thus allowing more time for the vehicle to obtain steady state.

- The recorded path could also be recorded at a higher speed. This will result in a path which is more suitable to be followed at higher speeds. An alternative would be to perform preprocessing on the prescribed path. The preprocessing would be performed to optimise the path for a given vehicle speed. The optimisation can be performed by minimising the peak and average lateral accelerations the vehicle will experience throughout the path.

- Additional sensors can be added to allow the system to determine its own path. This will result in the development of a more fully autonomous vehicle which performs both path planning and following.

- An inertial navigation system can also be implemented to improve measured parameters such as yaw rate, yaw angle and lateral acceleration. The reduction in noise within these signals will improve the performance of the driver models.

- Speed control can also be added. This will allow the vehicle the control of the speed through the manoeuvre allowing it to slow down in order to reduce the lateral acceleration.

- Stability control by means of differential braking, rear wheel steering and active suspension control, can also be implemented. This will allow the vehicle to operate more safely and reduce the possibility of rollover and prevent uncontrollable slides.

Bibliography

Abe, M. 2009. Vehicle Handling Dynamics. *Butterworth-Heinemann.*

Ackerman, J., Sienel, W. circa 1989. Robust Control for Automatic Steering. *University of California at Irvine, Department of Electrical and Computer Engineering.*

Amidi, O. 1990. Integrated Mobile Robot Control. *Technical Report CMU-RI-TR-90-17, Carnegie Mellon University Robotics Institute.*

Anonymous. 1978. Geometric Design Standards for Rural Two-Lane Two-Way Roads. *National Institute of Transport and Road Research of the CSIR.*

Avon motorsport tyres. 2010. [Online] Available at: *http://www.avonracing.com-/Downloads.aspx* [Accessed 8 November 2010].

Bakker, E., Pacejka, H.B., Lidner, L. 1989. A New Tire Model with an Application in Vehicle Dynamics Studies. *SAE Paper 890087.*

Bernstein, D. 2010. The Global Positioning System (NAVSTAR): An Introduction. *James Madison University* [Online] Available at: *https://users.cs.jmu.edu/-bernstdh/web/common-/lectures/slides_gps_introduction.php* [Accessed 11 December 2010].

Chatzikonis, C.I., Spentzas, K.N. 2009. A Path-Following Driver Model with Longitudinal and Lateral Control of Vehicles Motion. *Forsch Ingenieurwes (2009) 73: 257266 DOI 10.1007/s10010-009-0112-5.*

Clynch, J.R. 2006. Radius of the Earth - Radii Used in Geodesy. *University of New South Wales, Sydney, Australia.*

Corvallis Microtechnology. 1996. Introduction to the Global Positioning System for GIS and TRAVERSE. [Online] Available at: *http://www.cmtinc.com/gpsbook /*[Accessed 8 November

2010].

Cronje, P.H. 2008. Improving Off-Road Vehicle Handling Using an active Anti-Roll Bar. MEng Dissertation, University of Pretoria, Pretoria, South Africa. *http://upetd.up.ac.za- /thesis/available/- etd11262009-011206/.* [Accessed 29 July 2010].

De Luca, A., Oriolo, G., Samson, C. 1998. Feedback Control of a Nonholonomic Car-Like Robot. *Robot Motion Planning and Control*, 171-249.

El Hajjaji, A., Bentalba, S. 2003. Fuzzy Path Tracking Control for Automatic Steering of Vehicles. *Robotics and Autonomous Systems* 43 (2003) 203213.

Els, P.S. 2006. The ride comfort vs. handling compromise for off-road vehicles. *Thesis, University of Pretoria, Pretoria, South Africa.*

Federal Aviation Administration, 2011, Navigation Services - Local Area Augmentation System (LAAS). [Online] Available at: *http://www.faa.gov/about/office_org/headquarters_offices /ato/service_units/techops/navservices/gnss/laas/* [Accessed 2 December 2010].

Fenton, R.E., Melocik, G.C., Olson, K.W. 1976. On the Steering of Automated Vehicles: Theory and Experiment. *IEEE Transactions on Automatic Control*, Vol AC-21, No. 3, June 1976.

Festo. 2010. Stepper motors EMMS-ST. [Online] Available at: *http://xdki.festo.com/xdki- /data/doc_ENGB/PDF/EN/EMMS-ST_EN.PDF.* [Accessed 7 December 2010].

Fiala, E. 1954. Seitenkrafte am rollenden Luftreifen. VDI, Bd.96, Nr. 29, 11.

Genta, G. 1997. Motor Vehicle Dynamics: Modeling and Simulation. *World Scientific, Series on Advances in Mathematics for Applied Sciences - Vol. 43.*

Gerotek, 2011a. Satellite Image, Google Earth. [Online] Available at: *http://maps.google.co.za /maps?hl=en&ie=UTF8&ll=-25.752089,28.022733&spn=0.001672,0.00284&t=f&z=19&ecp ose=-25.75243238,28.02273301,1693.43,-0.052,8.626,0.* [Accessed 30 January 2011].

Gerotek, 2011b. Satellite Image, Google Earth. [Online] Available at: *http://maps.google.co.za /maps?hl=en&ie=UTF8&ll=-25.75326,28.022963&spn=0.001672,0.00284&t=f&z=19&ecpos e=-25.75354123,28.02296325,1626.12,-0.052,9.33,0.* [Accessed 30 January 2011].

Gerotek Test Facilities. 2008. Gerotek Test Facilities. [Online] Available at: *http://www.arms- corbusiness.com/SubSites/Gerotek/Gerotek01_landing.asp.* [Accessed 7 December 2010].

Gillespie, T.D. 1992. Fundamentals of Vehicle Dynamics. *Society of Automotive Engineers.*

Gingrich, C.G., Kuespert, D.R., McAvoy, T.J. 1992. Modeling Human Operators Using Neural Networks. *International Society of Automation Volume 31, Issue 3, 1992, Pages 81-90.*

Hessburg, T., Tomizuka, M. 1994. Fuzzy Logic Control for Lateral Vehicle Guidance. *IEEE Control Systems. August 1994.*

Hugemann, W., Nickel, M. circa 2002. Longitudinal and Lateral Accelerations in Normal Day Driving. *Ingenieurburo Morawski and Hugemann.*

ISO3888-1:, Passenger cars - Test track for a severe lane-change manoeuvre - Part 1: Double lane-change. 1999. *The International Organisation for Standardisation.*

Jazar, R.N. 2008. Vehicle Dynamics: Theory and Applications. *Springer.*

Kat, C. 2009. Suspension Forces on a Tri-Axle Air Suspended Semi-Trailer. *Unpublished Masters Dissertation. University of Pretoria, Pretoria, South Africa.*

Lo, S.M., Liu, M., Yuen, K.K., Zhang, P.H. 2008. An Artificial Neural-network Based Predictive Model for Pre-evacuation Human Response in Domestic Building Fire. *Fire Technology, 45, 431449, 2009.*

MacAdam, C.C. 2003. Understanding and Modeling the Human Driver. *Vehicle System Dynamics* Vol. 40, Nos. 13, pp. 101134.

MathWorks. 2010. Simulink - Simulation and Model-Based Design. [Online] Avialable at: *http://www.mathworks.com/products/simulink/.* [Accessed 7 December 2010].

MathWorks. 2011. MATLAB - The Language Of Technical Computing. [Online] Avialable at: *http://www.mathworks.com/products/matlab/.* [Accessed 19 January 2011].

Moon, K.S., Osborne, M.D., Kuykendall, D.J., Poirier, W.H. 2002. Modeling of Human Response From Vehicle Performance Characteristics Using Artificial Neural Networks. *Society of Automotive Engineering. Paper Number: 2002-01-1570.*

Moon, S., Moon, I., Yi, K. 2009. Design, tuning, and evaluation of a full-range adaptive cruise control system with collision avoidance. *Control Engineering Practice 17 (2009) 442-455.*

MSC.Software. 2010. ADAMS Multibody Dynamics. [Online] Available at: *http://www.msc-software.com/Products/CAE-Tools/Adams.aspx.* [Accessed 7 December 2010].

NHTSA, 2003 Consumer Information; New Car Assessment Program; Rollover Resistance; Final Rule. *Federal Register.*

O'Connor, T. 2004. Lateral Avoidance. *California Center for Innovative Transportation at the University of California at Berkeley and Caltrans.*

Pacejka, H.B. 2002. Tyre and Vehicle Dynamics. *Society of Automotive Engineers, Warrendal*, USA.

Peng, H. and Tomizuka, M. 1990. Lateral Control of Front-Wheel-Steering Rubber-Tire Vehicles. *PATH Research Report, UCB-ITS-PRR-90-5.*

Peng, H. and Tomizuka, M. 1991. Optimal Preview Control for Vehicle Lateral Guidance. *PATH Research Report, UCB-ITS-PRR-91-16.*

Perdikaris, G.A. 1991. Computer controlled systems: theory and applications. *Springer.*

Ploch, M., Edelmann, J. 2007. Driver Models in Automobile Dynamics Application. *Vehicle System Dynamics.* 45:7, 699-741.

Racelogic. 2010. VBOX (Velocity Box): Non Contact Speed & Distance Measurement using GPS. [Online] Available at: *http://www.velocitybox.co.uk/.* [Accessed 7 December 2010].

Rajamani, R. 2006. Vehicle Dynamics and Control. *Springer.*

Reymond, G., Kemeny, A., Dorulez, J., Berthoz, A. 2001. Role of Lateral Acceleration in Curve Driving: Driver Model and Experiments on a Real Vehicle and a Driving Simulator. *Human Factors: The Journal of the Human Factors and Ergonomics Society 2001 43: 483.*

Segura, F.M. 2010. The Representation of the Earth. [Online] Available at: *http://ajourneya crosst-ime1.wordpress.com/2010/09/19/unit-1-the-representation-of-the-earth/.* [Accessed 20 January 2011].

Sharp, R.S. 2005. Driver Steering Control and a New Perspective on Car Handling Qualities. *Proc. IMechE Vol. 219 Part C: J. Mechanical Engineering Science.*

Sharp, R.S., Casanova, D., Symonds, P. 2000. A Mathematical Model for Driver Steer-

ing Control, with Design, Tuning and Performance Results. *Vehicle System Dynamics, 33: 5, 289326.*

Sienel, W., Ackerman, J. circa 1995. Automatic Steering of Vehicles Involving Feedforward of the Estimated Track Curvature. *DLR, Oberpfaffenhofen, Weszling, Germany.*

Snider, J.M. 2009. Automatic Steering Methods for Autonomous Automobile Path Tracking. *Technical Report CMU-RI-TR-09-08, Carnegie Mellon University Robotics Institute.*

Sobering, T.J. 1999. Bandwidth and Risetime. *SDE Consulting.*

Thoresson, M.J. 2007. Efficient Gradient-Based Optimisation of Suspension Characteristics for an Off-Road Vehicle. *Unpublished PhD thesis, University of Pretoria, Pretoria, South Afirca, http://upetd.up.ac.za/thesis/available/etd-08042008-093103/.*

Thrun, S., Montemerlo, M., Dahlkamp, H., Stavens, D., Aron, A., Diebel, J., Fong, P., Gale, J., Halpenny, M., Hoffmann, G., Lau, K., Oakley, C., Palatucci, M., Pratt, V., Stang, P., Strohband, S., Dupont, C., Jendrossek, L.E., Koelen, C., Markey, C., Rummel, C., van Niekerk, J., Jensen, E., Alessandrini, P., Bradski, G., Davies, B., Ettinger, S., Kaehler, A., Nefian, A., Mahoney, P. 2006. Stanley: The Robot That Won the DARPA Grand Challenge. *Journal of Field Robotics*, 23(9):661-692, 2006.

Trimble. 2010. How GPS works. [Online] Available at: *http://www.trimble.com/gps/howgps-.shtml.* [Accessed 10 June 2010].

Universal Tracking, 2010. Global Positioning System. [Online] Available at: http://universal tracking.com/?tabid=81. [Accessed 2 December 2010].

Urmson, C., Anhalt, J., Bagnell D., Baker, C., Bittner, R., Clark, M.N., Dolan, J., Duggins, D., Galatali, T., Geyer, C., Gittleman, M., Harbaugh, S., Herbert, M., Howard, T.M., Kilski, S., Kelly, A., Likhachev, M., McNaughton, M., Miller, N., Peterson, K., Pilnick, B., Rajkumar, R., Rybski, P., Salesky, B., Seo, Y.W., Singh, S., Snider, J., Stentz, A., Whittaker, W., Wolkowicki, Z., Ziglar, J., Hong, B., Brown, T., Demitrish, D., Litkouhi, B., Nickolaou, J., Sadekar, V., Zhang, W., Struble, J., Taylor, M., Darms, M., Ferguson, D. 2008. Autonomous Driving in Urban Environments: Boss and the Urban Challenge. *Journal of Field Robotics*, 25(8):425-466, 2008.

Uys, P.E., Els, P.S., Thoresson, M.J., Voight, K.G., Combrinck, W.C. 2006. Experimental Determination of Moments of Inertia for an Off-Road Vehicle in a Regular Engineering Laboratory. *International Journal of Mechanical Engineering Education 34/4.*

Uys, P.E., Els, P.S. and Thoresson, M.J., 2007, Suspension settings for optimal ride comfort of off-road vehicles travelling on roads with different roughness and speeds. *Journal of Terramechanics, Vol. 44, pp. 163-175.*

Yoshida, T. 2010. Automatic Steering System for Rotary Snow Removers. *The Joint $9^{t}h$ Asia Pacific ISTVS Conference and Annual Meeting of Japanese Society of Terramechanics Sapporo, Japan, September 27 to 30, 2010.*

Appendices

Appendix A

Vehicle Properties

Table A.1: Vehicle properties

Parameters	Value
Total Vehicle Mass (m)	2047kg
Vehicle Sprung Mass	1576kg
Mass Moment of Inertia	($2057kgm^2$)
Distance between Front Axle and CG (l_f)	1.4m
Distance between Rear Axle and CG (l_r)	1.4m
Track Width Front and Rear (d_f and d_r)	1.486m
Distance Between Left and Rear 4S$_4$ Struts	1.009m
Front Roll Centre Height (h_f)	0.3985m
Rear Roll Centre Height (h_r)	0.517m
Roll Centre to CG (h_s)	0.14m
Front Tyre Cornering Stiffness (C_f)	36821N/rad
Rear Tyre Cornering Stiffness (C_r)	36822N/rad

Appendix B

Comparison Between Simplified Models and the Full Vehicle Model

In Appendix B, the simplified models developed in chapter 4 are compared to the full vehicle model at 120km/h.
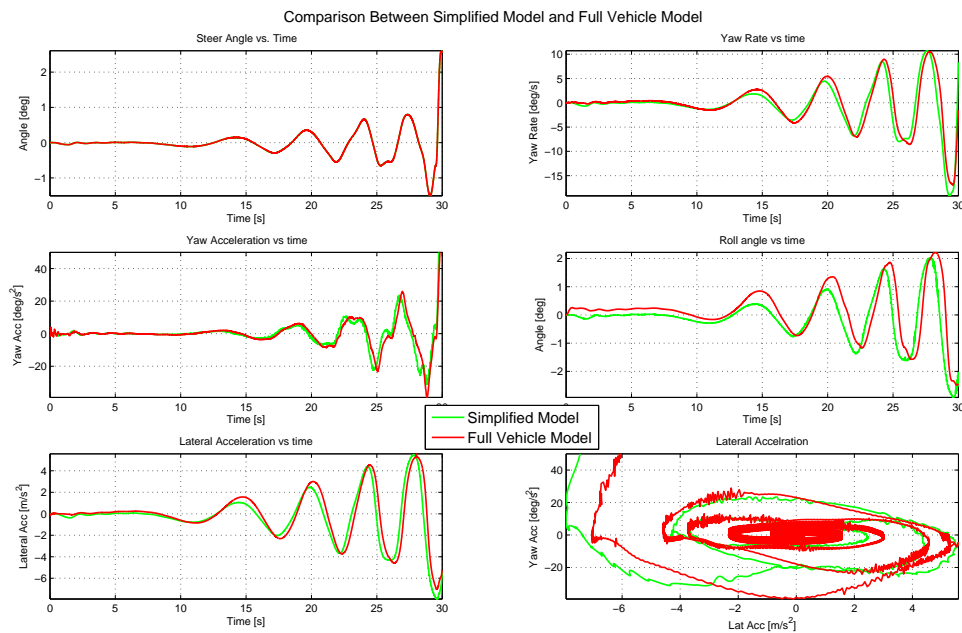
Figure B.1: Comparison between non-linear simplified model and full vehicle simulation for the yaw acceleration response.
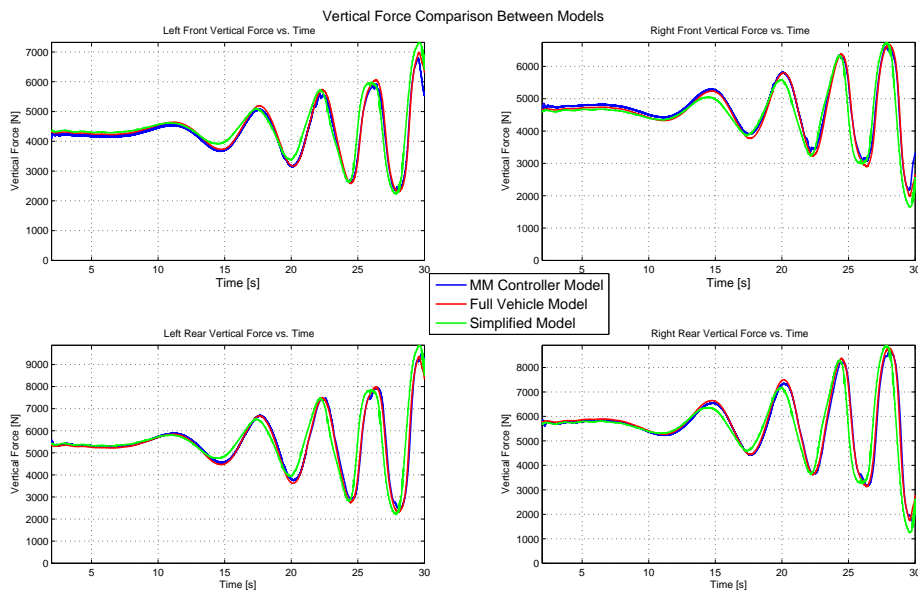
Figure B.2: Comparison between simplified models (non-linear and Mathematical Model) and full vehicle simulation model for vertical tyre load performing a sinusoidal path with increasing frequency at 120km/h.
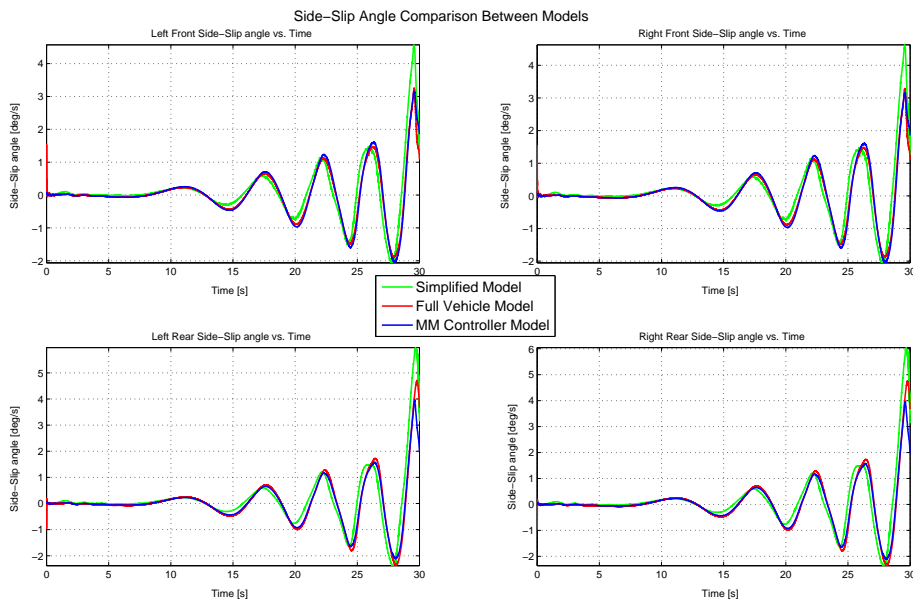
Figure B.3: Comparison between simplified models (non-linear and Mathematical Model) and full vehicle simulation model for side-slip angle performing a sinusoidal path with increasing frequency at 120km/h.
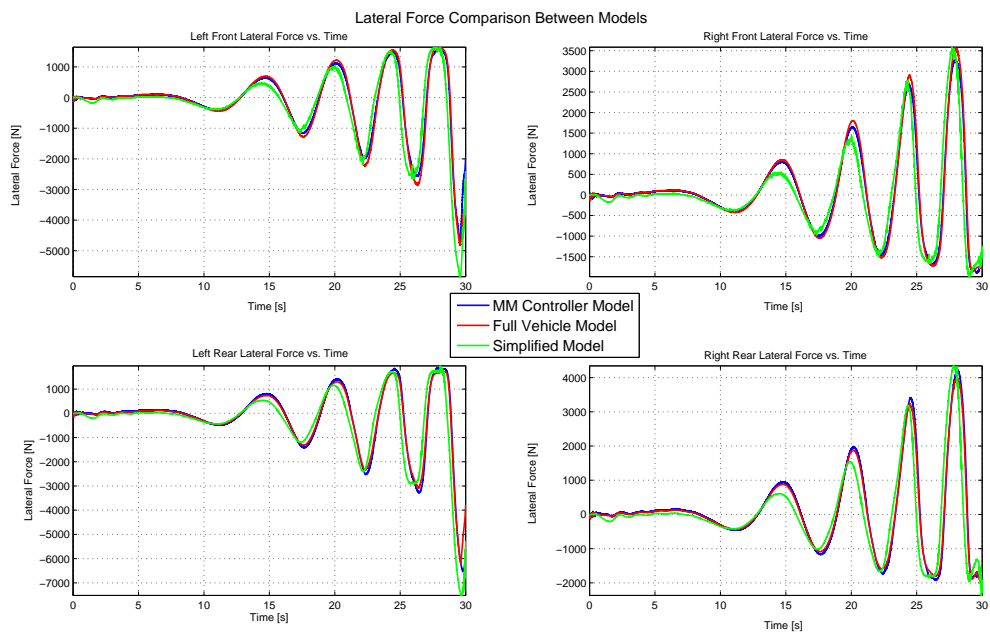
Figure B.4: Comparison between simplified models (non-linear and Mathematical Model) and full vehicle simulation model for lateral tyre force performing a sinusoidal path with increasing frequency at 120km/h.

Appendix C

Additional DLC Path Following Plots

In Appendix C, additional double lane change manoeuvres at different speeds, as well as with both controller models are presented.
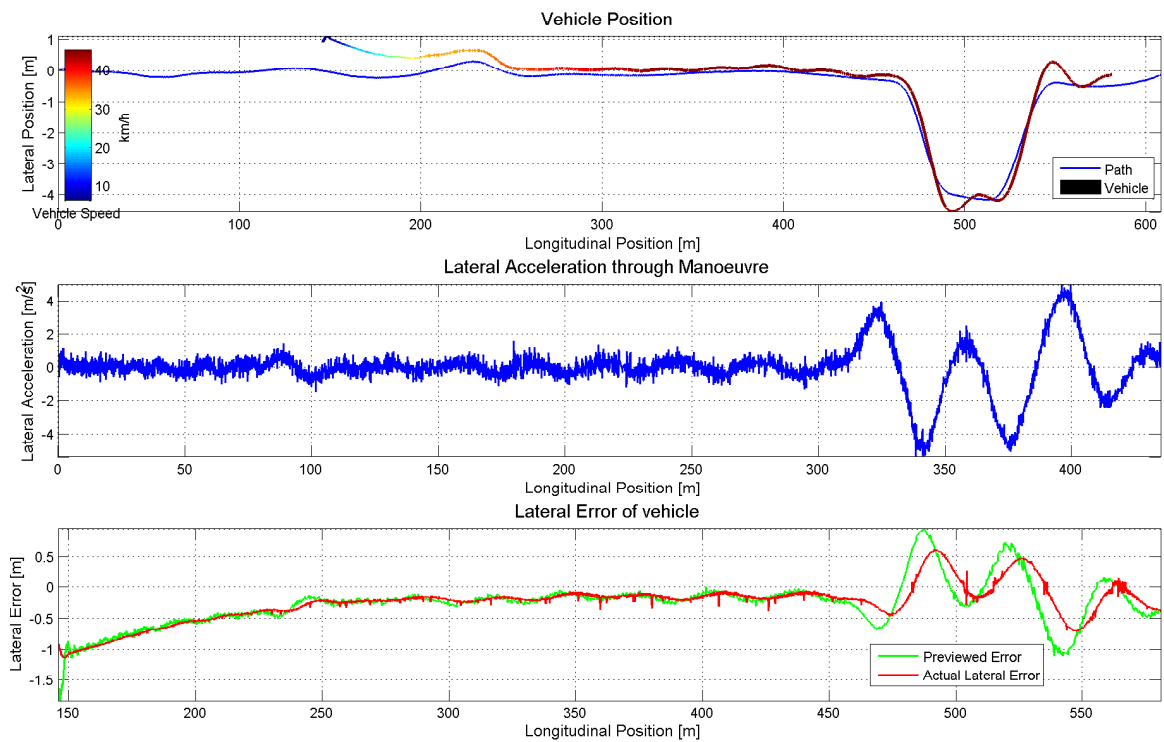

Figure C.1: Path following through DLC using the Mathematical Model and soft suspension setting at 50km/h.
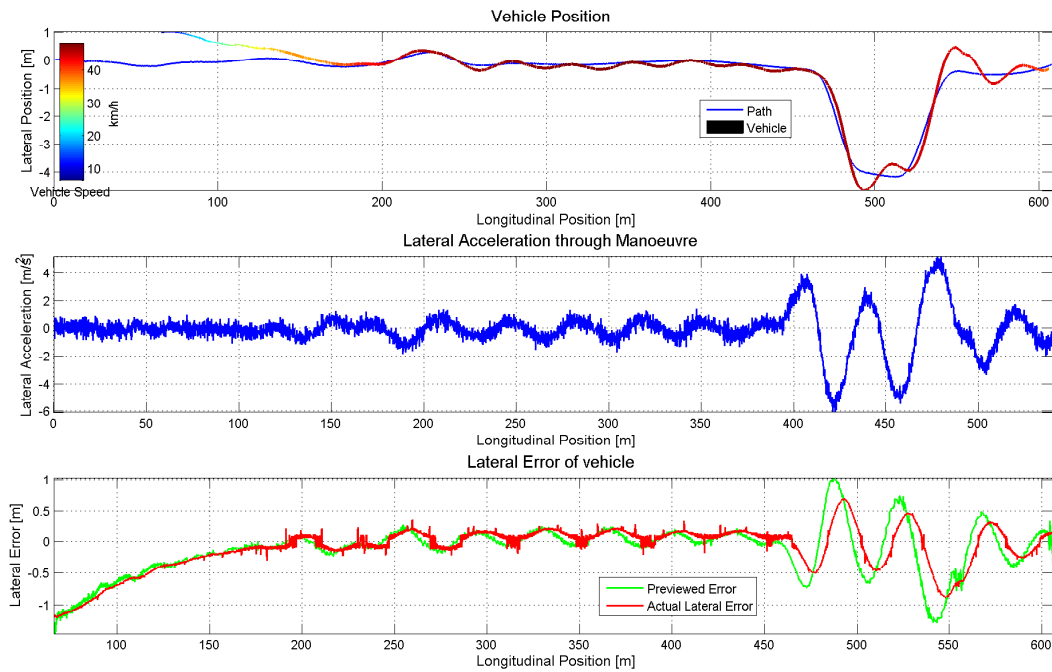
Figure C.2: Path following through DLC using the Inverse Magic Formula Model and soft suspension setting at 50km/h.
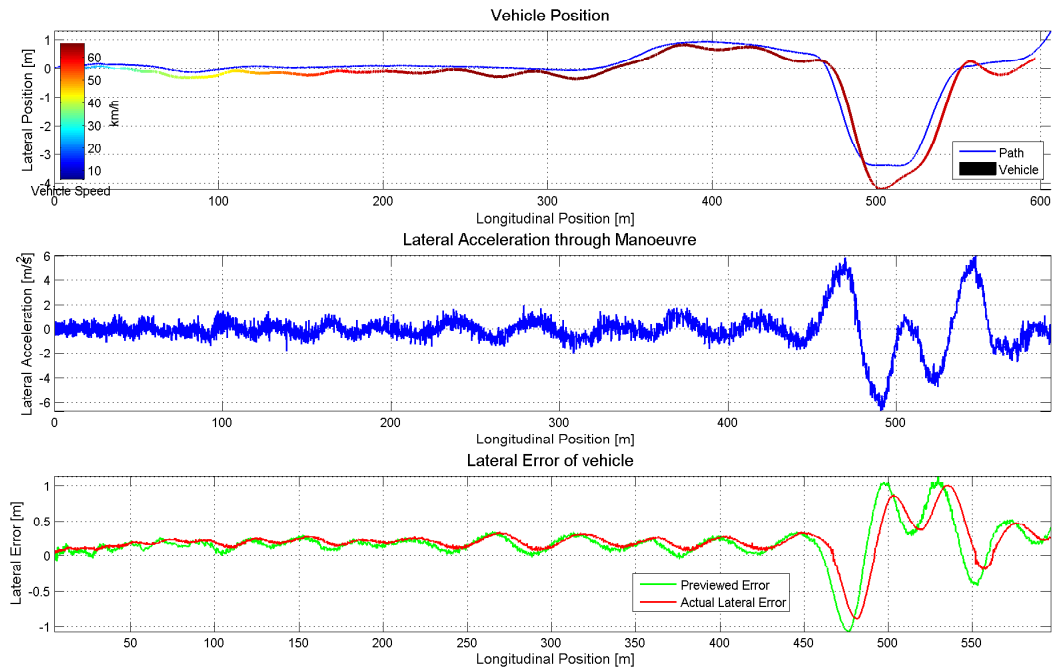

Figure C.3: Path following through DLC using the Mathematical Model and hard suspension setting at 70km/h.
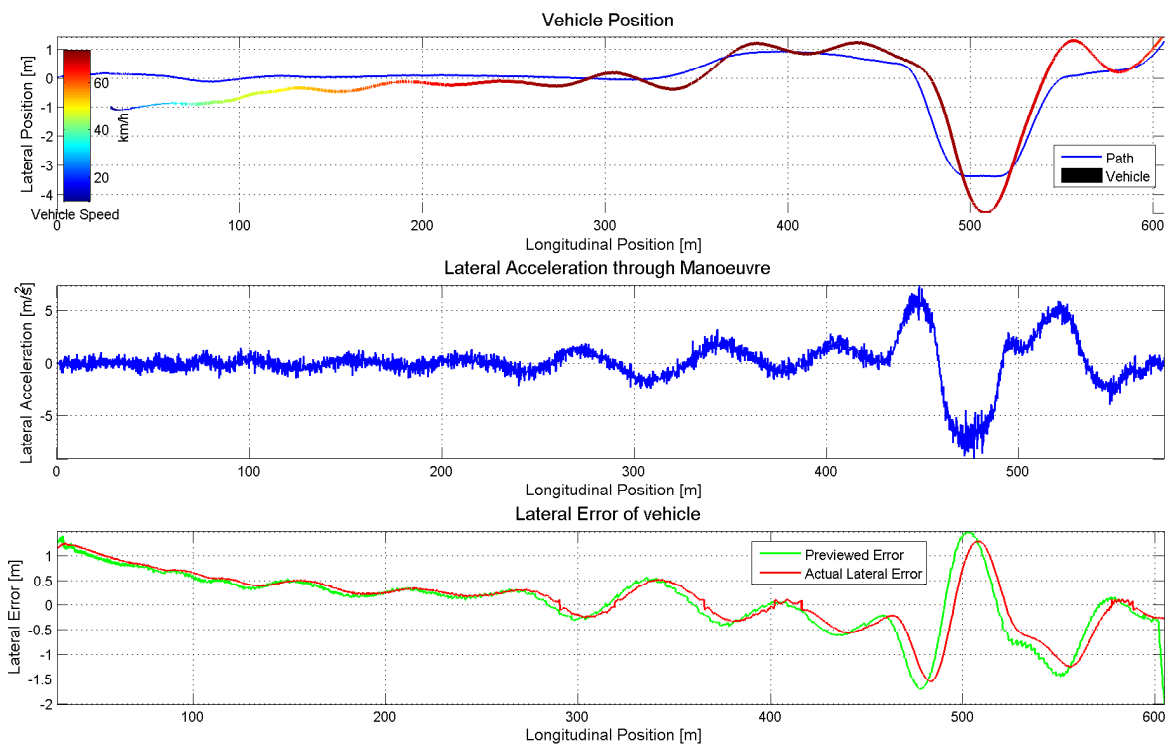
Figure C.4: Path following through DLC using the Inverse Magic Formula Model and hard suspension setting at 80km/h.